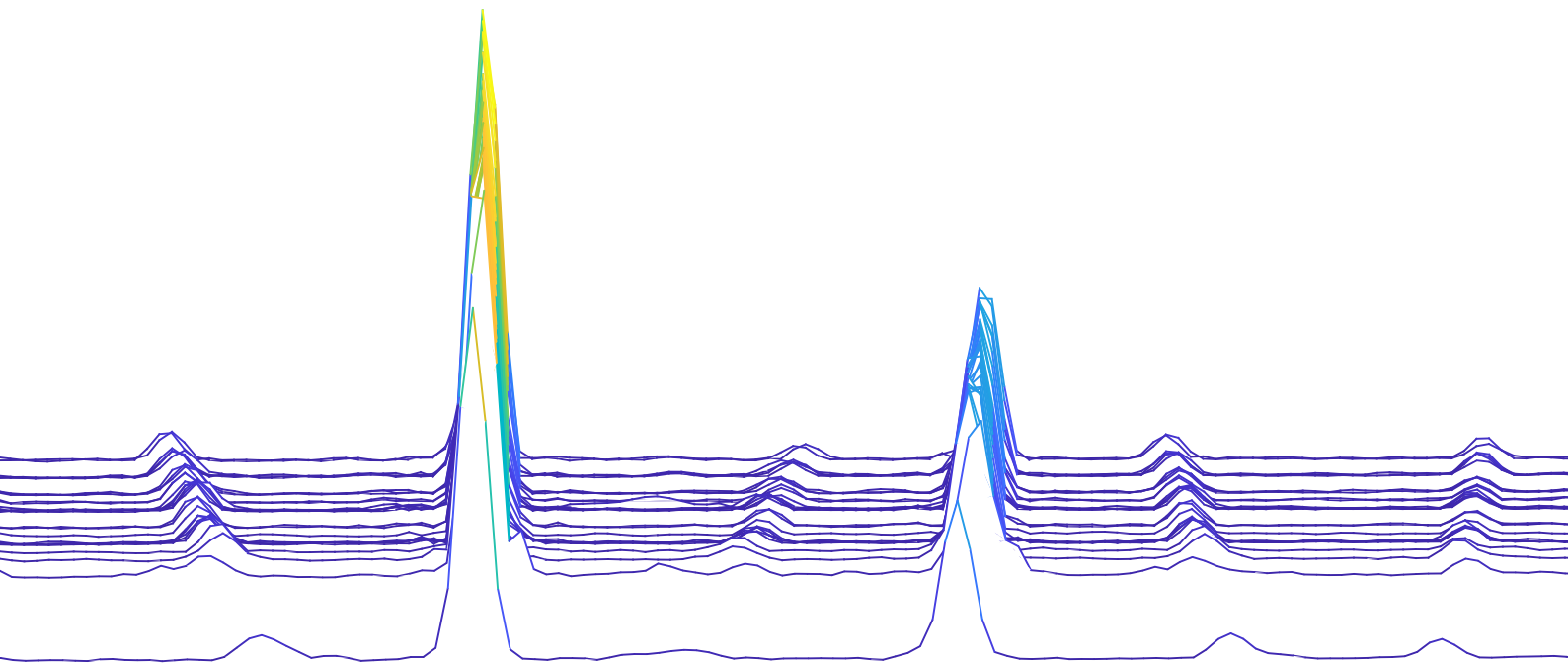


Microvibration test bench for tiny reaction wheels

MSc Space Engineering Thesis report

Fabio Mingione



Microvibration test bench for tiny reaction wheels

MSc Space Engineering Thesis report

by

Fabio Mingione

to obtain the degree of Master of Science
at the Delft University of Technology,
to be defended publicly on March 15, 2022 at 14:00.

Student number: 4630785

Project duration: January 22, 2019 – March 15, 2022

Thesis committee: Dr. J. Guo, TU Delft – LR-SPE-SSE, supervisor

Ir. J. Bouwmeester, TU Delft – LR-SPE-SSE

Ir. I. Uriol Balbin, TU Delft – LR-ASM-AS&CM

An electronic version of this thesis is available at <http://repository.tudelft.nl/>.

I never lose.
I either win or learn.
– Nelson Mandela

Abstract

Reaction wheels are often the main contributor to microvibrations on satellites. These vibrations are a source of pointing errors and therefore need to be limited as much as possible. The miniaturization trend in the space industry and universities fostered the production of very small reaction wheels, suited to Cubesat and PocketQube scales. A novel method to measure microvibrations for these kinds of wheels is proposed in this thesis. Due to budget and resolution constraints, a standardized method is indeed not available for this scale yet. The main idea behind this method is to amplify vibrations through a flexible mounting bracket on which the wheels are fixed and later calculate the source disturbance via a transmissibility function. This measurement method will be studied for validation against some initial requirements. Two types of tests are proposed for this purpose: In the first, a MEMS accelerometer is attached to the mounting bracket to measure accelerations, while in the second a laser is pointed to a mirror on the mounting bracket to measure displacement. The tests will be compared with two models: the empirical model, which is a parameter estimation model with test results as input; and the unified model, which combines the empirical model and an analytical model, simulating the equations of motion of the system with input parameters from a CAD model. The main results will include microvibration waterfall plots and static and dynamic imbalance values. Although it was not possible to entirely validate the test bench prototype within the scope of this thesis, room for improvement is left, with some hints for possible future work.

*Fabio Mingione
Delft, March 2022*

Contents

List of Figures	vii
List of Tables	xi
1 Introduction	1
1.1 Motivation	1
1.2 Microvibration theory and definitions	2
1.2.1 Flywheel imbalance	2
1.2.2 Ball bearing imperfections	4
1.2.3 Torque ripple	5
1.3 Microvibration tests and models	5
1.4 Research objective	5
1.5 Research questions	6
1.6 Thesis structure	8
2 Conceptual design	11
2.1 Test approach concept selection	11
2.2 Mounting bracket, tests and models requirements	15
2.3 High-level architecture of the test and modeling approach	18
3 Test bench design	21
3.1 Soft-suspended test bench concept	21
3.2 Equipment	22
3.3 Setup	23
3.3.1 Production	26
3.3.2 Working principle	28
3.3.3 Possible measurement solutions and failed attempts	30
3.3.4 Usage of fans for verification	31
4 Microvibration tests	33
4.1 Test plan	33
4.2 Arduino control	34
4.3 Test data processing	37
4.3.1 Interpretation of waterfall plots	38
4.3.2 MPU6050 test results (USBfan hard-mounted to ground)	40
4.3.3 MPU6050 test results (USBfan hard-mounted to mounting bracket)	42
4.3.4 Laser tests	44
5 Microvibration models	45
5.1 Empirical model	45
5.1.1 Harmonic numbers identification	48
5.1.2 Amplitude coefficient calculation	52
5.1.3 Mode removal	54
5.1.4 Comparison of model and data	55
5.2 Analytical model	60
5.3 Unified model	68
5.3.1 Numerical solution of the unified model	73
5.3.2 Parameter definition	77
5.3.3 CAD model	79
5.4 Laser displacement model	83

6	Validation of experimental data	89
6.1	Identification of frequency ranges for comparison	89
6.2	PiFan 3.3V tests and models comparison	90
6.3	PiFan 5V tests and models comparison	92
6.4	USBfan tests and models comparison.	95
6.5	Other requirements	97
7	Conclusions and recommendations	99
7.1	Requirement Verification Matrix	99
7.2	Conclusions.	101
7.3	Recommendations	103
	Appendices	105
A	Additional test results	107
A.0.1	MPU6050 test results (PiFan 3.3V hard-mounted to ground)	107
A.0.2	MPU6050 test results (PiFan 3.3V hard-mounted to mounting bracket)	108
A.0.3	MPU6050 test results (PiFan 5V hard-mounted to ground).	110
A.0.4	MPU6050 test results (PiFan 5V hard-mounted to mounting bracket)	111
B	Additional unified model results	113
B.1	PiFan 3.3V.	113
B.2	USBfan	115
C	Additional laser displacement model results	117
C.1	PiFan 3.3V.	117
C.2	PiFan 5V	118
	Bibliography	121

List of Figures

1.1	Static Imbalance	3
1.2	Dynamic Imbalance	3
1.3	Flow diagram of the thesis report	8
2.1	Concept generation for test bench and measurement approach [5][14][20][31][32][33][34]	12
2.2	Graphical trade-off for the test approach concept selection	13
2.3	Graphical trade-off for the measurement approach concept selection	14
2.4	Requirements Discovery Tree	15
2.5	Functional and non-functional system requirements of the mounting bracket, tests and models systems	17
2.6	High-level architecture of the thesis project, representing the key inputs/outputs of the tests and models	18
3.1	Imbalance measurement of a roller bearing cylinder by Sui et al. [20]	21
3.2	Complete test setup for accelerometer testing (MPU6050 taped to top base)	24
3.3	Complete test setup for laser testing (MPU6050 detached from top base) – Pi-Fan	25
3.4	Test setup for ground-fixed accelerometer testing (MPU6050 taped to the fan) – Pi-Fan	25
3.5	Bent parts after 3D printing	26
3.6	Drilling holes into the 3D printed bases	27
3.7	Change of top parts	28
3.8	Schematic representation of working principle of the mounting bracket	29
4.1	Arduino circuit diagram, as used in the tests (PiFan powered with 3.3V)	35
4.2	Example of serial monitor output of the <code>RPM_accelerometer.ino</code> sketch (USBfan-Acc.log)	36
4.3	Interpretation of waterfall plots	39
4.4	Test results: Force-time plots of the ground-fixed USBfan	40
4.5	Test results: Waterfall Force plots of the ground-fixed USBfan	40
4.6	Test results: Torque-time plots of the ground-fixed USBfan	40
4.7	Test results: Waterfall Torque plots of the ground-fixed USBfan	41
4.8	Test results: Force-time plots of the USBfan mounting bracket	42
4.9	Test results: Waterfall Force plots of the USBfan mounting bracket	42
4.10	Test results: Torque-time plots of the USBfan mounting bracket	42
4.11	Test results: Waterfall Torque plots of the USBfan mounting bracket	43
4.12	Determination of minimum time of accelerometer shaking for laser tests. USBfan a_x data. . . .	44
5.1	High-level workflow of the empirical model - Example with F_x disturbance as input	47
5.2	Harmonic number identification block	48
5.3	Example of amplitude spectrum in frequency and order domain for the USBfan F_y data (@1281.5RPM)	49
5.4	Noise identified in histogram bin and eliminated below Disturbance Threshold. USBfan F_y data (@1281.5RPM)	50
5.5	Amplitude coefficient calculation block	52
5.6	Least Squares Approximation model and data - USBfan F_y data	54
5.7	Example of mode removal at $h_1=0.388$. $C_{1old} = 1.2575e - 6kgm$; $C_{1new} = 2.0463e - 7kgm$. $Pearson_{old} = -0.2368$; $Pearson_{new} = -0.4532$. Pi-Fan 5V F_x data.	55
5.8	Amplitude spectrum comparison of experimental data and empirical model. USBfan F_y data.	56
5.9	Power Spectral Density comparison of experimental data and empirical model. USBfan F_y data.	57
5.10	Data vs Empirical model: Peak Amplitudes and cumulative RMS comparisons. USBfan F_y data (@1283 RPM).	59
5.11	Data vs Empirical model: Total RMS over speed comparison. USBfan F_y data.	59

5.12	Analytical model of the balanced test setup	60
5.13	Coordinate frames and Tait-Bryan rotations	61
5.14	Analytical model of the unbalanced test setup	66
5.15	Vibrating modes of the mounting brackets and fundamental harmonic	71
5.16	Example of transmissibility function of the USB mounting bracket	72
5.17	Unified model results: Force-time plots of the PiFan 5V mounting bracket	76
5.18	Unified model results: Waterfall Force plots of the PiFan 5V mounting bracket	76
5.19	Unified model results: Torque-time plots of the PiFan 5V mounting bracket	76
5.20	Unified model results: Waterfall Torque plots of the PiFan 5V mounting bracket	77
5.21	Translational mode of the PiFan mounting bracket (15.06Hz)	79
5.22	Rocking mode of the PiFan mounting bracket (32.36Hz)	80
5.23	Translational mode of the USBfan mounting bracket (13.85Hz)	80
5.24	Rocking mode of the USBfan mounting bracket (30.68Hz)	81
5.25	CATIA's Harmonic Dynamic Response results - PiFan bracket	82
5.26	CATIA's Harmonic Dynamic Response results - USBfan bracket	82
5.27	Laser displacement model	83
5.28	Example of usage of the <code>range_detector.py</code> script	85
5.29	Sample output frame of the <code>laser_tracking.py</code> script	85
5.30	Lens optics math: sensor and object plane proportions	86
5.31	Time-Force plot of the USB fan laser displacement model	87
5.32	Waterfall plot of the USB fan laser displacement model	88
6.1	Comparison of all tests and models. PiFan 3.3V F_x data	90
6.2	Comparison of all tests and models. PiFan 3.3V F_y data	90
6.3	Comparison of all tests and models. PiFan 3.3V T_θ data	91
6.4	Comparison of all tests and models. PiFan 3.3V T_ϕ data	91
6.5	Comparison of all tests and models. PiFan 5V F_x data	92
6.6	Comparison of all tests and models. PiFan 5V F_y data	93
6.7	Comparison of all tests and models. PiFan 5V T_θ data	93
6.8	Comparison of all tests and models. PiFan 5V T_ϕ data	94
6.9	Comparison of all tests and models. USBfan F_x data	95
6.10	Comparison of all tests and models. USBfan F_y data	95
6.11	Comparison of all tests and models. USBfan T_θ data	96
6.12	Comparison of all tests and models. USBfan T_ϕ data	96
6.13	Total cost of test bench components	98
7.1	Requirements Verification Matrix	100
A.1	Test results: Force-time plots of the ground-fixed PiFan 3.3V	107
A.2	Test results: Waterfall Force plots of the ground-fixed PiFan 3.3V	107
A.3	Test results: Torque-time plots of the ground-fixed PiFan 3.3V	108
A.4	Test results: Waterfall Torque plots of the ground-fixed PiFan 3.3V	108
A.5	Test results: Force-time plots of the PiFan 3.3V mounting bracket	108
A.6	Test results: Waterfall Force plots of the PiFan 3.3V mounting bracket	109
A.7	Test results: Torque-time plots of the PiFan 3.3V mounting bracket	109
A.8	Test results: Waterfall Torque plots of the PiFan 3.3V mounting bracket	109
A.9	Test results: Force-time plots of the ground-fixed PiFan 5V	110
A.10	Test results: Waterfall Force plots of the ground-fixed PiFan 5V	110
A.11	Test results: Torque-time plots of the ground-fixed PiFan 5V	110
A.12	Test results: Waterfall Torque plots of the ground-fixed PiFan 5V	111
A.13	Test results: Force-time plots of the PiFan 5V mounting bracket	111
A.14	Test results: Waterfall Force plots of the PiFan 5V mounting bracket	111
A.15	Test results: Torque-time plots of the PiFan 5V mounting bracket	112
A.16	Test results: Waterfall Torque plots of the PiFan 5V mounting bracket	112
B.1	Unified model results: Force-time plots of the PiFan 3.3V mounting bracket	113
B.2	Unified model results: Waterfall Force plots of the PiFan 3.3V mounting bracket	113

B.3	Unified model results: Torque-time plots of the PiFan 3.3V mounting bracket	114
B.4	Unified model results: Waterfall Torque plots of the PiFan 3.3V mounting bracket	114
B.5	Unified model results: Force-time plots of the USBfan mounting bracket	115
B.6	Unified model results: Waterfall Force plots of the USBfan mounting bracket	115
B.7	Unified model results: Torque-time plots of the USBfan mounting bracket	115
B.8	Unified model results: Waterfall Torque plots of the USBfan mounting bracket	116
C.1	Time-Force plot of the PiFan (@3.3V) laser displacement model	117
C.2	Waterfall plot of the PiFan (@3.3V) laser displacement model	118
C.3	Time-Force plot of the PiFan (@5V) laser displacement model	118
C.4	Waterfall plot of the PiFan (@5V) laser displacement model	119

List of Tables

1.1	Engine orders of single bearing imperfections	4
1.2	Research questions	6
3.1	Equipment used in the complete setup	23
4.1	Test plan	34
5.1	Empirical model parameters (1)	49
5.2	Empirical model parameters (2)	52
5.3	Coordinate frames names and Tait-Bryan transformation sequence for the fan test bench model	62
5.4	Static and dynamic imbalance values calculated by the <code>unified_model.m</code> script	75
5.5	Analytical and unified models: Parameter definition and origin	78
5.6	Translational and rocking modes calculated by CATIA for the mounting bracket and fan systems	81
5.7	System masses and principal moments of inertia calculated by CATIA	81
5.8	Isocell GW1 Sensor data	86
6.1	Frequency ranges within which the maximum peaks are taken for comparison	89

Nomenclature

BLDC	BrushLess Direct Current
BPF	Blade Pass Frequency
CRMS	Cumulative Root Mean Square
ESA	European Space Agency
I2C	Inter-Integrated Circuit
IMU	Inertial Measurement Unit
MEMS	Micro Electro-Mechanical Systems
MVMS	Micro Vibration Measurement System
ODE	Ordinary Differential Equation
PME	Precision and Microsystems Engineering
PQ	PocketQube
PSD	Power Spectral Density
RCF	Reaction Wheel Characterization Facility
RMS	Root Mean Square
RPM	Revolutions Per Minute
rps	Revolutions Per Second
SNR	Signal to Noise Ratio
STFT	Short-Time Fourier Transform

Introduction

In this chapter, the motivation for this research project is discussed, followed by background theoretical information on microvibrations. Then, the research objective will be formulated, together with some research questions, which are the basis this project will aim to answer to. At the end of the chapter, an overview of the thesis structure will be given.

1.1. Motivation

Reaction wheels often have several tiny imperfections that lead to the generation of microvibrations, also known as jitter. These microvibrations are usually the major contributor to pointing errors and, as such, they need to be limited, especially in missions with demanding pointing and high-resolution imaging requirements, such as Earth Observation, optic-based satellite communication, precise formation flying. A survey of problems caused by microvibrations in spacecraft, for example, has recently been published by NASA [1]. Causes of microvibration include – but are not limited to – rotor or flywheel mass imbalance, axis misalignment, ball bearing imperfections, and motor torque ripple.

This research project, hence, focuses on finding a method to measure microvibrations in small reaction wheels, in the scale of those of Delfi-PQ [2] and Delfi-n3Xt [3], and proposes three different models for comparison with the test data, that aim to predict vibration amplitudes and imbalance values. For this purpose, the main goal of this thesis was to design and validate a low-cost microvibration test bench prototype, which will be described in detail in chapter 3. Microvibration measurement setups are already quite established for bigger-scale reaction wheels, and they mainly consist of a reaction wheel hard-mounted on a Kistler dynamometer, fixed on a seismic base, as in the ESA Reaction Wheel Characterization Facility (RCF) [4]. However, due to budget or sensitivity constraints, test setups still need improvement for Cubesat-scale wheels and smaller ones, whose vibration amplitudes are much smaller than those of microsatellite (10kg and more) reaction wheels.

In particular, the most common microvibration measurement platform for reaction wheels, the Kistler 9236A [5], is provided by the manufacturer in two different sizes: $260 \times 260 \text{ mm}$ for the A1 version and $400 \times 400 \text{ mm}$ for the A2 version. The smallest distance between the mounting holes is 70 mm for the A1 version and 50 mm for the A2 version, which is already too much for mounting a tiny reaction wheel on top of it. The diameter of the Delfi-PQ RW, for example, is 14 mm , while the one of the Delfi-n3Xt RW is 20 mm . This means a heavy mounting adapter (with eigenfrequencies above the microvibration frequencies, to avoid resonances in this band) would be required to fix these RWs to the Kistler table. Furthermore, the sensitivity thresholds of these Kistler dynamometers need to be considered, to evaluate if they are suitable for measuring microvibrations in this scale. For the Delfi-PQ reaction wheel, the target microvibration measurement range was $[0.0186 - 2.807] \text{ mN}$ for radial forces and $[0.0034 - 0.544] \text{ mNm}$ for torques, calculated by similarity with measurements on a Cubesat reaction wheel [6]. On the other hand, for the Kistler 9236A, coupled with a Kistler 5080A multichannel amplifier [7] for data acquisition, a dynamic response threshold of 20 mN is reported in the user manual [8], which is the lowest change in force that can be detected by this setup during measurement. Even the European Space Agency's RCF facility, based on Kistler load cells 9250A4, would be unable to measure microvibrations in the Delfi-PQ range, as minimum amplitude thresholds of 4.5 mN (forces) and

1.8mNm (torques) were measured [4]. Only the newest ESA facility, the Micro Vibration Measurement System (MVMS), would be able to measure forces and torques down to 0.01mN and 0.01mNm [9]. Therefore, that would comply with the force requirement for tiny wheels, but not the torque requirement. Furthermore, the MVMS relies on an extremely complex and expensive system, consisting of a vibration isolation platform made up of seismometers, to decouple the vibration load from ground vibrations, and keep the background noise very low. Thus, the Kistler tables on the market are not suitable for measuring microvibrations of tiny reaction wheels.

Therefore, the main motivation behind the design and validation of this test bench is to provide universities or Cubesat manufacturers with a measuring method for microvibrations that both aims to cut costs and improve sensitivity compared to industrial setup. This research also aims to be a reproducible source of ideas for possible future iterations on this scientific approach for vibration measurement.

Exclusively as a means to validate the test bench, microvibrations were not measured on a proper reaction wheel (due to malfunctions explained in section 3.3.3), but rather on two small PC cooling fans, whose central bodies have respectively a 7.5mm and 21.7mm radius. Beware that this does not mean that fans are the object of this research, but rather that they represent a simplified method of validation for the test bench prototype, due to their similarity with reaction wheels. The reason behind this choice will be better explained in the next chapters.

A brief introduction to microvibration theory will follow in the next paragraphs of this chapter, to get acquainted with the main parameters of this field.

1.2. Microvibration theory and definitions

Microvibrations are periodic disturbances that generally occur in the frequency range 1 – 1000 Hz.

The main sources of micro-vibrations are identified in the literature [10][11] as the following: rotor or flywheel imbalance, ball bearing imperfections, and torque ripple. The flywheel imbalance is generally the largest disturbance source [11], while the torque ripple is generally a cause of motor driver errors (high-frequency phase switching of the stator) [10, p. 12]. Microvibrations are generally analyzed in the frequency domain, as they can be modeled as discrete harmonics (sine functions) with amplitudes proportional to the wheel speed squared. Alternatively, they can be transformed into the order domain, where the frequencies are normalized by dividing them by the wheel speed. A harmonic number, or harmonic order, is defined as the ratio of frequencies and wheel speed, and it's especially convenient because many types of microvibrations (such as imbalance, which generally happens once per revolution, and thus has order 1) have the same harmonic order across their whole speed range, while frequencies generally change linearly with speed. A very common way to represent microvibrations is waterfall plots, where the microvibration amplitudes are 3D plotted in frequency or order domain, with frequencies/orders and speed (RPM) in the x and y axes, respectively. A more in-depth explanation of these concepts will follow in the next chapters.

In the next paragraphs, a basic explanation of the principles underlying the three main sources of microvibration will be presented.

1.2.1. Flywheel imbalance

The major cause of microvibrations in a reaction wheel is imbalance. Imbalance is a characteristic of the wheel that arises during the manufacturing process. Due to the impossibility of any manufacturing process to produce a part with a completely even distribution of mass, there will always be an offset (or eccentricity) between the axis of inertia (where the center of mass lies) and the axis of rotation of the wheel. Therefore, imbalance is an unavoidable characteristic of the wheel, which is present (however small) in any system composed of a motor, shaft, and flywheel, and can only be decreased by homogenizing the mass distribution of the flywheel, but not completely eradicated. A more formal definition of imbalance will follow.

A common reference frame that can be defined for a reaction wheel has the x and y axes in the plane of rotation of the wheel and the z axis coinciding with the axis of rotation of the wheel, as in Figure 1.1, where an analogous ground-fixed frame (before Euler rotations to a body-fixed frame - see section 5.3) is drawn. Hence, the micro-vibrations produced by the wheel can generally be decomposed into three force components (F_x, F_y, F_z) and three moment components, or torques (T_x, T_y, T_z).

There are two main types of imbalances: static and dynamic imbalance. A static imbalance is caused by an uneven distribution of mass in the plane of rotation (middle section of the flywheel). This can be seen as an *offset* between the axis of rotation and the axis of inertia (Figure 1.1).

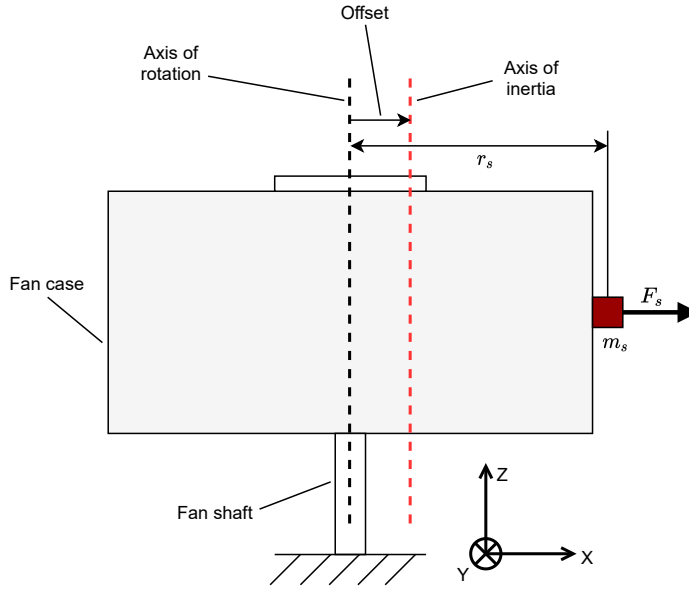


Figure 1.1: Static Imbalance

Mathematically, the static imbalance is represented by the equation:

$$U_s = m_s r_s \text{ [gcm]} \quad (1.1)$$

Where m_s is the static imbalance mass and r_s is the distance between the axis of rotation and this mass. The imbalance thus generates a centrifugal force during rotation:

$$F_s = m_s r_s \Omega^2 \quad (1.2)$$

Where Ω is the flywheel rotational speed.

This force is measured in the x and y components (F_x, F_y), and it has order $h = 1$ since it repeats itself once every rotation.

A dynamic imbalance, instead, is caused by an uneven distribution of mass in planes parallel to the plane of rotation. This results in an *angle* between axis of rotation and axis of inertia (Figure 1.2).

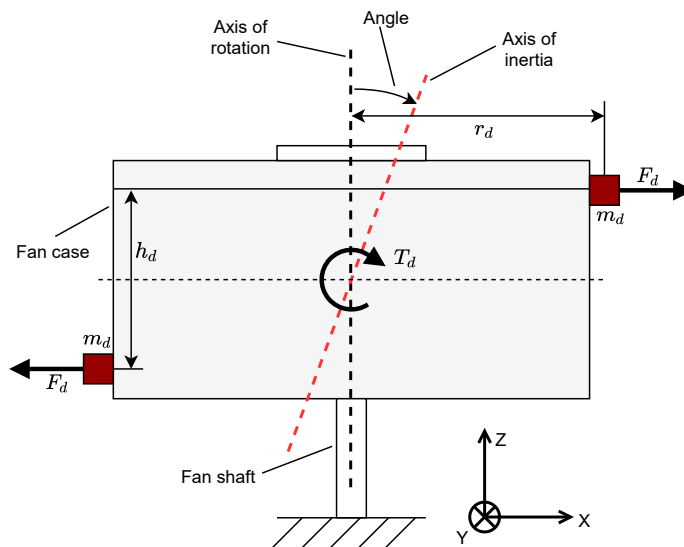


Figure 1.2: Dynamic Imbalance

In formulas, the dynamic imbalance is:

$$U_d = 2m_d r_d h_d \text{ [gcm}^2\text{]} \quad (1.3)$$

Where m_d is the dynamic imbalance mass, r_d is the distance between the axis of rotation and this mass, and h_d is the distance between the two dynamic imbalance masses.

This generates a couple of centrifugal forces during rotation, i.e. a torque:

$$T_d = 2m_d r_d h_d \Omega^2 \quad (1.4)$$

This torque is also observed in the x and y components (T_x, T_y) and has order 1.

The definitions of these imbalances will be useful throughout this project, especially in the writing of the unified model, in section 5.3. Also, it will be better explained later on that the major focus will be on these types of disturbances, as they are the ones that the mounting bracket can capture better. Microvibrations due to imbalance, as a matter of fact, are often by far the greatest reaction wheel disturbances, while those due to bearing imperfections or torque ripple are usually very close to the noise floor.

1.2.2. Ball bearing imperfections

Imperfections in ball bearings can be of three types:

1. **Manufacturing:** manufacturing imperfections can be further divided into two subcategories:
 - Geometric imperfections: local irregularities on the surface of bearing parts. These cause impulses when they come in contact with other bearing parts
 - Waviness: deviation of the shape of the balls from an exactly spherical shape (out-of-roundness).
2. **Structure:** bearing and surrounding structure can resonate under the excitement caused by other imperfections. This is known as structural vibration.
3. **Handling:** contamination and imperfections can be introduced during the integration process. The causes of imperfection include mechanical impacts during verification tests.

All these imperfections have specific harmonic orders that can be determined from a kinematic model of the bearing. These orders are calculated as in table 1.1 [12], with the assumption of no-slip between bearing components, and for imperfections on single bearing parts (without the interference of multiple imperfections).

Inner Race Imperfection	$H_{IRI} = \frac{z}{2} \left(1 + \frac{d_b}{D} \cos(\alpha) \right)$
Outer Race Imperfection	$H_{ORI} = \frac{z}{2} \left(1 - \frac{d_b}{D} \cos(\alpha) \right)$
Cage Rotational Imperfection	$H_{CR} = \frac{1}{2} \left(1 + \frac{d_b}{D} \cos(\alpha) \right)$
Ball / Ball spin Imperfection	$H_{BI} = 2H_{BS} = \frac{D}{d_b} \left(1 - \left(\frac{d_b}{D} \cos(\alpha) \right)^2 \right)$

Table 1.1: Engine orders of single bearing imperfections

Where z is the number of balls, d_b is the ball diameter, D is the pitch diameter and α is the contact angle.

Besides the main engine orders reported in Table 1.1, there are additional orders called sidebands, which are a linear combination of multiple disturbances coming from other sources as well, such as flywheel imbalance.

1.2.3. Torque ripple

Torque ripple is a disturbance generated by the motor and it manifests itself as a non-uniformity in the torque around the rotation axis (T_z). Only deterministic (periodic) signals around the z axis are considered torque ripple, while other random disturbances are referred to as torque instabilities.

The causes of torque ripple in BLDC motors can be divided into three categories: motor nature, motor structure, and motor control [13]. Ripples related to motor nature are due to physical properties and parameters proper of the manufacturing materials of the motor. Therefore, their minimization depends on the selection of materials for the motor. Motor structure refers to the shape and dimensions of the motor and its components. Motor control indicates the control technique of the motor. This can be also acted upon in order to minimize the torque ripple.

1.3. Microvibration tests and models

In microsatellites and minisatellites, weighing 10kg or more, the techniques used for measuring reaction wheel microvibrations are quite established. There are two main types of microvibration tests: hard-mounted or coupled. In the hard-mounted condition, the wheel is rigidly mounted to a dynamometer table. The models, hence, consider only the dynamics of the wheel, measuring directly microvibrations at the source and ignoring the spacecraft. A widely used platform for these types of tests is the Kistler table [4], where 3-component force sensors are integrated into one dynamometer, making it possible to measure three forces and three torques. This is good for determining the microvibration signature of the wheel and for validating the wheel itself but gives no indication of its coupled behavior with the satellite it will be mounted on. For this reason, coupled models are built, where the dynamics of the satellite is taken into account and it is simulated in tests with a mechanically representative structure, such as a truss [14][15]. This is usually hung to a ceiling with ropes to simulate a free-free boundary condition, like the one imposed by micro-gravity in space. It is quite common then, in microvibration research, to develop a Finite Element Analysis of the reaction wheel or the wheel and spacecraft system, to obtain a Frequency Response Function and be able to simulate the transmission of vibrations at the interfaces [16][17]. Alternative types of tests include fixing the reaction wheel to a known seismic mass, in a cantilevered configuration [18]. This is an indirect measurement, as it requires a transfer function between the seismic mass and the wheel [19], and it's the same type of measurement used in this thesis. However, testing methods do not always have to include contact sensors, and novel ideas could be taken from different fields. For example, laser-based methods [20], including self-mixing interferometry [21], have been used for measuring vibrations, and this could be applied to reaction wheel microvibrations as well, provided that attention is paid to the bandwidth in which these instruments can operate.

As for the models, several studies have been done on reaction wheel dynamics, especially ball bearings, which are arguably the hardest part to be modeled. It is generally required to calculate the ball bearing stiffness, which has been simulated with several different equations [10][22][23]. Hybrid ceramic [24] or magnetically levitating [25] ball bearings have also been studied to reduce imperfections and friction respectively, and hence microvibrations. The calculation of the bearing stiffness makes it possible to have all input parameters for an analytical model [26], consisting of the equations of motion of the wheel. Empirical models, which are parameter estimation models aiming to approximate the harmonic orders and amplitude coefficients of the test data, are also very common [27][28], and their outputs are often also used to improve the analytical model. This results in an extended, or unified model, which is a validated method for predicting microvibration performance [29].

1.4. Research objective

The rectangle below contains the research objective of this thesis project. The research objective is a concise statement where the motivation behind this research, the objective of this thesis, and the way it is going to be achieved are summarized. As previously mentioned, the main goal of this thesis is to be able to measure microvibrations in nanosatellite-scale (satellites weighing less than 10kg) reaction wheels, which is achieved by validating a microvibration test bench. The validation of the test bench represents the *how* of this project, that is how the objective is going to be achieved. However, the *how* will be still design-independent at this stage, in order not to influence the concept selection. The object of research, the *what*, are microvibrations in the scale of nanosatellite reaction wheels. In the case of Delfi-PQ, for example, torque disturbances in the range of 0.0041Nm have been measured. The *why*, i.e. the motivation behind this objective, is the lack of a low-cost approach for accurate microvibration measurement in nanosatellite RWs, as stated in the motivation section (1.1).

Research objective:

This thesis aims to validate a microvibration measurement approach for nanosatellite-scale reaction wheels, given the lack of low-cost accurate approaches for these sizes, *by* prototyping a microvibration test bench and comparing the microvibration tests on this setup with at least one or more other types of measurement and models.

Therefore, due to the very small size of the motors, this project aims to contribute to an advancement in the body of knowledge of microvibration measurement, given that this kind of measurement is not standardized for these sizes yet (instrumentation with higher sensitivity is required compared to larger-scale wheels because the microvibration amplitude is smaller in this case). The low budget of the test bench will also be attractive for other projects of this scale since they are as frequent in universities as in industry right now, and academia often lacks the industrial instrumentation suitable for this purpose. Cubesat production is, in any case, oriented towards cost-saving solutions, for which this test bench could represent a good choice.

1.5. Research questions

Starting from the research objective and other considerations above, the following research questions have been formulated, and the rest of the project will be an attempt to answer these. The questions are listed briefly in table 1.2 and each of them is explained more in detail below the table.

Q1	Can a low-cost microvibration test bench be prototyped in-house?
Q2	Is it possible to measure in a systematic and reproducible way the microvibration signature of rotating (RW-like) objects in the order of the Delfi-PQ one ($[0.0186 - 2.807]mN$ forces and $[0.0034 - 0.544]mNm$ torques)?
Q2.1	Is it possible to measure the rotational speed of the rotating objects?
Q2.2	Is it possible to obtain microvibration plots in frequency or order domain?
Q2.3	Can the expected harmonic orders be identified in the test results?
Q3	Is it possible to calculate static and dynamic imbalances from the test results?
Q4	Can the test results be validated?
Q4.1	Is it possible to simulate the test results with models?
Q4.2	Is it possible to compare the test results with other types of tests?

Table 1.2: Research questions

Q1: In section 1.1, it was explained that one major motivation for the need of this project was that existing microvibration measurement setups are relatively expensive ($>20000€$ including Kistler dynamometer and charge amplifier, depending on specific solutions [30]) and often outside the budget of university departments or startups working on nanosatellites. Therefore, this question directly relates to this need, and the goal, as will be seen later in the requirements, is to cut prices by approximately 200 times.

Q2: This question specifies what exactly should be measured. That is microvibration forces in the range $[0.0186 - 2.807]mN$ and torques in the range $[0.0034 - 0.544]mNm$. The general term rotating object is used in the question since it is expected that microvibrations analogous to the ones produced by reaction wheels

can be measured even with simpler objects – for the verification of the test bench – as long as these objects are composed of, among others, a motor, shaft, and flywheel, and hence have a certain static and dynamic imbalance. The question also asks whether these measurements can be done in a systematic way, that means, according to a test plan, and in a reproducible way, meaning that the plan and approach proposed can be followed by someone else in the future to retrieve the same kind of results.

Q2.1: The sub-questions of Q2 list the parameters that must be obtained in order to be able to answer Q2. In this sub-question, it is asked whether the rotational speed (or angular velocity) of a rotating object can be measured. Wheel speed is an important parameter in microvibration results because data are often plotted in 3D graphs, called waterfall plots, representing frequency and speed in the (x-y) plane and microvibration amplitude in the z plane. An alternative to speed in waterfall plots is time. However, speed is often preferred in order to determine at what speeds exactly the wheel presents the greatest peaks. Speed in waterfall plots has a unit of RPM (revolutions per minute) or rps (revolutions per second).

Q2.2: This sub-question is also related to what was explained in the previous paragraph. In other words, it also asks whether it is possible to represent the measured microvibrations in waterfall plots. This time, the specified parameters are frequencies or harmonic orders, two domains in which vibrations are often studied since peaks are more easily distinguishable compared to the time domain. The harmonic order domain is equal to the frequency domain divided by the rotational speed of the wheel (both in Hz), and therefore harmonic orders are dimensionless numbers.

Q2.3: These harmonic orders are known in certain cases, like imbalances which have harmonic order 1 (since they repeat once per revolution), or they can be predicted analytically as seen for ball bearing imperfections. This sub-question then asks whether vibration peaks can be seen in the waterfall plots at these expected values of orders.

Q3: Even though Q3 also lists important microvibration parameters, this question was formulated separately from Q2, since imbalances, as opposed to the previous parameters, are not directly measurable during tests or visible in waterfall plots, but require post-processing on the amplitude coefficients. It is however related to Q2.3 since in order to answer to Q3 one should be able to answer positively to Q2.3 first, meaning that order 1 should have been identified in the test results.

Q4: While previous questions dealt with tests and post-processing of the test data only, this question deals with models, and hence the validation of the test bench and test approach by comparison and model and test data. More specific requirements for validation will follow in the requirements section 2.2.

Q4.1: This sub-question specifically asks whether the test results can be predicted by models and whether the two can be compared to each other.

Q4.2: This sub-question specifically asks whether the proposed test approach can be compared to one or more other measurement approaches on the same object of measurement. This represents a further term of comparison, besides the models and the main approach, to verify whether at least one measurement approach can be validated.

1.6. Thesis structure

In this section, a flow diagram representing the thesis structure is shown in figure 1.3. In each block, the title of a chapter is written and the arrows connecting different blocks show the main inputs and outputs of each chapter and their relationship. A concise summary of the content of each chapter can be found below the figure.

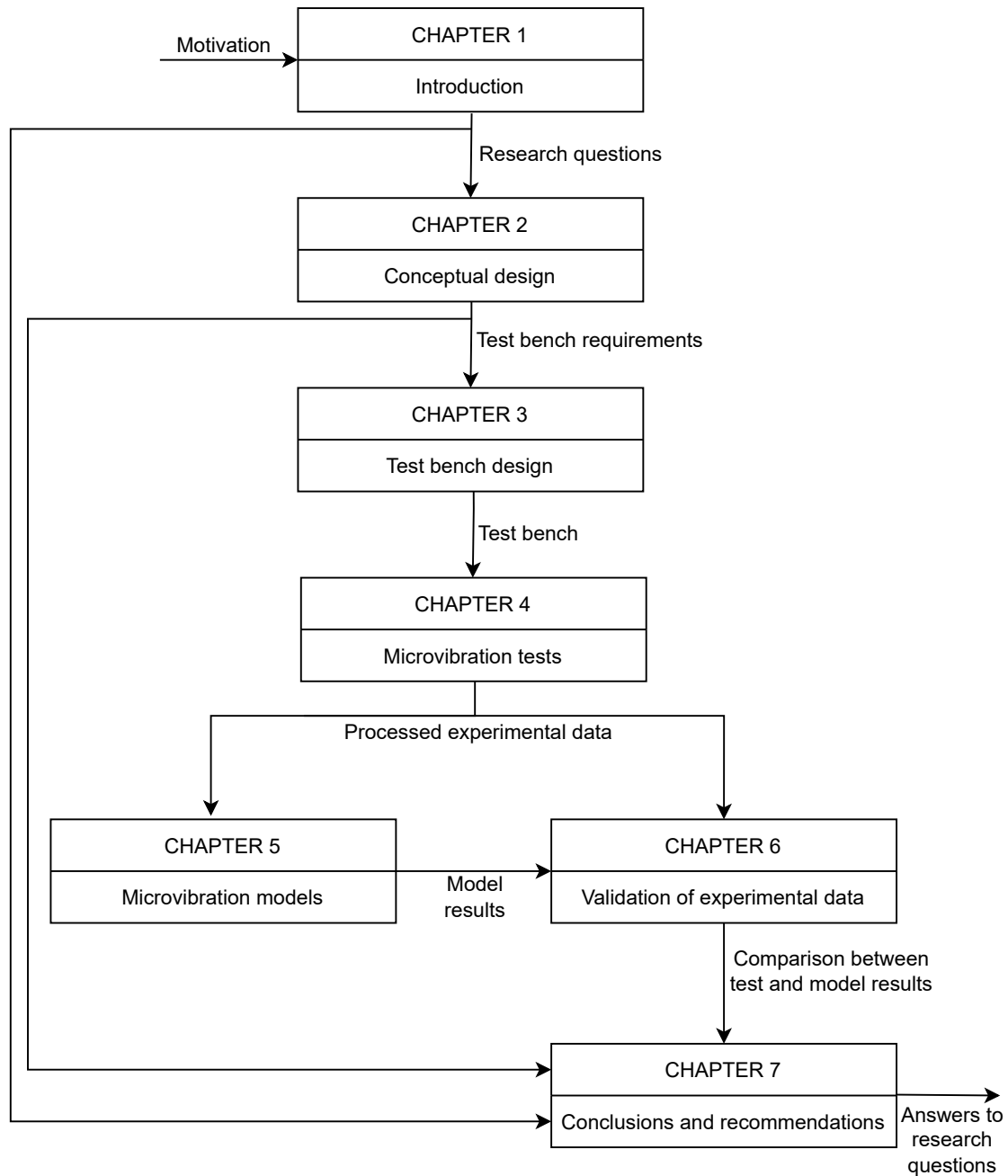


Figure 1.3: Flow diagram of the thesis report

Since chapter 1 ends with this section, the summary is going to start with chapter 2. The main output of chapter 1, as can be seen in the figure above, are the research questions (1.5).

Chapter 2 contains a high-level, conceptual design of the microvibration test bench. This will start with a generation of concepts for different types of test bench approaches and sensors. Then, three concepts will be selected based on a graphical trade-off, according to certain criteria. Afterward, requirements will be laid

out by generating a Requirements Discovery Tree, linking the research questions to technical requirements. Finally, the actual list of requirements will be shown in a matrix, and a high-level architecture of the test and modeling approaches will be presented.

Chapter 3 is going to describe the final design of the test bench prototype, including a list of equipment, the production and all related problems, and the scientific working principle of the test bench. Failed attempts, that happened in the initial stage of the practical implementation of this project, and the respective lessons learned will also be included.

In chapter 4, first a test plan is described. Then, the Arduino wiring, code, and outputs are discussed. The post-processing of the raw data in MATLAB is then explained, followed by the final results, in the form of waterfall (Frequency-RPM-Amplitude) and time-amplitude plots.

Chapter 5 contains the full development of the microvibration models, including an empirical model, which is a harmonic identification and parameter fitting model of the test data, and an analytical model, where the equations of motion of the test bench are simulated. The two models will then be merged into a single, unified model. A more in-detail explanation will follow in that chapter. Lastly, a laser displacement model will be described, which consists of the object identification and post-processing of the recorded videos of the laser reflection during tests.

In chapter 6, then, a comparison between test and model results is shown, by means of RPM-Amplitude plots at specific frequency ranges. From these plots, compliance or non-compliance of tests, models, or test bench with the corresponding requirements is deduced. Other requirements, not related to this comparison, will also be discussed.

The final chapter (7) shows the final requirements verification matrix summarizing the status of compliance of the current systems. Then, conclusions will be drawn by answering each research question. Finally, recommendations will be given on future lines of action.

2

Conceptual design

In this chapter, a preliminary concept selection for the test bench will be performed, based on the research questions. The technical implementation of the selected concept will follow only in the next chapter so that the requirements can be solution-independent at this stage. Then, system requirements are going to be derived, starting from the research questions outlined in section 1.5. These include functional and non-functional requirements for test bench, test approach and results, and microvibration models. To do this, a Requirements Discovery Tree will be built, linking each research question to specific functions, related to the final system requirements. Each requirement will also be justified with a brief rationale.

Following the requirements, a conceptual map will be shown to outline the main test and modeling functions of this thesis project and their mutual relationships, including inputs and outputs. This map will give more technical insight to the reader compared to the previous thesis structure in figure 1.3 and will prepare for the reading of the test and model chapters (4,5,6).

2.1. Test approach concept selection

Based on the motivations for this thesis brought in section 1.1, on the review of test approaches in 1.3, and on the research questions in 1.2, high-level concepts for the test approach will be proposed in this section, without delving into the design of the test bench, so that a basis can be provided for system requirements before implementation is performed. In other words, the concept selection will try to determine through a preliminary qualitative analysis which scientific approach is likely to respond better to all research questions, but says nothing about its technical details, which will be given in chapter 3. First all possible concepts will be shown and then the final concept will be selected via a graphical trade-off.

Figure 2.1 shows the generated concepts for the test approach.

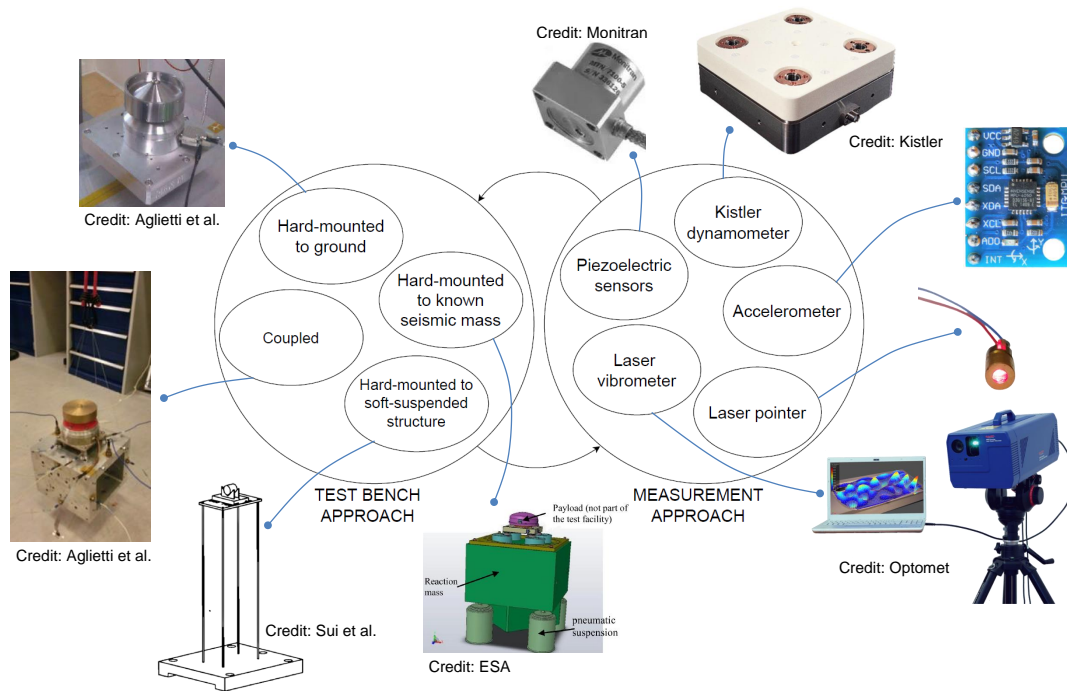


Figure 2.1: Concept generation for test bench and measurement approach [5][14][20][31][32][33][34]

As seen in figure 2.1, the main different types of microvibration tests are grouped in the left circle. On the right, instead, different types of measurement approaches, or sensor families, are grouped. The meaning of the arrows between the two groups is that any item inside any of the two groups can be linked to any item of the other group, generating a unique concept. Two of these combinations will be selected to be able to answer Q4.2, which asks that results from more than one type of test be compared.

The difference between hard-mounted and coupled approaches was explained in section 1.3, including conditions in which the RW is hard-mounted to the ground (or better a heavy table) or to a known seismic mass. The case "hard-mounted to soft-suspended structure" is quite similar to the seismic mass one, but it differs from it in how the supporting structure is built. A soft suspension is a material with low stiffness, inside the microvibration frequency range (1-1000Hz) that crosses its resonance zone during tests so that vibrations can be amplified. An example of this is given by the mounting bracket presented in an article by Sui et al. [20]. This allows cutting the cost on the measurement approach, which can even consist, in principle, of commercial off-the-shelf electronics operated by cheap microcontrollers. However, the dynamics of the supporting structure must also be considered in this case and a transmissibility function must be found between it and the reaction wheel. Furthermore, this structure is likely to be excited only by the greatest microvibration peaks of the reaction wheel, that is those due to imbalances, which normally happen at lower frequencies (those equal to the reaction wheel angular speed). On the other hand, the peaks due to bearing imperfections, for example, happening at higher frequencies, will probably not be amplified by this type of structure and therefore they will not be read correctly by cheap sensors.

As for the sensors, the limitations of the Kistler dynamometers for these sizes of RWs have already been explained in the introduction. The alternative use of piezoelectric sensors or accelerometers has been mentioned. In some cases, a laser Doppler vibrometer has also been used [20], capable of measuring displacements down to nm scale. A much cheaper but surely more inaccurate alternative is pointing a common laser on the RW or its supporting structure to approximate the displacement through its reflection.

Since a trade-off involving all possible combinations between test bench and measurement approaches would be too long and confusing, they will be treated separately: first, a trade-off will be performed on the test bench approach, with two selections, and then the same process will be repeated for the measurement approach. Four selection criteria have been decided based on the research question. It is clear that, given the motivations for this project, one criterion shall be *cost*, which can be applied to both concept groups. This is related to Q1. From Q2, it can be inferred that a second criterion is the measurable *disturbance range*. This can also be applied to the test approach because one concept allows the amplification of this range. From Q2.2 and Q2.3 it can be deduced that microvibrations should be measured in their entire frequency

range, hence another criterion is the sensor *bandwidth*, which is the frequency range in which it is capable of measuring vibrations. This applies to measurement approaches only, since it is a characteristic of the sensor. The last criterion is *complexity*, meaning how difficult the implementation of these approaches would be, as it would affect time as well. A rating among the following will be given to each concept according to each criterion: unacceptable (red); correctable deficiencies (yellow); good, meets requirements (blue); excellent, exceeds requirements (green). In the test approach, all three criteria are given the same weight, because of their very similar importance related to the research questions, while in the measurement approach, which presents the risk of being extremely expensive, the cost criterion is given 40% weight, and the other three criteria 20% each.

Criterion Concept	Cost (33.3%)	Disturbance range (33.3%)	Complexity (33.3%)
Hard-mounted to ground	No additional cost other than sensor green	Not amplified by test bench (high-resolution sensor required) yellow	No additional test bench component other than measurement setup blue
Hard-mounted to known seismic mass	Development of a heavy seismic mass (high material cost) red	Not amplified by test bench (high-resolution sensor required) yellow	Dynamics of known seismic mass included in the calculations yellow
Hard-mounted to soft-suspended structure	Low to very low (depending on suspension design) blue	Amplified by test bench green	Dynamics of structure included in the calculations yellow
Coupled	Development of the satellite-representative structure yellow	Slightly amplified by free-free conditions (medium/high-resolution sensor required) blue	Dynamics of structure + free-free conditions included in the calculations red

Figure 2.2: Graphical trade-off for the test approach concept selection

According to figure 2.2, the two concepts that are going to be selected are *hard-mounted to ground*, and *hard-mounted to soft-suspended structure*. The hard-mounted condition to the ground is in fact the easiest and cheapest option to implement in this list, due to the fact that it doesn't include other mechanical equipment, such as a support structure, as opposed to other options. The risk, in this case, is that cheap sensors selected for the measurement approach will not suffice to measure the vibrations of tiny wheels accurately. That is why the hard-mounted condition to a soft-suspended structure is also selected. The disturbance range will be amplified by the supporting structure, making it possible to select cheaper sensors and still capture the range accurately. On the other hand, some cost will be foreseen for the development of the supporting structure (prototype), although it will be kept as low as possible at this stage, and it is surely lower than that of a truss representing the spacecraft or a seismic mass.

The results of the two concepts can be compared between each other after the ones of the soft-suspended approach are divided by the transmissibility function of the supporting structure to obtain the source disturbances.

Criterion \ Concept	Cost (40%)	Disturbance range (20%)	Bandwidth (20%)	Complexity (20%)
Kistler dynamometer	>20k€ (excessive, unless already available) red	Minimum: $\approx 0.002\text{N}$ blue	>2kHz green	Learn yellow dedicated SW; huge amount of data
Piezoelectric sensors	Medium-low, >50€ (depending on solution) yellow	Minimum: $\approx 0.01\text{N}$ (depending on solutions) blue	>1kHz blue (depending on solution)	blue Programmable with a microcontroller
Accelerometer	Low, < 50€ (depending on solution) blue	Minimum around 0.2N (depending on solutions) yellow	Up to around 1kHz (depending on solution) yellow	blue Programmable with a microcontroller
Laser Vibrometer	>20k€ (excessive, unless already available) red	Minimum: <10nm green	Around 10kHz green	Learn yellow dedicated SW; huge amount of data
Laser pointer	Extremely low (<10€) green	Variable, depending on mirror reflectance and video resolution (only usable with soft-suspended test bench) red	Variable, depending on mirror reflectance and video resolution red	green Simplest module (plug-and-play)

Figure 2.3: Graphical trade-off for the measurement approach concept selection

Regarding the selection of the measurement approach, bear in mind that an attempt to use either a laser vibrometer or a Kistler dynamometer as the first concept was made initially, due to the fact that they were both available at TU Delft. Hence, the cost wouldn't have been a problem in this case, and it would have still been possible to comply with the research objective by comparing their output to results from a low-cost sensor (the second concept) and validate this last (low-cost) test bench. However, both attempts to work with the vibrometer or with the dynamometer failed, due to constraints that will be explained in section 3.3.3.

Therefore, *accelerometers* were the first option selected in this case, due to their low cost, the ease of implementation, and the acceptable deficiencies on measurable disturbance range (which could be partly made up for by the soft-suspended approach) and bandwidth. The idea is to use a low-cost accelerometer module, which can be simply programmed with a microcontroller. The design will follow in chapter 3. Piezoelectric sensors could have also been a good choice, but they are generally a bit more expensive than accelerometers (depending on specific solutions), and the approach would be very similar to the first concept: to fix a contact sensor either on the RW and the supporting structure. Therefore, it was decided not to select them, and to try a different approach instead: the *laser pointer*. This, however, will be a viable option only with the soft-suspended approach, with the laser pointing at a mirror on the supporting structure, since the measurable disturbance range of the laser will surely not be enough for a ground-fixed RW. Therefore, even though

the disturbance range appears unacceptable for this concept, it is expected to become at least acceptable with the soft-suspended case and provide at least qualitative results to compare with the accelerometer ones. The bandwidth remains the major risk in this case, as it is expected that the laser will not be able to capture high-frequency disturbances. However, since the focus of Q3 is on static and dynamic imbalances, it is expected that the laser will be able to capture at least their harmonics since they will be the ones that are more amplified (on purpose) by the supporting structure.

To summarize, the three combinations of selected approaches are:

1. Accelerometer on reaction wheel hard-mounted to ground
2. Accelerometer on soft-suspended structure, with reaction wheel hard-mounted on top
3. Laser pointing to a mirror on soft-suspended structure, with reaction wheel hard-mounted on top

These approaches will be described in detail in the following chapters and also correspond to the tests selected in the test plan (table 4.1).

2.2. Mounting bracket, tests and models requirements

This section is going to report all requirements relative to the mounting bracket (both for testing and simulation), that will be necessary to validate it and answer research questions.

First of all, a Requirements Discovery Tree is shown in figure 2.4, where the research questions are summarized in blocks and they are linked to related actions, that will directly convert into technical requirements.

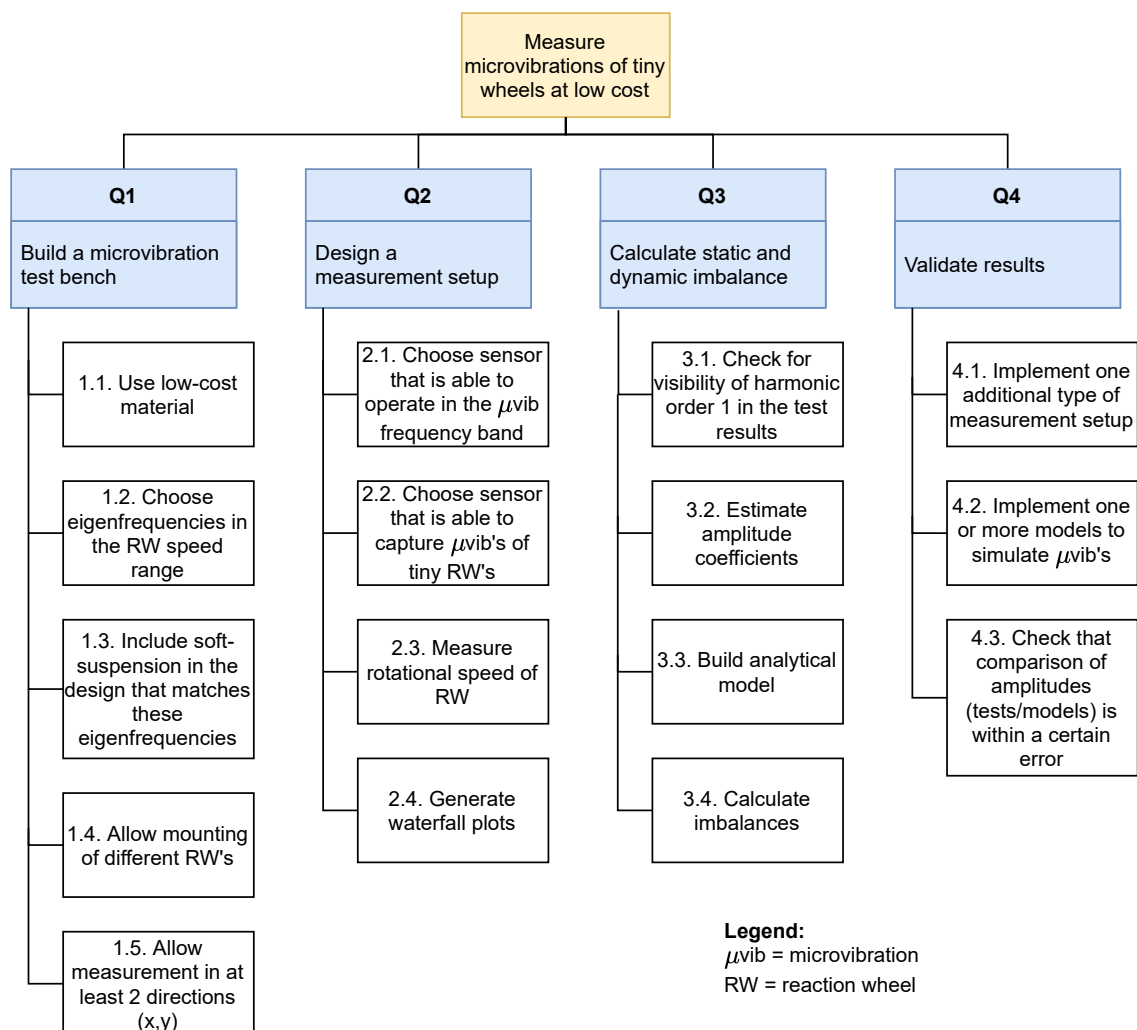


Figure 2.4: Requirements Discovery Tree

The yellow block at the top represents the research objective, while the four blue blocks represent the research questions. Non-trivial blocks are going to be explained hereafter. 1.2 and 1.3 relate to the previously selected soft-suspended approach: eigenfrequencies of the test bench shall be chosen in the wheel speed range to let it operate in its resonance zone and amplify vibrations. 1.5 asks for the possibility to measure vibrations in just two directions, since in the z direction (the one of the rotation axis) the movement of the reaction wheel would probably be constrained by the test bench and axial stiffness and damping are generally harder to model for the suspensions compared to radial ones. So the goal is to measure forces and moments just in radial directions. Child blocks of 2 were already explained in the concept selection. 3.1 asks for the presence of order 1 in the results. Recall that this is the order of static and dynamic imbalances, so amplitudes at that order shall be estimated (3.2) to calculate imbalances (3.4). That is done by solving the equations of motion of an analytical model (3.3) with the estimated amplitudes as external forces. The validation asks for one additional type of measurement approach (4.1), and that is why the laser concept was also selected, besides the accelerometer. The models (4.2) will serve as further terms of comparison for the validation.

The technical system requirements are shown in figure 2.5. Each requirement has a requirement identifier (or ID), which is an alphanumeric code that uniquely identifies the requirement. The ID is made up of three parts, divided by hyphens. The first identifies the system: MB stands for mounting bracket, TES for tests, MOD for models. The second part identifies the nature of the requirement: F stands for functional, meaning that it's a requirement inherent to the capabilities of the system, NF for non-functional, meaning that it's a requirement inherent to the characteristics of the system. The third part is made of three digits, to distinguish the requirement.

The second column, labeled requirement description, contains the actual requirement statements. Each requirement will be related to a block of the Requirements Discovery Tree, in column three. Furthermore, a verification method will be written for each requirement in column four, including one or more of the following: A for analysis, D for demonstration, I for inspection, and T for testing. A brief rationale, stating the motivation for the existence of each requirement and the relationship to the Requirements Discovery Tree blocks will be included in the fifth and last column.

REQUIREMENT ID	REQUIREMENT DESCRIPTION	RELATED REQUIREMENT BLOCK	VERIFICATION METHOD	RATIONALE
MB-NF-001	The total fixed costs of all test bench components shall be less than 200€	1.1	I	Cheap accelerometer modules and other simple electronics, microcontroller and 3D-printed test setup are expected to cost no more than 150€. Margin is added.
MB-NF-002	At least one of the eigenfrequencies of the test bench shall be inside the speed range of the fans	1.2	A	This is to let the test bench operate in its resonance zone and amplify the vibrations.
MB-NF-003	The mounting bracket shall contain a soft-suspension made of flexible materials to facilitate the amplification of vibrations	1.3	D	This is related to MB-NF-002, in that the soft suspension's low stiffness is what makes the system's eigenfrequency low (in that range).
MB-F-001	The mounting bracket shall be able to be fixed to different types of wheels, with diameter within its maximum dimension	1.4	D	More than one wheel is expected to be tested.
MB-F-002	The mounting bracket shall allow microvibration measurements for at least two forces (Fx, Fy) and two torques (Tx, Ty), where x and y are the radial plane of the fan	1.5	T,A	Movement in the z-direction is expected to be constrained by the soft suspension design. Axial stiffness is difficult to be modeled.
TES-F-001	It shall be possible to generate waterfall plots from the tests results, with the disturbance amplitude plotted along the frequency or harmonic order spectrum and the fan speed	2.4	T,A	Waterfall plots are the most common method to visualize microvibrations.
TES-F-002	The sensor used in the test bench for microvibration measurements shall be able to measure disturbances in the 1-500Hz frequency band	2.1	I,T	Microvibrations occur in the 1-1000Hz band. However, since the majority of them happen below 500Hz anyway and to allow for a cheap sensor, the requirement has been relaxed.
TES-F-003	The sensor used in the test bench for measuring microvibrations shall be able to measure disturbance forces in the range [0.0186-2.807]mN	2.2	T,I	This range comes from the expected disturbances of the Delfi-PQ RW. The amplification of the test bench must be taken into account: amplitudes will have to be divided by transmissibility before comparing with this range.
TES-F-004	The sensor used in the test bench for measuring microvibrations shall be able to measure disturbance torques in the range [0.0034-0.544]mNm	2.2	T,I	Same as TES-F-003.
TES-F-005	The fan rotational speed shall be measured with a maximum uncertainty of ± 10 RPM	2.3	T,I	Cheap sensors like a hall-effect sensor are able to measure high rotational speeds within a few RPM's. Some margin is added, and 10 is in any case an acceptable value to know the wheel state without jeopardizing validation.
TES-F-006	The harmonic order 1 shall be visible in the mounting bracket test waterfall plots in order domain	3.1	I	The harmonic order 1 is the one of static and dynamic imbalance disturbances. In order to calculate the imbalances, peaks at order 1 should be visible.
TES-NF-001	At least one more type of microvibration test shall be performed, whose results can be compared to those of the mounting bracket	4.1	T	Another measurement approach is desired to be able to compare different results from different types of tests, provide more than one measurement concept, and validate the first concept.
TES-F-006	The waterfall plots generated by other types of tests shall be compared to the mounting bracket test results with a maximum error of 30% at any given frequency and speed	4.3	T,A	A high margin for error is included in this requirement. At this prototyping stage, it should be considered that peaks from different tests or models are not always perfectly aligned at the same speeds/frequencies (for sensor resolution or modeling problems), so it can be made stricter at later iterations.
MOD-F-001	At least one of the models shall be able to calculate the static and dynamic imbalance of the fans	3.4	A	Microvibration empirical and analytical models are generally implemented in research for the validation of test results.
MOD-F-002	The models shall be able to generate waterfall plots, comparable to those of the tests	4.2	A	Same as TES-F-001.
MOD-F-003	The waterfall plots generated by the models shall be compared to the mounting bracket test results with a maximum error of 30% at any given frequency and speed	4.3	A	Same as TES-F-006.

Figure 2.5: Functional and non-functional system requirements of the mounting bracket, tests and models systems

2.3. High-level architecture of the test and modeling approach

In this section, a high-level architecture of the experimental and modeling part of this thesis project is shown in figure 2.6, including key blocks, corresponding to specific scripts used for tests and simulations. It provides more insight on what will be done in the next chapters compared to the thesis structure in figure 1.3, but it still doesn't dive into details and it limits itself to showing relationships between each block and their most important inputs and outputs so that the reader can start to get acquainted with some recurrent parameters. Each block is then going to be thoroughly explained, especially in chapters 4 (tests), 5 (models), and 6 (final comparisons).

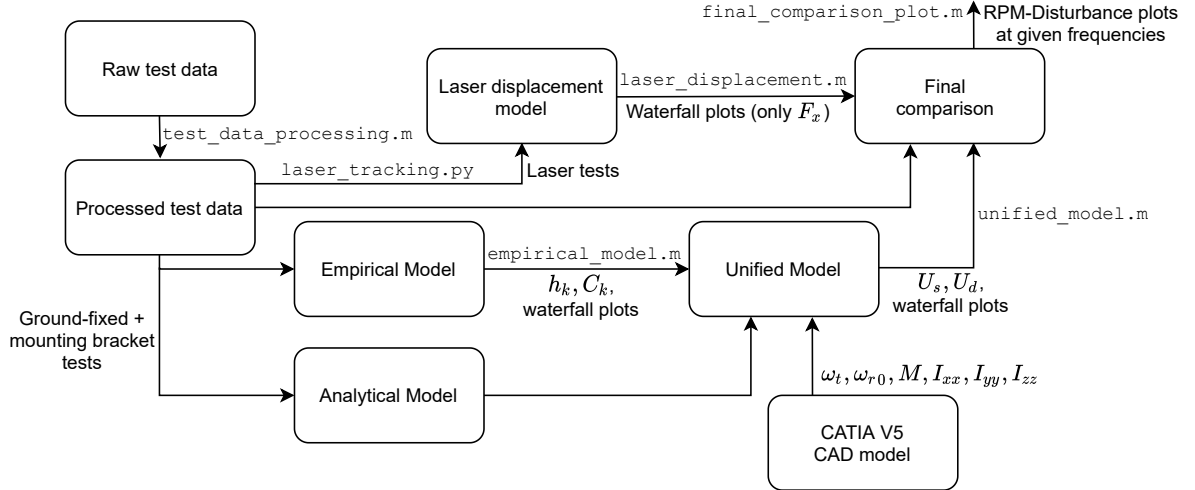


Figure 2.6: High-level architecture of the thesis project, representing the key inputs/outputs of the tests and models

All parameters in figure 2.6 are going to be discussed in detail later on, and only a brief description is listed below:

- h_k : Harmonic orders
- C_k : Amplitude coefficients
- U_s : Static imbalance
- U_d : Dynamic imbalance
- M : Mass of fan + bracket top base + iron bars (system)
- I_{xx} Principal moment of inertia of the system around x
- I_{yy} Principal moment of inertia of the system around y
- I_{zz} Principal moment of inertia of the system around z

As mentioned earlier, the goal of this thesis is to validate the mounting bracket test bench by comparing the test results with other types of tests or models. These are all shown in the conceptual map.

First, the raw test data are retrieved, with three main types of microvibration test:

1. Accelerometer measurement, with the accelerometer taped to the mounting bracket top base, and fan fixed on top of the bracket
2. Accelerometer measurement, with the accelerometer taped to the fan, and fan taped to the ground
3. Recorded video of a laser dot displacement, reflected by a mirror fixed on the mounting bracket top base

The purpose of having two types of accelerometer tests is to verify the transmissibility of the mounting bracket, that is the amplification factor from source disturbances (at the fan) to mounting bracket top base disturbances. Therefore, by dividing the disturbance amplitudes of the mounting bracket test by the ones of the ground-fixed test, it should be possible to calculate transmissibility. Alternatively, by dividing the amplified disturbances by the transmissibility, an approximation of the ground-fixed (source) data can be calculated. The laser displacement test, instead, can directly be compared to the corresponding mounting bracket test, after due processing, since it captures the same displacement of the mounting bracket top base. Its limitation is that one laser reflection can only capture disturbances in one direction, hence only forces F_x will be compared.

From all these tests, waterfall plots will be generated, that can directly be compared with all following models.

The first model is commonly called empirical model. This is based on the assumption that a microvibration is a sum of harmonics, where the k^{th} harmonic has harmonic order h_k and amplitude $C_k\Omega^2$, where C_k is called amplitude coefficient and Ω is the fan speed (in rps or Hz). This is formally written in equation 5.1. Therefore, the whole model is based on parameter estimation from experimental data, in order to calculate these two sets of parameters, h_k , and C_k . The waterfall plots generated with the modeled amplitudes can directly be compared to the ones of test data. However, the empirical model alone is not sufficient to validate microvibration measurements with the mounting bracket, since it is solely based on test data.

Therefore, an analytical model is built, taking into account the dynamics of the mounting bracket and fan system and the imbalances of the fans, as described in paragraph 1.2.1. The main results of the analytical model are the equations of motion, where the static and dynamic imbalances are the external forces on the right-hand sides of the equations.

This model is then modified by taking inputs from the empirical model, and substituting the static and dynamic imbalance disturbances with the empirical model disturbances, given that the values of static and dynamic imbalance are not previously known. This is called unified model. The unified model also takes inputs from a CATIA V5 CAD model, in particular eigenfrequencies, masses, and moments of inertia of the test bench.

By solving the differential equation system formed by the equations of motion, two translational and two rotational displacements can be derived, which, multiplied by the radial or torsional stiffnesses, give forces and torques respectively. Also, the static and dynamic imbalances can be calculated.

It should be noted that particular emphasis was given to disturbances due to imbalances. This is due to the fact that mounting bracket measurements aim to capture that type of disturbance. As a matter of fact, the brackets are built in such a way that their natural frequencies overlap with the fan rotational speeds, thus entering the resonance zone and amplifying vibrations (up to around 200 times). A transmissibility function can then be calculated to derive the source disturbances. Therefore, since the vibrations that are amplified are exactly those that occur at the fan speeds, it is expected to have the biggest disturbances at order 1 (the order of the imbalances) in the results. Other orders will probably not be captured well, including those corresponding to bearing imperfections or torque ripple, since they will either be in the static or damping zone of the transmissibility function.

In other words, the main results of this project will be the static and dynamic imbalances, and the corresponding waterfall plots. The laser measurement is expected to serve as a first quick test, to check for example if imbalances were reduced after mitigating actions, even by visual inspection. Then, the unified model could give insight into how much these imbalances are.

Test bench design

Since the main focus of the thesis is the validation of the test bench, this chapter is going to report in detail how the mounting bracket was built and all the problems related to this process. At the end of the chapter, the working principle behind the setup is explained.

3.1. Soft-suspended test bench concept

The idea of the test bench design follows from the test and measurement approach concept selections in figure 2.2 and 2.3. The selected test approaches, in particular, were reaction wheel hard-mounted to ground and reaction wheel hard-mounted to a soft-suspended structure. Since the first concept requires no mounting bracket for the RW, the only product that has to be designed is the soft-suspended test bench. An example of a low-cost soft-suspended mounting bracket, which partially inspired the test bench design for this project, can be found in the article by Sui et al. [20]. Their work is shown in figure 3.1.

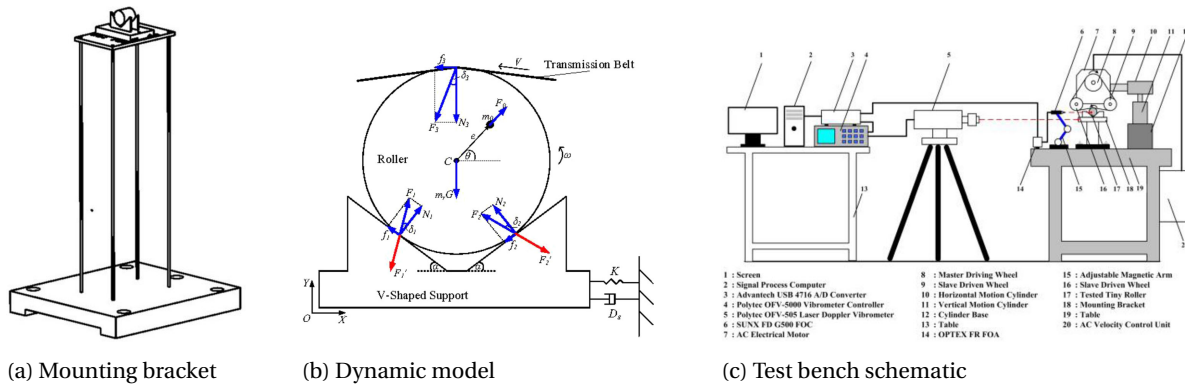


Figure 3.1: Imbalance measurement of a roller bearing cylinder by Sui et al. [20]

In their design, a transmission belt drives a roller bearing cylinder, which transmits vibrations to the mounting bracket via friction, as shown in figure 3.1b. Vibrations are later measured at the mounting bracket top base by a Polytec Laser Doppler Vibrometer (figure 3.1c). However, the unwanted vibrations coming from the transmission belt were identified as a major source of error in microvibration testing. Furthermore, at the interface between transmission belt and roller, the rolling was not ideal, meaning that the intensity of the transmission belt's pressure against the roller was most likely not constant, making it very hard to model friction accurately. This resulted in a discrepancy between test data and simulations, where at certain speeds the test data were about 16 times greater than the models. So, while a concept based on soft suspensions should in principle work, it is recommended to change the type of interface between wheel and bracket, and avoid the transmission of vibrations via friction.

In the case of wheels driven by an embedded motor, like reaction wheels, there is no need for a transmission belt. Hence vibrations don't have to be transmitted via friction, but through contact (the base of the wheel is hard-mounted on the top base of the bracket, with its axis of rotation perpendicular to the contact

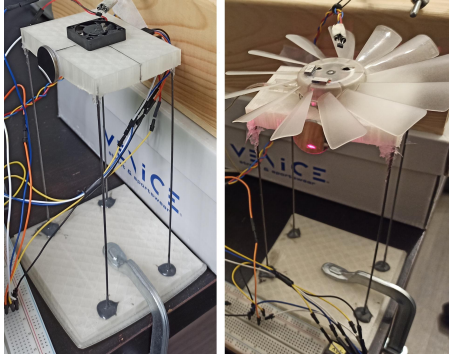
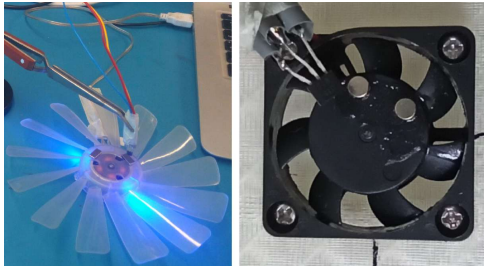
surface). The bracket will still amplify vibrations thanks to the soft suspensions (iron bars), making it possible to operate the bracket in its resonance zone, due to their selected low eigenfrequencies inside the wheel speed range. Furthermore, as mentioned in the introduction and in section 3.3.3, two small fans were used instead of an actual reaction wheel. The reasons for this choice are explained in paragraph 3.3.4. Therefore, the same concept of the mounting bracket was modified in order to fit these, and for each of them, a different top base was 3D printed.

The innovation that the work in this thesis project will bring to microvibration literature lies in the fact that such a test bench has never been used before with reaction wheels. Nevertheless, it is expected to be a viable approach for two reasons. First, a modification of the mounting bracket, that consists in changing the type of interface as explained above, is expected to improve results significantly, since friction was identified as the main problem in the results of the roller bearing. Second, there is no need to actually use an expensive Laser Doppler Vibrometer. Since the soft suspensions (the iron bars) amplify vibrations by around 200 times (see section 3.3.2), low-cost sensors with lower resolution are considered to be sufficient for this approach. This is why this approach was chosen in the concept selection, together with low-cost accelerometer and laser modules, in order to comply with the research objective.

As a matter of fact, due to the impossibility of using a laser vibrometer (see section 3.3.3), two new measurement concepts were selected. The first one is to mount an accelerometer to the bottom of the top base (where the displacement is at its maximum) and directly read displacements through it. The second one is to point a laser to a mirror fixed on the top base in order to capture displacements from the laser reflection. The various types of tests that were thought with these methods will be further explained in the test plan (4).

3.2. Equipment

The table below (3.1) is a complete list of the equipment used in the test setup and is sufficient to replicate all the tests that were performed within this project. These are Hardware components only. Commonly used or optional items are excluded from this list, namely: breadboard, jumper wires, switch, double-sided tape, hook and loop tape, and tweezers. Software is excluded and will be further explained in the tests chapter (4).

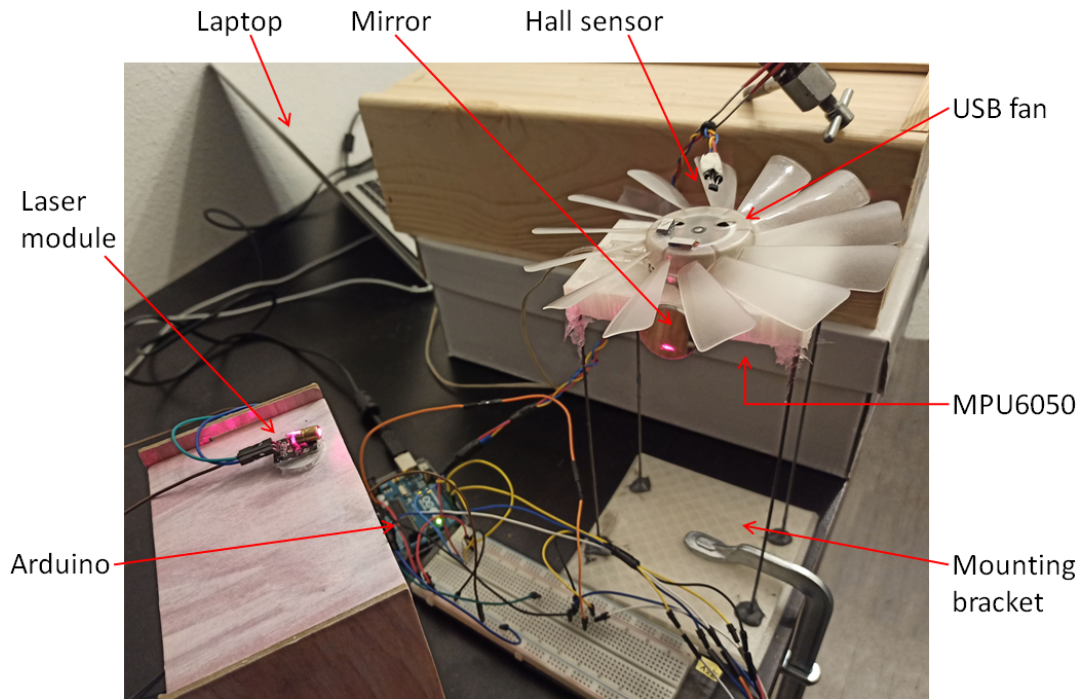
Part name	Picture/Description
3D Printed Mounting bracket (4 iron bars + 3 PLA parts)	
USB fan [left] PiFan (LD3007MS) [right]	

Hall effect sensor (US1881) [left] Neodymium magnets [right]	
25mm CO2 Molybdenum laser reflector (mirror) [left] 650nm Laser module KY-008 [right]	
MPU 6050 Accelerometer+Gyroscope module [left] Arduino Uno [right]	
Laptop	Macbook Air Mid 2011

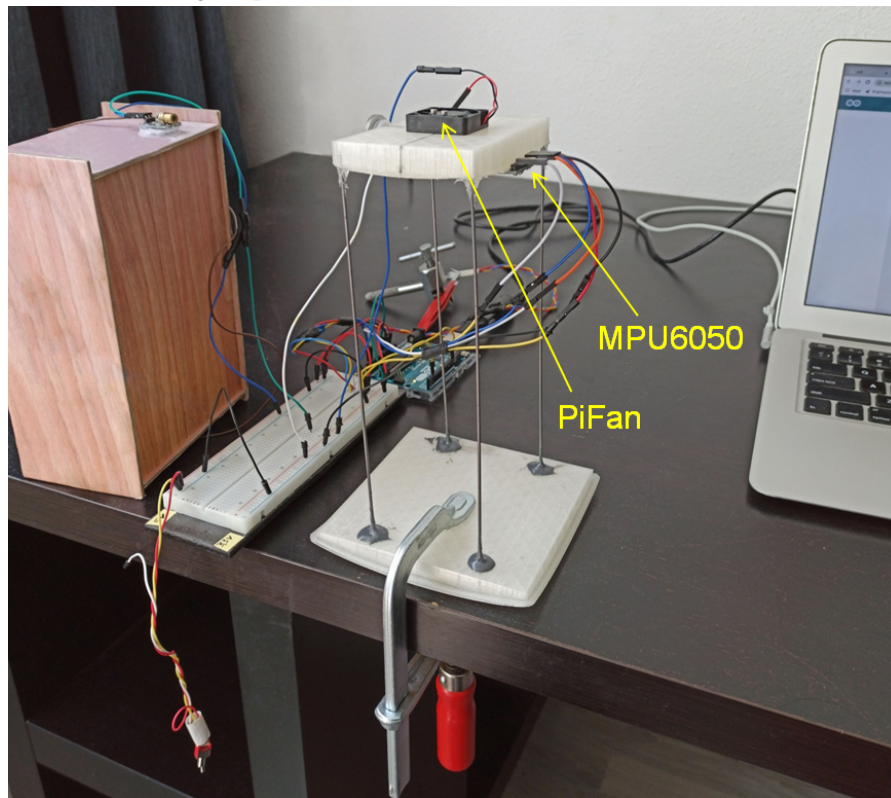
Table 3.1: Equipment used in the complete setup

3.3. Setup

In figures 3.2, 3.3 and 3.4 the complete setups used for the tests are shown. The setups in figures 3.2a and 3.2b will correspond to the "Accelerometer - Mounting bracket" test in the test plan (table 4.1), meaning that the measurement of accelerations and angular velocities is done by the MPU6050 at the mounting bracket top base (with a soft-suspended approach), to later calculate the source disturbances at the fan via a transmissibility function. The laser will be turned off during this type of test. The setup in figure 3.3, instead, corresponds to the "Laser displacement" test, though which displacement (also at the mounting bracket top base) is estimated via a laser tracking script. The MPU6050 will be detached from the top base during this type of test, and shaken together with the beginning of the laser reflection recording, to determine the starting time of the video. Finally, setup 3.4 represents the "Accelerometer - Ground-fixed" test, where the MPU6050 measures disturbances directly at the source. The MPU6050 here is taped to the fan case and the fan is taped to a table (ground). However, this last test produced very noisy results and was soon discarded, because vibrations are not amplified in a ground-fixed approach, and therefore amplitudes were lower than the sensor's noise threshold.



(a) USB fan MPU6050 testing setup



(b) Pi-Fan MPU6050 testing setup

Figure 3.2: Complete test setup for accelerometer testing (MPU6050 taped to top base)

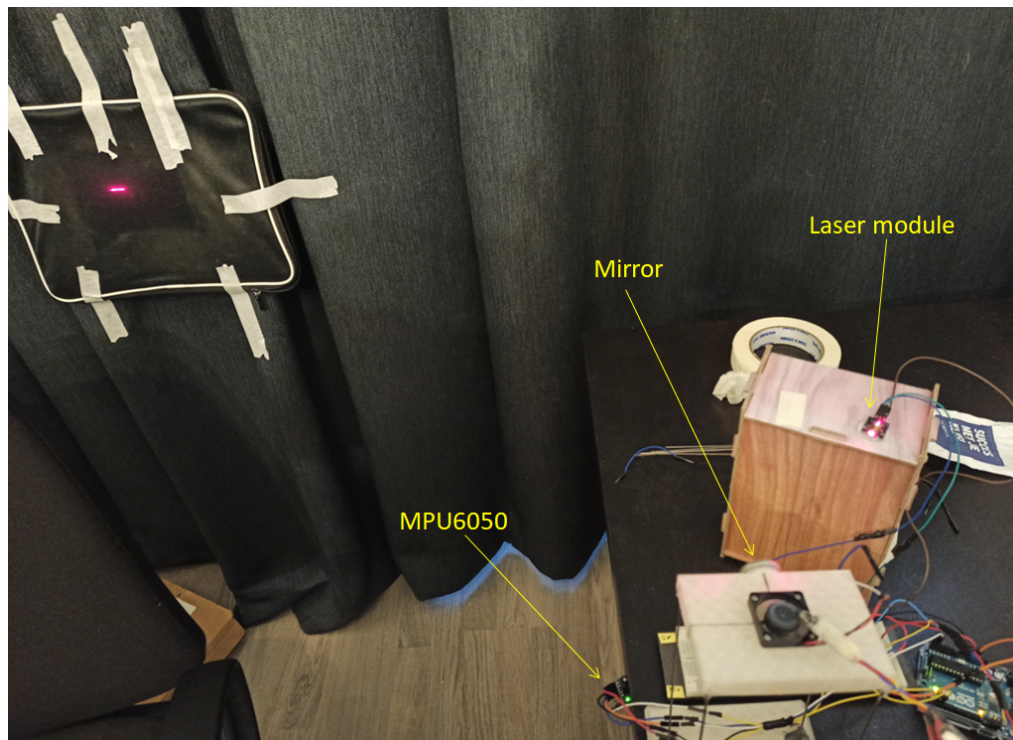


Figure 3.3: Complete test setup for laser testing (MPU6050 detached from top base) – Pi-Fan

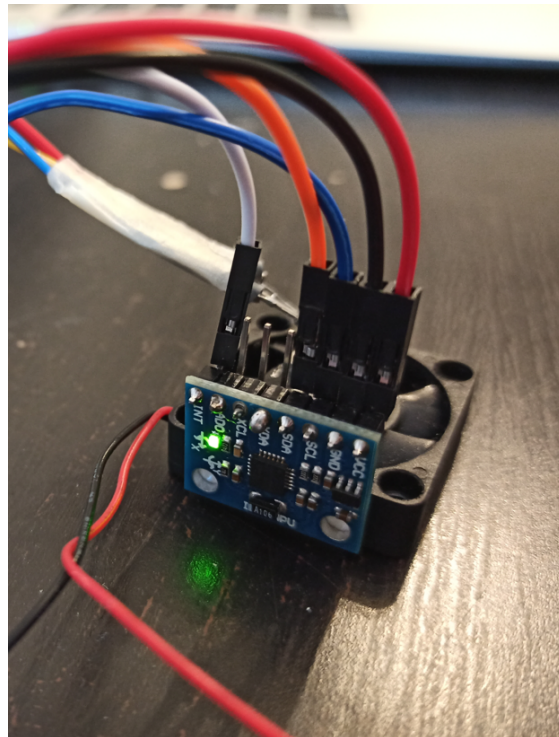
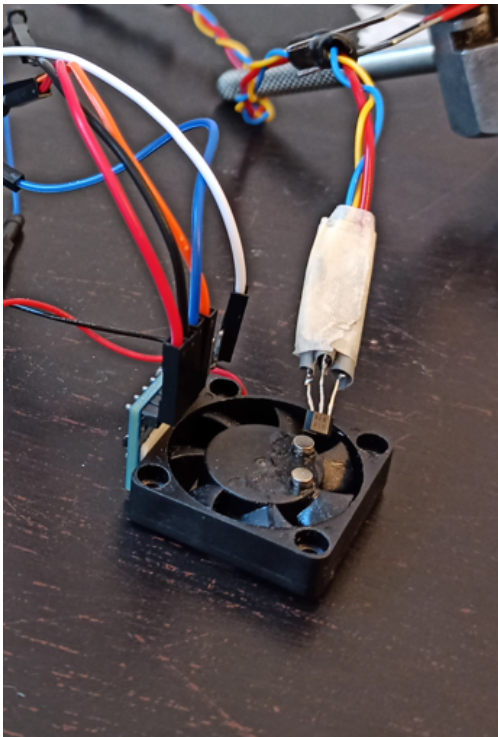


Figure 3.4: Test setup for ground-fixed accelerometer testing (MPU6050 taped to the fan) – Pi-Fan

3.3.1. Production

The mounting bracket was produced entirely in-house, with the MakerBot 3D printer of the Space Systems Engineering department. Three pieces were 3D printed in PLA: the bottom base and the two top parts, which are interchangeable. One id used to fit the Pi-Fan and the other one to fit the USB fan.

The first problem in the production was that during 3D printing, due to the fact that the filament was very hot and distributed on a large surface, the structure bent at the edges, as shown in figure 3.5.

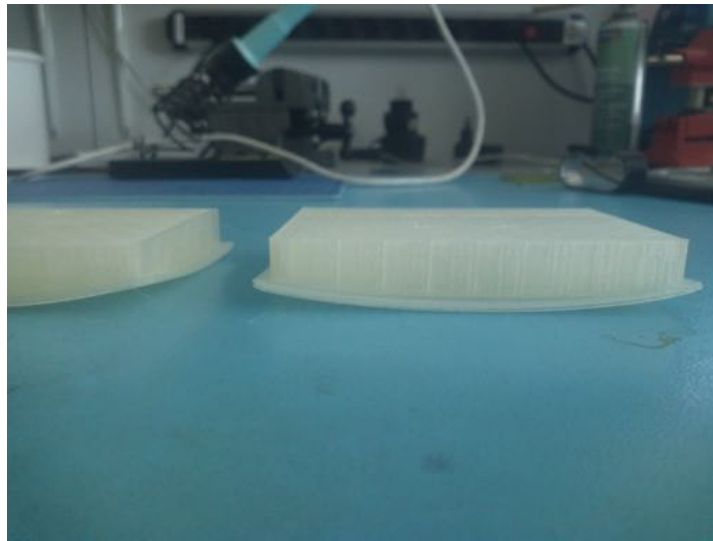


Figure 3.5: Bent parts after 3D printing

The lack of uniformity of the bottom surface may have influenced the final results since the base needs to be firmly fixed to the ground to let vibrations transfer only to the top one (as desired) and not the bottom one. To make up for this problem, hook and loop tape was used on the bottom of the base (on the part of the surface which was still not curved) and on the table, and the bond was additionally secured by a vise, as can be seen in fig. 3.2. This should be sufficient, since, due to the length and elasticity of the iron bars, the amplitude of vibrations is much greater and visible with the naked eye in the top base, while the bottom base stays still, so the transmission of vibration between the two bases is considered negligible. However, in the future, it is recommended to work with an even-surfaced, heavier base, possibly fastened to a table with screws.

After printing the above-mentioned bases, they were filed to remove major inaccuracies in the edges, and four holes were drilled in the bottom base and the two top bases, to accommodate the iron bars. This was done with the drilling machine in the Space Systems Engineering workshop, as can be seen in figure 3.6.

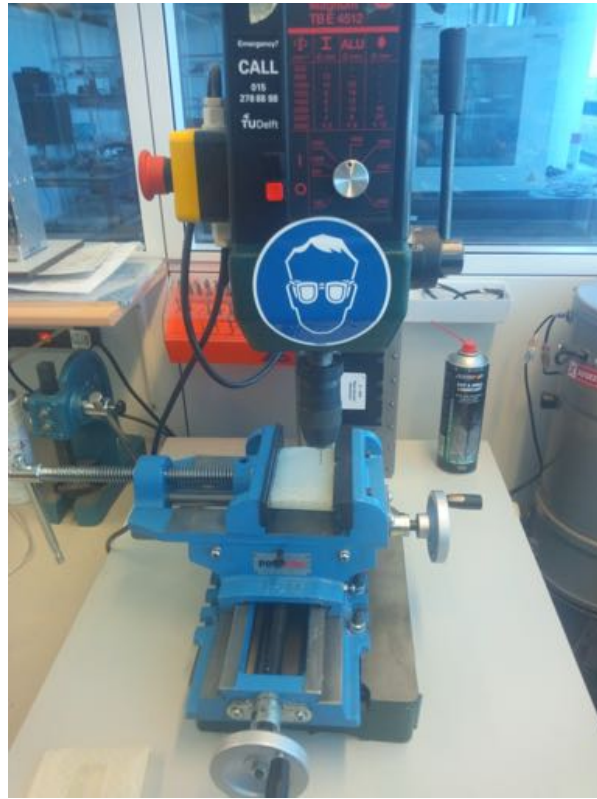


Figure 3.6: Drilling holes into the 3D printed bases

Due to the partly hollow structure of the 3D printed parts, some holes ended up being larger (and/or deeper) than others, as they encountered a hollow part inside the base. This was not considered to be a major issue and was simply made up for by applying more resin or silicone (as explained in the next paragraph) to the holes. However, for an optimal design, it is recommended in future products to use a denser structure for the bases so that identical holes can be drilled and a perfectly symmetrical structure for the iron bars can be obtained.

Four 20 cm iron bars were fixed with epoxy resin to the bottom part, as can be seen in figure 3.2. The upper part of the iron bars was fixed with a silicone sealant to the top part, as can be seen in figure 3.7 so that a connection between the parts is provided while allowing to replace the top parts whenever necessary (in case other fans/wheels want to be tested).

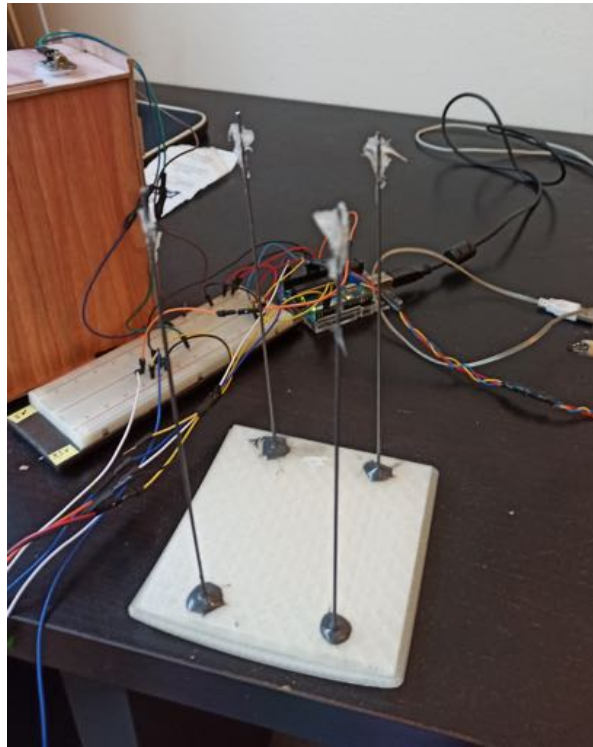


Figure 3.7: Change of top parts

Both the epoxy resin and the silicone must rest for at least two days to provide their maximum fastening. Nevertheless, since silicone is in principle not suitable as a structural bond (e.g. to bear heavy loads), this also may have had small influences on the displacement during vibrations and hence on the final results. It was used anyway due to the fact that the structure is extremely light and the effect of vibrations on the silicone should be negligible. This allowed to save some time for printing and assembling another mounting bracket. However, in the future, it is recommended to fix the upper of the iron bars to the top part with epoxy resin as well, to ensure a hard bond. An alternative, in order to have both a hard structural bond and replaceability of the top base, could be to redesign the iron bars so that the top extremities are threaded (for example by gluing a hollow screw to an edge of the existing iron bars). This way they could be inserted into through holes in the top base and fixed with nuts on the other side.

3.3.2. Working principle

The basic working principle of the 3D printed mounting bracket is quite simple: amplifying vibrations and obtaining the original ones via a transfer function from the disturbances (forces/moments) on the accelerometer (i.e. on the top base) to the ones on the rotating body (the input or source disturbances). The transmission of vibrations at the interface happens through contact since the fans are hard-mounted on the top base of the mounting bracket and excite the bracket directly. So, in this case, the fan and the top base can be ideally treated as a single body, even though the flexibility of the screws will not make it so in the real case.

What excites the mounting bracket is in fact the microvibrations produced by the wheel on top of it. Recall that the major sources of microvibrations from wheels are static imbalance (figure 1.1), which produces a centrifugal force, and dynamic imbalance (figure 1.2), which produces a couple of centrifugal forces (torque). Figure 3.8 shows a simple schematic of how the wheel's imbalance excites the designed mounting bracket. The dashed lines represent the static position of the system, while the full lines represent the generic perturbed position. The radial stiffness (in the x direction) of the system is represented by k , and it corresponds in reality to the four iron bars. The top base of course is not really connected to the ground on its side, but the representation is equivalent, as the rigidity of the four iron bars constrains the movement of the base along the x direction. The same goes for the damping, c .

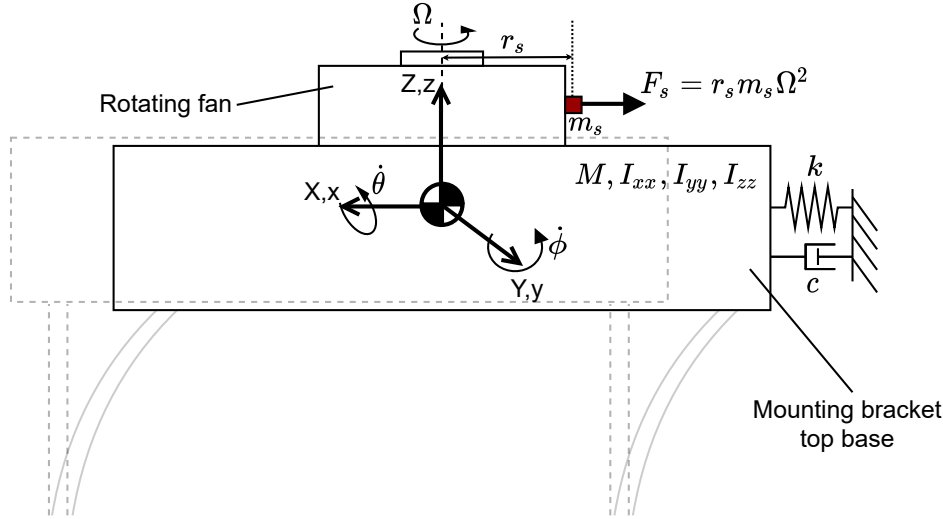


Figure 3.8: Schematic representation of working principle of the mounting bracket

The bracket is designed so that its eigenfrequencies lie in the range of the wheel's rotational speed (in Hz). The bracket is then expected to operate around its resonance zone when excited by the wheel, and amplify vibrations up to around 200 times, according to the transfer function in equation 3.3, and later shown in results in figure 5.16. This value can be derived by substituting the calculated test bench eigenfrequencies, together with other necessary parameters, as explained later, into the transfer function. A preliminary calculation of the translational eigenfrequency of the system was performed analytically and later confirmed by a frequency analysis on CATIA V5 (figures 5.21 to 5.24). The analytical calculation was performed as follows: the stiffness of the iron bars can be approximated as the stiffness of a cantilever beam with a load applied on its free far side, perpendicularly to the beam, which is known to be:

$$k = 3 \frac{EI}{h^3} \quad (3.1)$$

Where E is the Young Modulus of iron, equal to approximately $210GPa$, I is the area moment of inertia of a circular section, equal to $\pi D^2/64$, where D is the diameter of the bar ($1.6mm$) and h is the height of a bar ($20cm$). Since the iron bars are in parallel and are assumed to have all the same stiffness, the equivalent stiffness of the system is the k above multiplied by 4. The translational natural frequency of the mounting bracket can then be estimated as:

$$\omega_t = \frac{1}{2\pi} \sqrt{\frac{k_{eq}}{m}} \quad (3.2)$$

Where $k_{eq} = 4k$ is the equivalent stiffness and m is the mass of the system, which in the case of the PiFan setup is $208g$. The result, in this case, is only $3.51Hz$, which is low, as expected, but lower than needed. To make the approximation more precise, the translational mode was calculated with CATIA V5 which gave a result of $15.06Hz$. This is much higher than the analytical calculation, most likely because the top base of the mounting bracket wasn't included in the hand calculations and it adds stiffness to the system.

Beware that the frequency $15.06Hz$ still doesn't match exactly the fans' speed range. This frequency corresponds to $906.3RPM$. While both fans do cross that frequency, they do it very quickly to then settle at their rated speed of about $5500RPM$ for the PiFan (at 5V) and $1250RPM$ for the USB fan. However, rocking frequencies haven't been considered yet. Note that while the translational frequency stays the same at every wheel speed, the rocking (rotational) frequencies change with wheel speed, as shown in figure 5.15. These will therefore better approach the harmonic of the wheel speed, as compared to the translational frequencies, and they will be the ones responsible for the resonance behavior of the bracket. They still do not cross entirely the fundamental harmonic (the wheel speed value in Hz), in order not to generate an excessive resonant behavior, but they only approach it. The rocking frequency at speed 0 was computed in CATIA V5 and the ones at other speeds were calculated analytically (equation 5.68).

The transfer function between the wheel and the top base is also called transmissibility in literature [10]. This will be very similar to the transmissibility of a reaction wheel hard-mounted to a dynamometer since the equations of motion will be analogous, but the stiffness and the damping coefficients will of course be very different in this case. This can be derived directly from the equations of motion and is defined by Phuoc [10] as:

$$T(\xi, \Omega, \omega_n(\Omega)) = \left| \frac{F_{out}}{F_{in}} \right| = \sqrt{\frac{1 + 4\xi^2 \left(\frac{\Omega}{\omega_n(\Omega)} \right)^2}{\left(1 - \left(\frac{\Omega}{\omega_n(\Omega)} \right)^2 \right)^2 + 4\xi^2 \left(\frac{\Omega}{\omega_n(\Omega)} \right)^2}} \quad (3.3)$$

Where ξ is the damping ratio of the system, chosen as 0.002, a typical value for metallic materials like the iron bars, Ω is the rotational speed of the wheel in Hz, $\omega_n(\Omega)$ is the eigenfrequency (or natural frequency) of the system (in Hz), which is excited by the wheel speed harmonic (closest to it), and is speed-dependent in case of the rocking (rotational) mode. F_{in} is the source disturbance at the wheel, while F_{out} is the output disturbance measured by the accelerometer, attached below the top base of the mounting bracket. This will be further discussed in the unified model section 5.3 (eq. 5.67).

It is important to bear in mind throughout this report that the soft-suspended approach always implies the measurement of F_{out} , the disturbance at the mounting bracket top base, while in the hard-mounted to ground approach F_{in} is directly measured at the source (on the reaction wheel). The two results can then be compared by dividing F_{out} by the transfer function above.

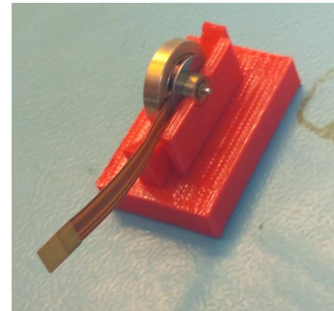
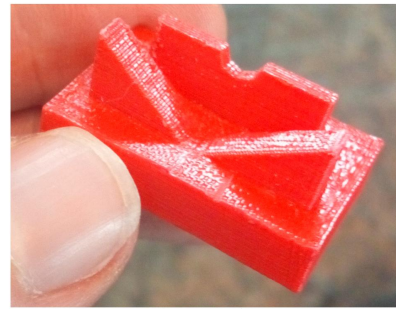
3.3.3. Possible measurement solutions and failed attempts

Before the final setup was designed, as shown in the previous sections, a few attempts to procure a working reaction wheel and to design a suitable mounting bracket were made. These are going to be reported in this section to show the main constraints around this project and some lessons learned.

Initially, similarly to the concept by Sui et al. [20] explained in section 3.1, a mounting bracket for the Delfi-PQ reaction wheel was built. First of all, it was discussed whether the mounting bracket could be produced in metal: iron for the bottom base and the four bars, to give weight to the base and make its resonance frequency higher than the rest of the setup, and elasticity to the bars, and aluminum for the other parts. However, the production cost that was estimated by an external company was considered too high, and it was decided to 3D print the mounting bracket in-house since a preliminary validation of the concept is thought to be possible also on this kind of prototype. In figures 3.9a and 3.9b, pictures of the 3D-printed mounting bracket are shown.



(a) 3D-printed mounting bracket



(b) Details of the mounting bracket top base

As can be noticed, this approach still relied on the transmission of vibrations to the bracket via friction, as in Sui's concept. The purpose was to clamp the BLDC motor on the small rectangular profile on the top base and make the flywheel rub against the triangles in front of it.

Since the PME (Precision and Microsystems Engineering) department at TU Delft also has a Polytec laser vibrometer, this was initially thought to be the reference measurement approach, because its resolution is far superior to the one of a MEMS accelerometer. The plan would have then been to compare microvibrations measured by the accelerometer to the ones measured by the vibrometer, to verify whether low-cost sensors could work with this approach as well. However, in the period in which the experimental part of this thesis took place, the lab containing the laser vibrometer was inaccessible due to COVID-19, and therefore the vibrometer could not be used.

At the same time, the idea of the microvibration measurement on the Delfi-PQ reaction wheel was discarded since all the three remaining BLDC motors were returning errors while trying to control them, probably because Hall Sensors were damaged (as the EPOS Studio software of its controller suggested). This made it impossible to control the wheel properly, as one of the motors had an intermittent motion and the other two didn't start. Buying another one of these motors was the primary option. However, the EC10 Maxon motor was no longer on sale/production at the time. Therefore it was decided to change the object of measurement. To avoid redesigning a reaction wheel from scratch, the idea was to buy a rotating object that resembles a reaction wheel, such as a small PC cooling fan run by a BLDC motor, which is considered sufficient as a means of validation for the mounting bracket prototype. The following section will explain more in detail why fans make a suitable measurement object in this case.

Further problems emerged later. The main idea for the mounting bracket validation became to compare microvibration results from a low-cost sensor attached to the mounting bracket, with a more standard method of measurement of microvibrations (especially for larger-scale wheels), such as Kistler tables, in a hard-mounted to ground approach. These are 3-axis dynamometers that measure vibration forces and torques in all directions simply by screwing the reaction wheels on top of them. A Type 9256C Kistler Dynamometer was borrowed from a professor of Mechanical Engineering, but, after a few attempts, it was impossible to connect the damaged input cable from the dynamometer to the (5070A) multichannel charge amplified, which is needed to retrieve results. The idea of the Kistler table was thus soon discarded. In any case, the suggested application of the 9256C dynamometer is cutting force measurement, which means that the expected forces are much greater than microvibrations. Also, its noise threshold, which is the minimum disturbance change that the instrument can capture without excessive noise, is higher than required. The 9256C datasheet [35] reports a threshold of $2mN$, which is too high for the desired range, defined by requirement TES-F-003. Therefore, this type of Kistler table is not recommended for hard-mounted microvibration measurement of tiny reaction wheels, even in future work. In principle, it should be possible to still use a Kistler dynamometer and fix it on the top base of a soft-suspended bracket, to enhance its resolution. However, its weight is excessive for the bracket design proposed in this thesis, and a more sophisticated system would then be necessary.

Due to these difficulties, tests were continued with more rudimentary solutions at home, since access to many labs in the university was restricted. This also affected the concept selection, where two other measurement approaches were eventually chosen, as previously mentioned. Possible recommendations from these failed attempts will be given in the final chapter, section 7.3, so that measurements approaches can be given a priority and be determined more easily for a future iteration.

3.3.4. Usage of fans for verification

As previously mentioned, fans have been used instead of actual reaction wheels, exclusively to validate the test bench measurement approach in its prototyping stage. This paragraph shows why fans make a good choice for validating microvibration measurement approaches, due to their similarity with reaction wheels.

First of all, PC fans are run by BLDC (Brushless Direct Current) motors, which are generally the first choice for small-size reaction wheels as well. BLDC motors are a source of vibrations, that will thus be comparable to the ones generated by reaction wheel motors of similar size. Second, PC fans, like reaction wheels, have a certain degree of imbalance, due to a geometrical eccentricity given by an uneven mass distribution or the wear of fan blades [36]. This imbalance is likely greater in PC fans than in reaction wheels, due to the greater geometrical complexity (and hence a less uniform mass distribution) and the likelihood of wear or accumulation of dust on the fan blades. Therefore, the amount of imbalance measured during tests is expected to be slightly larger than that of similar-size reaction wheels. This makes the fans suitable for the validation of a test bench prototype, at least to validate the approach, while possible future iterations on this test bench could

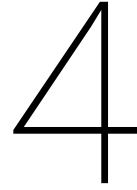
validate measurements on actual reaction wheels so that requirements can be made stricter at each step.

A qualitative estimation of the disturbance torque generated by a PC cooling fan can be done by scaling measured amplitudes in literature. Carrara and Kuga [37] measured the torque produced by a CPU fan, weighing about 500g, which resulted in 0.46mNm . It is reasonable to scale microvibrations according to a linear proportion of the weight of the rotating object, as was done for example to estimate disturbances for the Delfi-PQ RW [2], because imbalances and radii increase with weight, while angular speeds generally slightly decrease. Therefore, since the Pi-Fan weighs about 22g and the USB fan around 100g, disturbance torques of 0.02mNm and 0.1mNm are expected respectively. These values, and in the worst-case scenario also the one by Carrara and Kuga, fall into the range expected for Delfi-PQ and indicated in requirement TES-F-003, and therefore represent perfectly acceptable amplitudes for the validation of the test approach.

Last but not least, PC fans were chosen also because of their low cost, which was in line with the cost of the test bench and with the research objective, and their ease of use (plug-and-play). The choice, for example, could have fallen also on hard disk drives [38], which have recently been used as Cubesat reaction wheels. These could also be chosen for an intermediate future iteration, due to the lack of blades and an even greater similarity with reaction wheels, before testing on actual reaction wheels.

A possible downside of fans is the influence of airflow dynamics on microvibrations. Since the major disturbance source is still the fan imbalance, this is expected to be visible in the results, but the airflow could result in noisier data as compared to reaction wheels. Furthermore, fans also produce an additional harmonic in their vibration spectrum, called Blade Pass Frequency (BPF), which is equal to n times its angular speed, where n is the number of blades of the fan [36]. A fan with 7 blades, for example, will show the usual fundamental harmonic 1 in order domain (the one corresponding to its rotational speed), and harmonic 7 as well. However, this is not considered a problem as it will not influence the fundamental harmonic, so imbalances can be calculated as usual.

Keep in mind, in any case, that the main goal remains to measure low-amplitude microvibrations with low-cost equipment, regardless of the object that generates them.



Microvibration tests

In this chapter, the experimental part of the project will be described. This includes a test plan; an explanation of the working principle of the sensors, Arduino circuit, and sketches; the test data processing in MATLAB; and the final test results in terms of time-amplitude plots and waterfall plots (frequency-RPM-amplitude plots).

4.1. Test plan

To validate the 3D printed mounting bracket and the whole setup for microvibration testing, the plan is to compare one laser test and two types of accelerometer tests (one on the mounting bracket and one with the fan on the ground and accelerometer mounted on the fan) with a MATLAB simulation, consisting of empirical and analytical models, joined together in the unified model. The PiFan is also able to run at two different speeds, depending on its voltage (3.3V or 5V), so that results at different speeds can be compared. Unfortunately, the acceleration of both fans after turning on is quite fast and makes it difficult in this case to compare results at speeds other than the fans' nominal speeds. The speed range in the test results will thus appear quite narrow.

Therefore, for a complete validation process, it is suggested in the future to run a BLDC motor, for example, with a torque or speed control loop that allows a constant acceleration from 0 to maximum RPM, then run it in steady-state, and then set the torque to 0 and wait until it comes to rest again (usually referred to as coast-down mode). Otherwise, if the motor can rotate in both directions, as a reaction wheel should, it is suggested to make a few cycles (clockwise - counterclockwise): 0 to max RPM, then breaking until 0; allow a zero RPM crossover (which is often problematic in BLDC motor control) and a change of direction; run it until max speed in the opposite direction. This could be run in different settings, such as full torque or linear (constant acceleration), and would also serve as a possible verification of the reaction wheel microvibration signature requirements, besides the verification of the test setup itself.

In this case, as mentioned, tests for three types of fan settings were made: PiFan at 3.3V, PiFan at 5V, and USB fan. This is to have some redundancy on the object of measurement as well, in case one of the fans doesn't work properly. There are also three different types of test, namely: ground-fixed fans, fans on the mounting bracket, and laser displacement. The reason for the choice of these test concepts has been discussed in the concept selection section (2.1), and it corresponds exactly to the selected combinations of the test bench and measurement approaches. To summarize, the ground-fixed approach and soft-suspended mounting bracket approach have been selected, so that by dividing the test results of the second test by the transmissibility of the mounting bracket, disturbances at the source are estimated. These can be then compared to the test results of the ground-fixed case, where vibrations are measured directly at the source (MPU6050 taped to the fan). The laser approach has also been selected as a further term of comparison for the soft-suspended approach, to validate the results from the accelerometer. For the first two test types, the output vibration values are measured by the MPU6050, as explained in the next sections, while for the laser tests a video of the reflected laser dot is recorded, and later processed. The working principle of the Arduino sketch and a more detailed explanation of the measured data are given in section 4.2, while the post-processing in section 4.3. The table below summarizes the 9 tests that were planned, together with the corresponding output log file names, containing raw acceleration and angular velocity data.

Fan Name, Voltage Test description	PiFan 3.3V	PiFan 5V	USBfan
Accelerometer – Ground-fixed	PiFan-3dot3V-Acc-ground.log	PiFan-5V-Acc-ground.log	USBfan-Acc-ground.log
Accelerometer – Mounting bracket	PiFan-3dot3V-Acc3.log	PiFan-5V-Acc.log	USBfan-Acc.log
Laser displacement	PiFan-3dot3V-laser.log	PiFan-5V-laser.log	USBfan-laser.log

Table 4.1: Test plan

These log files are collected in the raw_test_data folder. It can be noticed that in this folder there are three different sets of log files for the PiFan at 3.3V on the mounting bracket, coming from three different tests. This is caused by the fact that the tests were repeated, since the fan sometimes struggled to start by itself at this voltage, and needed to be slightly pushed by hand, which arguably invalidated part of the results. This happened for the log files 'PiFan-3dot3V-Acc1.log' and 'PiFan-3dot3V-Acc2.log', while for 'PiFan-3dot3V-Acc3.log' the fan started correctly by itself. Therefore, this is the file that was processed and will be used in the rest of the discussion, and that is why it's the only one reported in table 4.1.

4.2. Arduino control

In this section, the Arduino connections and sketch are going to be described. An Arduino Uno was used to power and control four devices: an MPU6050, a US1881 Hall sensor, a KY-008 laser module, and the PiFan (in case of PiFan tests).

The MPU6050 is a module with embedded 3-axis MEMS gyroscope and 3-axis MEMS accelerometer. Therefore, the gyroscope outputs three angular velocities ($\omega_x, \omega_y, \omega_z$), and the accelerometer outputs three accelerations (a_x, a_y, a_z), that can later be processed as explained in the next section. It has a sampling rate of $1kHz$. That means the bandwidth, according to the Nyquist-Shannon sampling theorem, should be $500Hz$ or less, to avoid aliasing. By default, the module has a digital low pass filter at $260Hz$, which can be adjusted in the Arduino sketch. Therefore, it is not suitable for measuring microvibration disturbances in the upper-frequency range ($500 - 1000Hz$). It is powered with 3.3V and it logs data to Arduino via the I2C bus, which corresponds to the Arduino Uno pins A4 and A5 and the MPU6050 pins SDA (Serial Data) and SCL (Serial Clock). Optionally, the INT pin of the MPU6050 can be connected to Arduino's interrupt 2, to indicate that data is available for the sensor to read (otherwise, it enters a low-power mode).

The US1881 is a latching Hall sensor, also commonly called Hall-effect latch or simply latch. The working principle of a latch is the following: the sensor outputs HIGH (or 1) whenever the north pole of a magnet is brought close to it, and LOW (or 0) whenever the south pole of a magnet is brought close to it. That is why at least two magnets were needed on each fan so that the sensor can change state and go back to its original state (one pulse) at least once per revolution. On the other hand, non-latching hall sensors go back to their original (LOW) state on their own, right after the north pole of a magnet is removed, therefore they would need only one magnet on the fan to work correctly. However, a latching sensor was preferred to make the change of states more precise and fast enough to allow a correct reading of pulses. This was powered with 5V.

The laser module is also powered with 5V and the laser wavelength is $650nm$. It was realized only after tests that the CO2 laser mirror is used for the wrong application here. This is commonly used in high-power applications like laser cutting and has a reflectance of 98% at $10.6\mu m$, which is very distant from the laser wavelength. However, the laser reflection captured by the videos was satisfactory enough, and although there is no wavelength-reflectance graph for this mirror, its reflectance at $650nm$ is estimated to be between 40% and 60%, by comparison with other similar mirrors on the market. Therefore, the reflected laser dot is just slightly blurry in this case, but good enough to calculate a displacement, as seen in section 5.4.

The PiFan can be powered either with 3.3V or 5V – as explained in the test plan – so that two sets of data for each type of voltage will be produced.

A circuit diagram of the Arduino wiring on a breadboard, as used for the tests, is shown below.

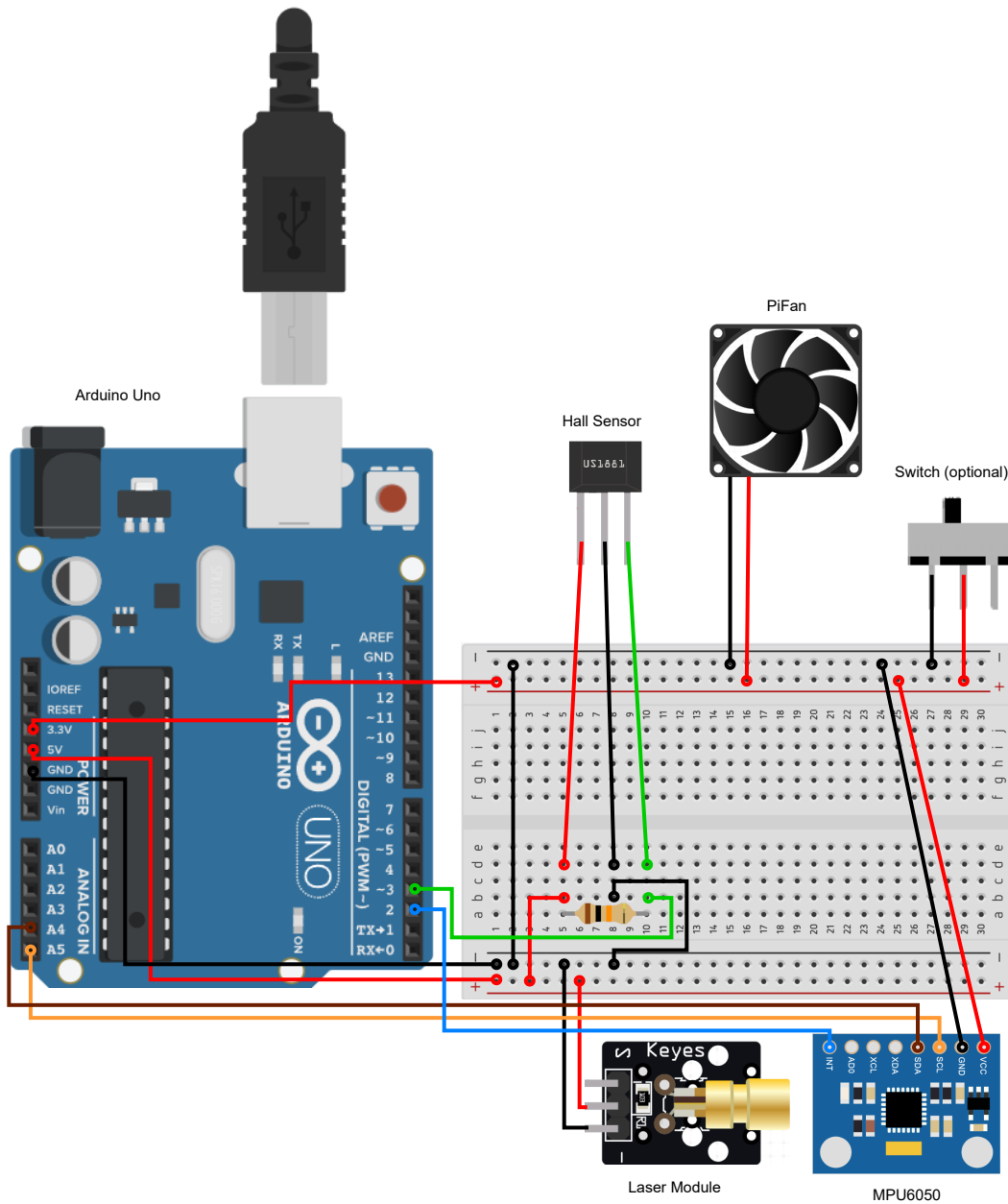


Figure 4.1: Arduino circuit diagram, as used in the tests (PiFan powered with 3.3V)

The sketch used to run all devices is called `RPM_accelerometer.ino` and it's mainly a combination of data reading from the MPU6050 and the Hall sensor, as the name suggests, while the laser module is not connected to any interrupt in this case, and it's always powered.

The `Adafruit_MPU6050.h` open-source library was used to plot data from the MPU6050 onto the Serial Monitor and can be found on GitHub [39]. In particular, a copy of its `basic_readings.ino` sketch in its examples folder was included in the `RPM_accelerometer.ino` sketch. This allows to first set a range for the accelerometer and the gyroscope (respectively between $\pm 2g$ and $\pm 16g$, and between $\pm 250deg/s$ and $\pm 2000deg/s$). Then, a digital low-pass filter bandwidth can be set, between $5Hz$ and $260Hz$, the default value. In this case, the following values were chosen: $\pm 16g$ accelerometer range, $\pm 250deg/s$ gyroscope range (since rotations are limited), and $21Hz$. The value of $21Hz$ was chosen since it was calculated that the mounting bracket's resonance was going to be around $20Hz$. Therefore, since the purpose of the bracket is to amplify vibrations, only vibrations around the resonance are going to be considered, and later divided by transmissibility to obtain the source disturbances, as will be explained in the unified model 5.70. However, it was

realized only later that this was a mistake, as it greatly limits the amount of data that could be read above that bandwidth, even though disturbances would not be amplified so much. In any case, due to the fact that the final raw data were retrieved with this bandwidth, only disturbances at frequencies lower than 21 Hz can be reliably accepted. After these values are set, the three values of raw acceleration in m/s^2 and the three values of raw angular velocities in rad/s are printed to the Serial Monitor, which is set at the highest Baud Rate: 115200 Hz . These data will be processed in MATLAB, as explained in the next section.

Besides this, the `RPM_accelerometer.ino` contains a sketch to program the Hall sensor to work as a tachometer, to measure the speed of the fans in RPM. This was also taken from an open-source project [40], with minor adjustments for this purpose. This sketch measures the period between pulses (1 per revolution in this case), using the `micros()` function to calculate the RPM. The RPM values are plotted to the serial monitor. At high speeds, the period between pulses becomes too low for readings of just 1 pulse/rev to be accurate. Therefore, multiple readings are done and the period is averaged, by dividing the period between the first and last pulse by the number of pulses read. Together with RPM values the following values are returned to the serial monitor: the period between pulses, amount of readings, frequency, and tachometer (a smoothed RPM value that takes into account the multiple readings and averages the RPM). The figure below is an example of the data printed on the serial monitor, which were then copy-pasted to log files for further processing.

```
Period: 172248 Readings: 1 Frequency: 5 RPM: 346 Tachometer: 346
Acc_x: 0.38 Acc_y: -0.92 Acc_z: -10.48 Gyro_x: -0.05
Gyro_y: -0.05 Gyro_z: -0.18
Period: 172248 Readings: 1 Frequency: 5 RPM: 346 Tachometer: 346
Acc_x: 0.94 Acc_y: -0.43 Acc_z: -10.47 Gyro_x: -0.07
Gyro_y: 0.00 Gyro_z: -0.00
Period: 172884 Readings: 1 Frequency: 5 RPM: 348 Tachometer: 347
Acc_x: 1.40 Acc_y: -0.07 Acc_z: -10.50 Gyro_x: -0.06
Gyro_y: -0.01 Gyro_z: 0.06
Period: 172884 Readings: 1 Frequency: 5 RPM: 348 Tachometer: 348
Acc_x: 1.36 Acc_y: -0.75 Acc_z: -10.42 Gyro_x: -0.04
```

Figure 4.2: Example of serial monitor output of the `RPM_accelerometer.ino` sketch (USBfan-Acc.log)

However, it was noticed that the RPM values reported on the serial monitor are likely not truthful, as the PiFan should have a rated speed of about 6000 RPM when powered with 5 V . Instead, the printed speeds were lower by a factor of 3.7. Therefore, it was decided to multiply all RPM values by this factor to match the datasheet speeds.

In the future, it is suggested to improve the tachometer readings. The wrong readings may be caused by the fact that the I2C communication of the MPU6050 was inserted before the loop of the hall sensor interrupt routine, and handling too much data may have slowed down the Arduino Uno logging rate or caused the Hall sensor to miss some pulses. For this reason, probably it would be a better idea to use an Arduino Mega for this purpose since it has two sets of I2C pins. This way, both the hall sensor and MPU could log data via I2C, without mixing interrupts and I2C. As a matter of fact, for the laser tests, where the accelerometer was moved only at the beginning of the tests, the hall sensor recorded higher RPMs.

Otherwise, more magnets could be added on the fans, so that more pulses per revolution would be read, thus making the measurement more reliable.

Another reason for the low RPM could be that the magnets stayed outside of the Hall Sensor proximity zone during some rotations, and therefore a lower amount of pulses was detected. So, the hall sensor cables could be fixed to the top base of the mounting bracket in the future, to allow the sensor to always stay on top of the magnets while moving together with them. This wasn't chosen as a solution for these tests to avoid invalidating the test results, by adding unwanted disturbance (from the cables) to the mounting bracket, which would be difficult to model. Therefore, an even better solution could be to modify the mounting bracket top by adding a 3D printed support just for the hall sensor, to let it stay on top of the magnets so that the cables don't have to be fixed to the bracket.

4.3. Test data processing

The post-processing of the test data is done in MATLAB before they can be compared to models described in chapter 5. This is done in the `test_data_processing.m` script, which performs the following tasks:

- Read raw data from log files
- Select data corresponding only to the range of positive values of RPM (while the fan is rotating)
- Remove the initial offset in the acceleration measurement (before the fan moved, i.e. while RPM is still null)
- Remove any trends to prevent them from degrading the quality of the frequency estimation
- Convert accelerations to forces and angular velocities to torques
- Plot time vs. force or torque
- Create frequency-RPM maps of the forces/torque, containing RMS amplitude estimates of their spectral content at each value of RPM
- Create waterfall plots out of the maps

First of all, the script allows the user to select which log file (generated by the Arduino script during testing) should be read and processed.

MATLAB then imports the data from the log file, including Period, Number of Readings, Frequency, Tachometer (although all of these listed so far are not used), RPM, Accelerations in 3 directions (a_x, a_y, a_z), Angular speeds in 3 directions ($\omega_x, \omega_y, \omega_z$).

The total test time (during which Arduino was logging data) is calculated indirectly, through the number of bytes of the generated files, using the following equation:

$$t_{TOT} = \#bytes \frac{\#bits/char}{\#bits/sec} \quad (4.1)$$

Where $\#bytes$ is the number of bytes of the log file (i.e. the number of characters, since 1 character occupies 1 byte and the log files are entirely composed of characters), $\#bits/char$ is the number of bits occupied by a single character, that is 10 (8 character data bits plus start and stop bit for Arduino), and $\#bits/sec$ is the number of bits per second, which, in this case, coincides with the baud rate used in the Arduino Serial Monitor, that is 115200 Hz.

The time array t is then calculated at intervals corresponding to the RPM data, until the previously calculated t_{TOT} . The sampling frequency is simply calculated as the inverse of the time interval Δt :

$$F_s = \frac{1}{\Delta t} \quad (4.2)$$

After that, the non-zero values of RPM are found, so that only data corresponding to the fan movement (during a test) are processed. All the acceleration and angular velocity values at these indices, where the RPM is null, are thus trimmed. Then, the mean of all acceleration and angular velocity values before the first non-zero RPM value is calculated, and subtracted from the rest of the data, so that there is no offset coming from the sensor bias in the processed data.

Also, for further smoothing of the data, the in-built MATLAB function `detrend` is used, to remove any possible trends, i.e. shifts in data values, which may be caused for example by sensor drift. An imperceptible movement of the sensor may have happened, changing its rest position, especially because it was fixed with tape (ideally but not practically a rigid connection), so this is made up for by this detrending function. More commonly, drift errors happen in IMU's (Inertial Measurement Units) like the MPU6050 or accelerometers and gyroscopes in general because the error generated by integrating accelerations and angular velocities grows over time. This is partially corrected by the low-pass filter integrated into the module, but since small trends were still visible in the raw data they were further removed with `detrend`.

It happened on rare occasions that there were some "false" RPM zeroes, inside the already selected non-zero arrays, while the fans were moving. That is most likely caused by the fact that the Arduino loop couldn't run fast enough to record the tachometer values correctly, as already mentioned in section 4.2, and therefore

logged some zeros in-between the recorded values. Otherwise, the fans may have temporarily moved one or both magnets outside the hall sensor range during vibration, and, as a consequence, the sensor didn't read that value correctly and logged zero. These are removed, as well as all other parameters' values at the same indices, and the remaining array is kept.

The RPM is then multiplied by the 3.7 factor mentioned earlier in section 4.2.

The script now converts accelerations and angular velocities to forces and torques. This is done by multiplying the accelerations by the mass of top base and fan, and by calculating the time-derivatives of angular velocities, times the respective moments of inertia:

$$\begin{aligned} F_x &= Ma_x & T_\theta &= I_{xx} \frac{d\omega_x}{dt} \\ F_y &= Ma_y & T_\phi &= I_{yy} \frac{d\omega_y}{dt} \\ F_z &= Ma_z \end{aligned}$$

Where T_θ is the torque around x and T_ϕ the torque around y . The derivatives are calculated by dividing the difference between adjacent values of disturbance by the time increment of the time array. Masses and moments of inertia are taken from the CATIA model, as explained in section 5.3 and 5.3.2 in particular. The torque around z was not calculated, because it's not representative of the fan motor torque, given that the rotation Ω around z is the fan speed, and it's almost constant. The force F_z is also not shown here in the results, since it will not be calculated later in the models. As a matter of fact, the movement in the z direction of the top base is limited by the iron bars, so the bracket cannot be used as a representative measurement system in the z direction.

The script now generates a series of plots. First, these disturbances are plotted in time. Then, they're converted into frequency domain with the in-built MATLAB function `rpmfreqmap`. This function takes as input the disturbance array in the time domain, the sampling frequency of the test and the RPM array, and outputs a map of the analogous disturbance in the frequency domain (with each row corresponding to a single frequency and each column corresponding to a single speed), a frequency array and a speed array. The function uses a Short-Time Fourier Transform (STFT) to do this, which means it divides the signal into small segments (or windows), averages the speeds (RPM values) inside each window, and returns the corresponding Fourier transform. By default, `rpmfreqmap` returns the RMS (Root Mean Square) amplitude estimates of the disturbances at each value of RPM, meaning that, inside each window, the RMS of the disturbance is returned (by averaging the squares of the disturbance values and then taking the square root). Further options, that will be used later in the empirical model are '`peak`' and '`power`', which respectively return the peak amplitudes and the power spectrum. This will be further explained in section 5.1.

The frequency and RPM arrays returned by the STFT can now be mapped onto a mesh for 3D plotting, with the `meshgrid` in-built MATLAB function. The waterfall plots can now be generated, with the `waterfall` MATLAB function, which takes these two meshes of frequency and RPM– and the disturbance spectrum previously calculated by `rpmfreqmap` – and directly returns the plot.

The script, by user request, can also generate time and/or waterfall plots of accelerations and/or angular speeds. Since these will not be analyzed further or compared to the models, they will not be shown here.

Test results are shown in the subsections below, followed by a discussion. For simplicity, only the USBfan case will be shown here, both for ground-fixed and mounting bracket tests, and the other two cases (PiFan at 3.3V and PiFan at 5V) will be shown in appendix A. This will be enough to understand the quality of the retrieved results for the two approaches – which is similar for both fans – and to see what processed data look like and how they will be compared to models later on.

4.3.1. Interpretation of waterfall plots

This subsection describes how waterfall plots should be interpreted.

As previously mentioned, waterfall plots are 3D plots, with frequency [Hz] or harmonic order [-] in the x axis, the wheel rotational speed [RPM or rps] in the y axis, and amplitude [N or Nm] in the z axis. The previous paragraph explained how these plots are built through a Short-Time Fourier Transform that converts the signal from the time domain to the frequency or order domain. In figure 4.3 it is shown in practice what it's meant by that and why the treatment of vibration data in these domains is convenient.

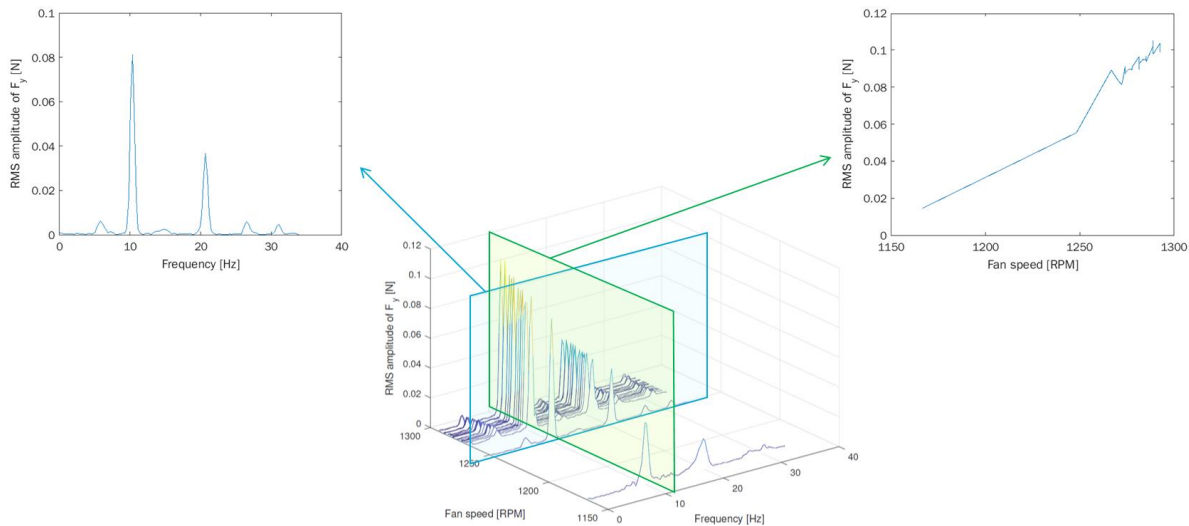


Figure 4.3: Interpretation of waterfall plots

As shown above, the STFT groups together similar fan speeds in the same window, and then averages these speeds inside the window and generates a frequency-domain signal only at that averaged speed. This corresponds for example to the blue plane in the waterfall plot in figure 4.3, which is extracted in the top left and can be interpreted as a frequency-amplitude plot at speed 1250RPM. This is valid for all parallel slices of the waterfall plots. These slices are stacked together by the STFT algorithm to form the waterfall plot. Of course, a slice of the 3D plot perpendicular to this will correspond to a speed-amplitude plot at a certain constant frequency, as illustrated in the figure in the top right. To better understand the convenience of this representation, it would be useful to look at equations 5.1 and 5.2, which are the base of microvibration models. According to these equations, the signal amplitude should grow quadratically with speed. That is in fact what can be seen on the green plane, although with some variance compared to the ideal model. At the same time, equation 5.1 implies that a certain harmonic k (one of the sine functions that are summed to compose the entire signal) should be visible in the $x - y$ plane along the straight line $\bar{\omega}_k = h_k \Omega$, where $\bar{\omega}_k$ is the frequency of the harmonic, h_k is defined as harmonic order (and is the dimensionless coefficient of this line), and Ω is the fan speed. This corresponds to the ridges which can be seen on the $x - y$ plane of the waterfall plot and follow a straight line, although the coefficient is not clearly visible because the speed range is very narrow. Alternatively, the order domain is also commonly used in microvibration treatment. In this case, disturbance ridges follow a vertical line, where a single harmonic should be visible for all speeds at a constant harmonic order (or number). This is generally helpful for distinguishing harmonics and their causes since disturbances from different sources correspond to different harmonic numbers. Disturbances generated by imbalances, for example, have harmonic order 1 (also known as the fundamental harmonic), while ball bearing disturbances have higher harmonic numbers which can be determined analytically as in table 1.1.

Since waterfall plots provide all these pieces of information in a single plot, they are widely used in this field.

4.3.2. MPU6050 test results (USBfan hard-mounted to ground)

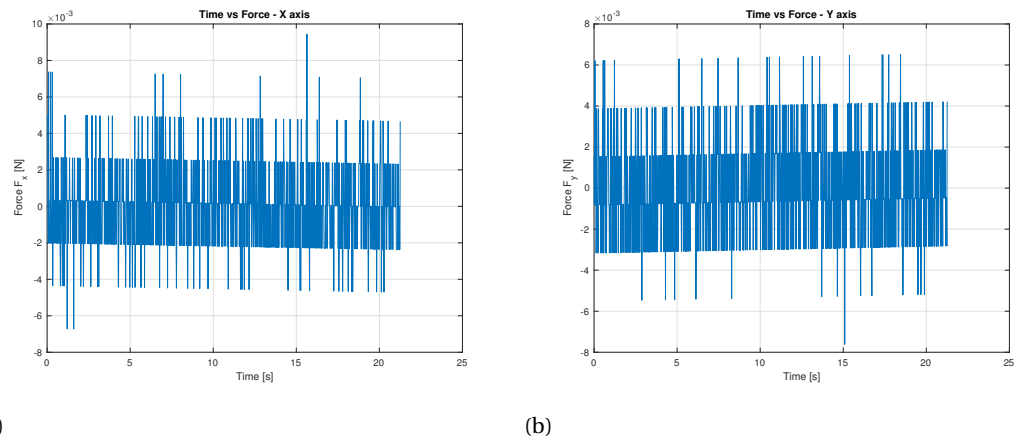


Figure 4.4: Test results: Force-time plots of the ground-fixed USBfan

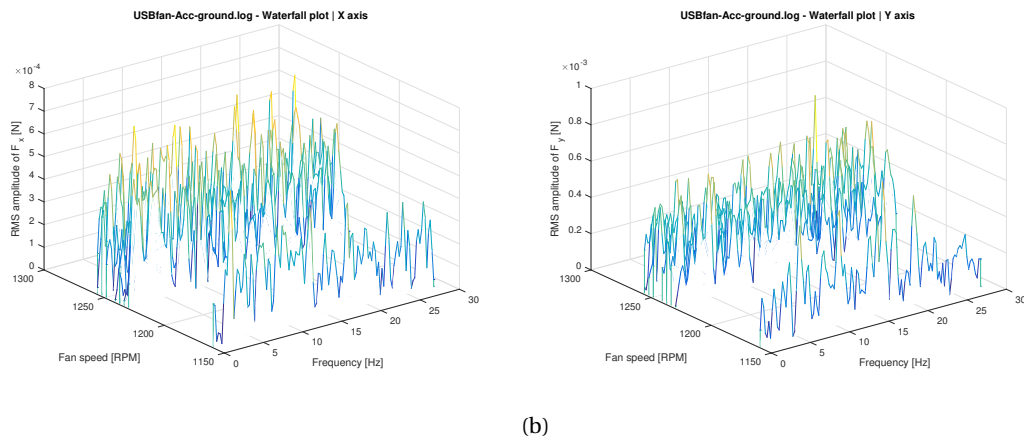


Figure 4.5: Test results: Waterfall Force plots of the ground-fixed USBfan

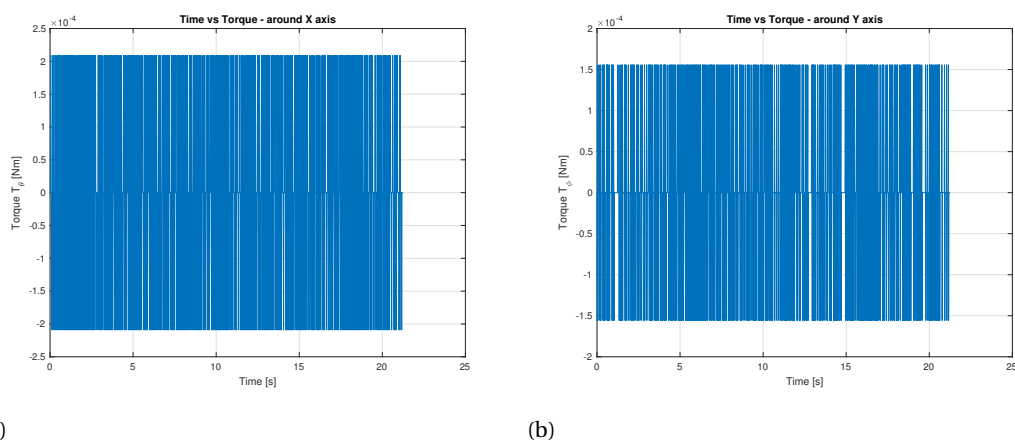


Figure 4.6: Test results: Torque-time plots of the ground-fixed USBfan

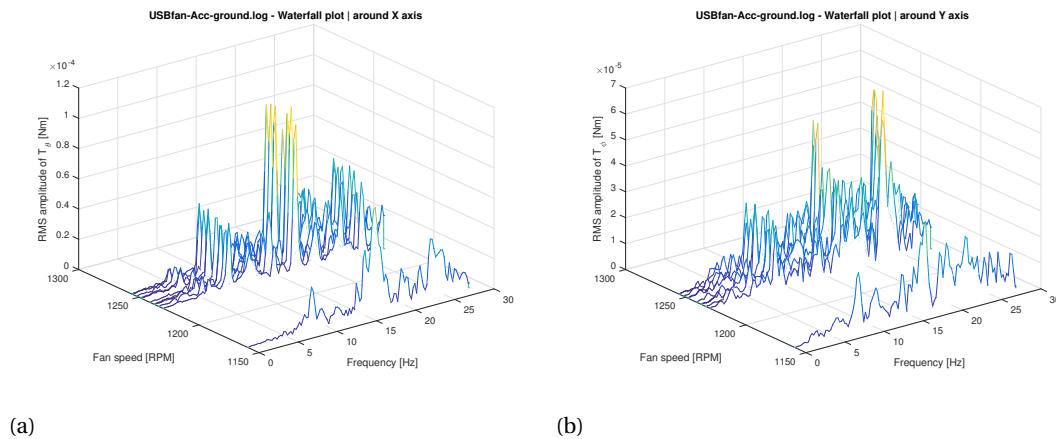


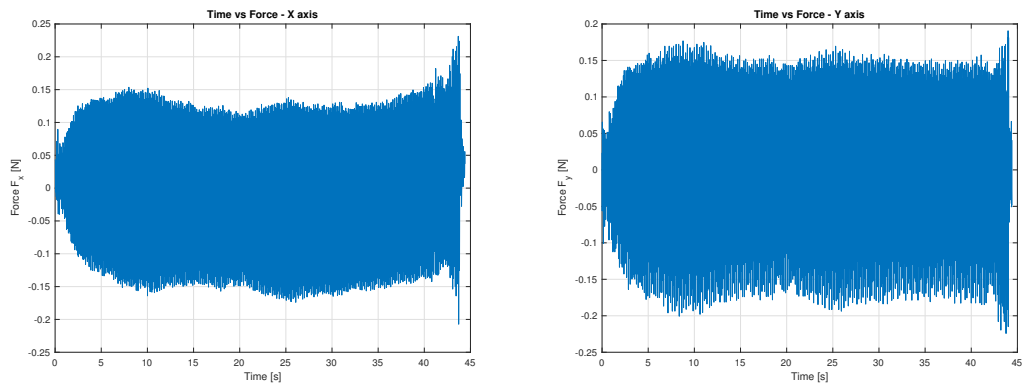
Figure 4.7: Test results: Waterfall Torque plots of the ground-fixed USBfan

It can be seen in figures 4.4 to 4.7 that the test data of the ground-fixed fans are extremely noisy. Noise is caused by the accelerometer and can be either electrical noise from the circuitry or mechanical noise from the sensor module and cables themselves. This is clear from the waterfall plots especially. Vibrations waterfall plots generally provide much more insight compared to time-amplitude plots. The former aim to show all harmonics (vibration peaks) at specific frequencies and speeds, while in the latter harmonics are not distinguishable and these plots are therefore only useful to visualize possible trends in time, caused for example by sensor drift.

Waterfall plots here show there are no peaks much greater than others, especially in figure 4.5. The only visible peaks are in figure 4.7, for the torque values (measured by the gyroscope), at around 10, 15, and 25 Hz, but it is still not clear if other data are noise or vibrations. In other words, a noise floor is not visible, but the accelerometer noise reached at least the same level of microvibrations, if not higher. As a matter of fact, due to the very limited bandwidth of the accelerometer (260 Hz, limited to 21 Hz), high-frequency disturbances are completely indistinguishable from noise in this case scenario, and therefore none of the ground tests will be useful for further modeling or validation. Therefore, it can be deduced already that the cheap accelerometer MPU6050 is not suitable for the ground-fixed approach. Thus comparisons will be done only between tests performed with the soft-suspended approach and models.

As predicted during concept selection, there was some doubt whether the ground-fixed approach could work in this case, especially because the noise threshold of the accelerometer is around 0.2 N, while microvibrations are expected to be around 2 mN and below (TES-F-003). It was decided to try this approach anyways, to see whether real peaks were higher than expected or the noise threshold of the sensor lower, but the results confirmed the negative expectations (noisy data). The noise level in force measurement in fact seems to be stable at around 5 mN, as seen in figure 4.4, and at around 0.21 mNm for torques (figure 4.7). The gyroscope in this case performed a bit better than the accelerometer in the same module since the torque noise level falls right into the range of TES-F-004, and that is why some peaks are visible. However, it is still not sufficient, since noise should be below that range. It follows that the verification of TES-F-003 and TES-F-004 will be possible only through the soft-suspended approach. Furthermore, to offer a backup solution for the validation of the soft-suspended accelerometer measurements, a second measurement approach (the laser) was selected.

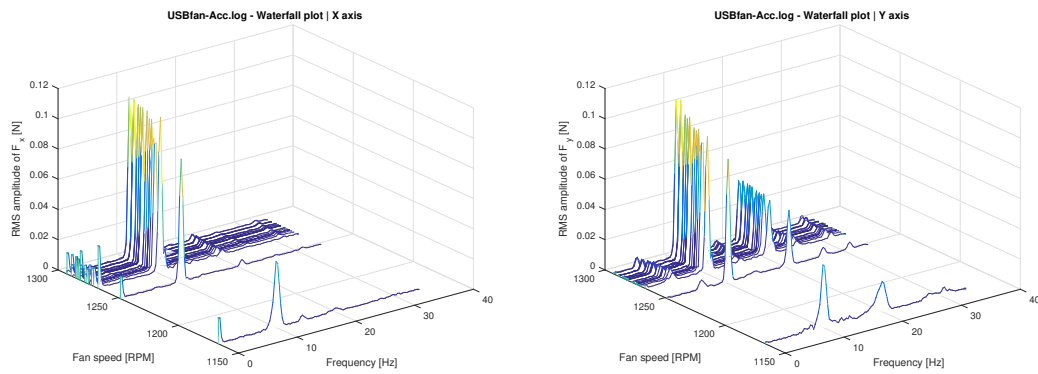
4.3.3. MPU6050 test results (USBfan hard-mounted to mounting bracket)



(a)

(b)

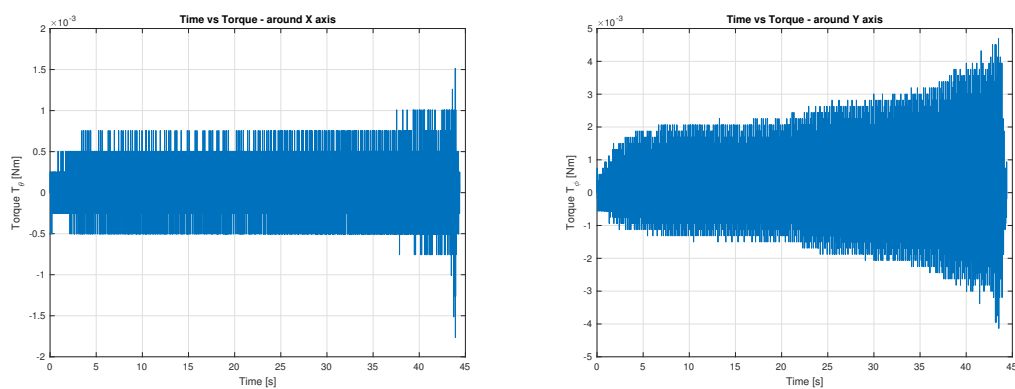
Figure 4.8: Test results: Force-time plots of the USBfan mounting bracket



(a)

(b)

Figure 4.9: Test results: Waterfall Force plots of the USBfan mounting bracket



(a)

(b)

Figure 4.10: Test results: Torque-time plots of the USBfan mounting bracket

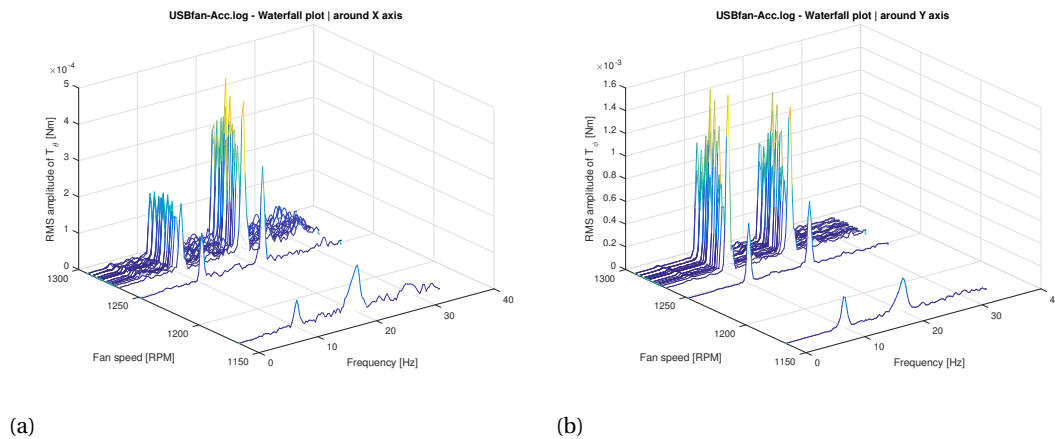


Figure 4.11: Test results: Waterfall Torque plots of the USBfan mounting bracket

In these plots, a disturbance pattern can be clearly recognized in figures 4.9 and 4.11, as opposed to the ground-fixed tests. A small increase in amplitudes can be seen at the end of the time-amplitude plots (4.8, 4.8), but that is not relevant to the discussion, since it is probably simply due to the click on the computer to stop the test, as it was placed on the same table where the mounting bracket was fixed. There are however two clear disturbance ridges at around 10 and 21 Hz, both in force and torque waterfall plots, indicating two harmonics. Since the majority of speeds are between 1250 and 1300 RPM, which corresponds to around 20.5 to 21.5 Hz (dividing by 60), the ridge at 21 Hz is the fundamental harmonic, that is order 1. Similarly, the frequency 10 Hz corresponds to harmonic order 0.5. This is only true because the speed range is very narrow in this case, otherwise, a harmonic order would correspond to a frequency changing linearly across wheel speed, as per its definition ($\omega = h\Omega$).

However, two problems arise in the harmonic order determination. First, as previously mentioned, the speed calculated by the hall sensor was adjusted by multiplying it by a factor of 3.7, to match the PiFan rated speed, after it was understood that the measured speed was incorrect. Therefore, it will be difficult to match frequencies to harmonic orders correctly, since this factor might be inaccurate. Second, it should be recalled that 21 Hz is also the filter bandwidth that was used by the MPU6050 accelerometer. Therefore, it is possible that aliasing happened and higher frequencies were mirrored at 21 Hz. As a consequence, all frequencies reported in this project are unfortunately not representative of the real ones. It will be assumed in the rest of the thesis that these are the real frequencies, and in the final comparison between experimental data and models more attention will be given to amplitudes rather than frequencies, to obtain at least a partial validation, while frequencies cannot be considered reliable.

Furthermore, it can be noticed that torques are still a bit noisy even for the mounting bracket tests, especially in those of the PiFan in appendix A. This is caused by the fact that their amplitudes are much smaller as compared to forces. Angular velocities, coming directly from the gyroscope measurements, show the same noisy pattern. Therefore, their amplitudes will be used for the coming models anyways, although the results are not as reliable as those of forces.

The USB fan mounting bracket test arguably provided the best results out of all tests, since more disturbance ridges can be seen, and also small ones, quite close to noise, in the force waterfall plots (4.9), that may be due to bearing imperfections or torque ripple. These ridges are the harmonics that should be identified later by the empirical model, so these experimental data represent a good basis for the validation of the model.

As regards the measured disturbance ranges, small ridges can be distinguished in 4.9 at about 5 mN. However, to get to the source disturbance, this value should be divided by transmissibility, which in the case of the USB fan is about 200 at 21 Hz (figure 5.16b). So the real minimum disturbance is about 0.025 mN, which is very close to the requirement TES-F-003 (0.0186 mN). Similarly for torques, a disturbance of 0.2 mNm can be seen in figure 4.11(a). This corresponds to a source torque of about 0.001 mNm, which satisfies requirement TES-F-004 (0.0034 mNm).

4.3.4. Laser tests

The `test_data_processing` script handles data differently in the case of laser tests. The calculation of test times is the only part in common with the other types of tests, after which the script starts a different case only for laser tests. The whole data processing explained above doesn't happen in this case, because the accelerometer was disconnected and therefore doesn't provide any useful disturbance data. The only useful accelerometer data, in this case, are given by the shaking of the accelerometer done at the moment the video recordings of the laser started. Therefore, the script, in this case, only determines the time when laser videos started (which coincides with the first accelerometer movement), to match RPM data to corresponding laser displacements. The only goal of the script is therefore to output the correct RPM array and the corresponding time array.

This is done by looking at all disturbances generated by the accelerometer during the shaking (3 accelerations and 3 angular velocities), and determining the minimum time t_0 at which one of these gets out of the band delimited by its mean \pm one standard deviation. The RPM and time arrays are then trimmed, keeping only the part from that time index on. The time t_0 is also subtracted from the previously calculated test time array so that it starts from zero. The rationale behind the determination of the video start time is shown in the figure below:

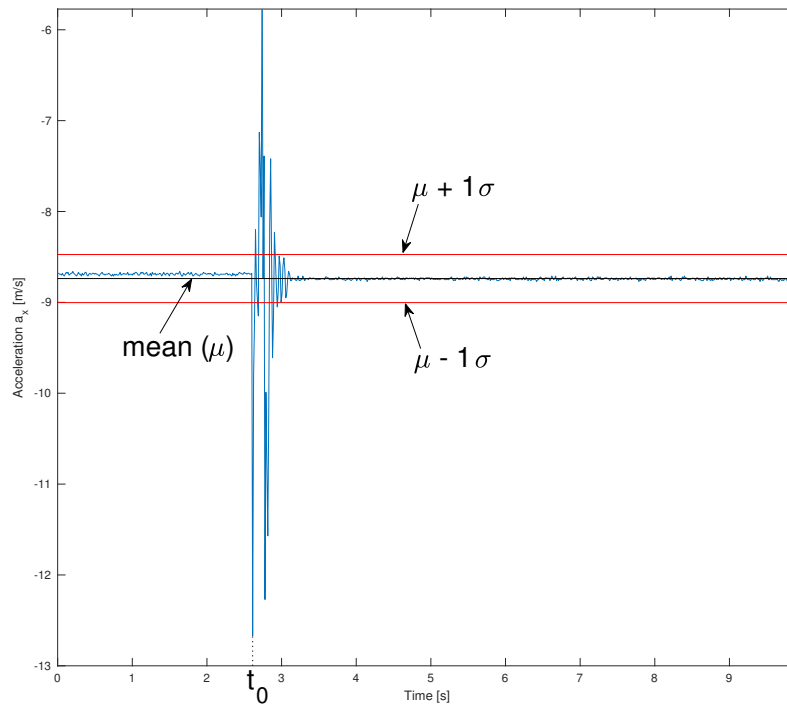


Figure 4.12: Determination of minimum time of accelerometer shaking for laser tests. USBfan a_x data.

The script then just plots the RPM array in time and saves it for the laser displacement model. The real processing of the laser displacement data will happen there, and it is described in detail in section 5.4.

5

Microvibration models

In this chapter, the microvibration models will be described in detail. First, an empirical model is described, which takes the processed test data as input and performs a parameter fitting algorithm to extract two important sets of parameters: harmonic orders and amplitude coefficients. Then, an explanation of the analytical model will follow, including the derivation and solution of the equations of motion of the system. To further refine the solutions, the two models are then joined together into a single, unified model, where the external forces of the equations of motion are the disturbances that had been previously approximated by the empirical model. Finally, a model of the laser displacement, based on an object recognition script of the laser reflection videos, will be explained. The goal of this chapter is to generate results from the models that are directly comparable to the ones of the tests in the previous chapter, to be able to validate them, as will be seen later in the comparison chapter 6.

5.1. Empirical model

The empirical model is a disturbance identification and parameter fitting model, where test data are taken as input and corresponding harmonic orders and amplitude coefficients are determined. These parameters will be fundamental, as explained in section 5.3, to determine static and dynamic imbalances of the fans in the unified model. The first complete empirical approach for microvibration modeling was created to assess the influence of RWA vibrations on the Hubble Space Telescope at NASA, and later presented in detail in literature especially by R. Masterson [27][28]. More recent literature [10] largely followed her approach for the definition of empirical models, and so will this section, with a few differences due to the particularities of the test bench used for this project.

The initial assumption of this model is that disturbances $x(t)$ (forces and torques) are a sum of discrete harmonics (i.e. sine functions) of the wheel speed Ω , and their amplitudes are proportional to the wheel speed squared:

$$x(t) = \sum_{k=1}^n C_k \Omega^2 \sin(2\pi h_k \Omega t + \alpha_k) \quad (5.1)$$

Where n is the number of harmonics and C_k , h_k and α_k are respectively the amplitude coefficient, harmonic order, and phase of the k^{th} harmonic. Harmonic orders are non-dimensional numbers and they are equal to the ratio of the disturbance frequency $\bar{\omega}_k$ of the k^{th} harmonic and the wheel speed Ω (both in Hz):

$$h_k = \frac{\bar{\omega}_k}{\Omega} \quad (5.2)$$

The goal of the entire model is to approximate all C_k and h_k for the test data, while α_k is assumed constant over a $[0, 2\pi]$ interval.

The definition of h_k , therefore, will be of paramount importance throughout the rest of the model, as data are frequently treated in frequency or order domain, where in the order domain the frequencies are normalized with respect to the wheel speed. Therefore, according to equations 5.1 and 5.2, harmonics in waterfall plots (Frequency/Order-RPM-Amplitude 3D plots) are expected to describe ridges whose amplitude

grows quadratically (in z) along straight lines (in the x - y plane), as can be seen in [41], for example, among others. In the order domain, each of these lines will generally correspond to one constant order, while in the frequency domain they will have a coefficient, according to the definition of harmonic order.

Bear in mind that this model is generally valid for steady-state ($\Omega = \text{const}$) conditions only and transient effects due to speed variations are not considered. However, the fans used in this project don't have a broad speed range, with the speed being almost constant at a given input voltage. Furthermore, the transformation of the data to the frequency domain is done with a Short-Time Fourier Transform (STFT), which transforms the signal only after dividing it into small segments, which for this purpose can be considered quasi-steady-state. This will be explained more in detail later. Similarly, an analytical solution of the system will be calculated in the unified model in section 5.3, where the solver finds solutions in small windows where the RPM is averaged (and even almost constant before averaging).

The model consists of four main blocks, which correspond to the following MATLAB functions, included in the `emprical_model.m` toolbox:

- `iden_harm.m`, which identifies the harmonic orders of the input data.

- `find_coeff.m`, which approximates the amplitude coefficients of the given data at the harmonic orders determined in step 1.

- `remove_mode.m`, which removes the effects of wheel structural resonances (which usually deviate from the quadratic model) and recalculates the amplitude coefficients.

- `comp_model.m`, which compares the model to test data.

The general workflow of the model with the force F_x as input is shown in figure 5.1, where `find_peaks.m` and `bin.m` are auxiliary functions of the harmonic identification routine and the `test_data_processing.m` was explained in chapter 4. The model works exactly the same way with other input forces or torques. Only the units of the output amplitude coefficients will differ ($[kg \cdot m]$ for forces and $[kg \cdot m^2]$ for torques).

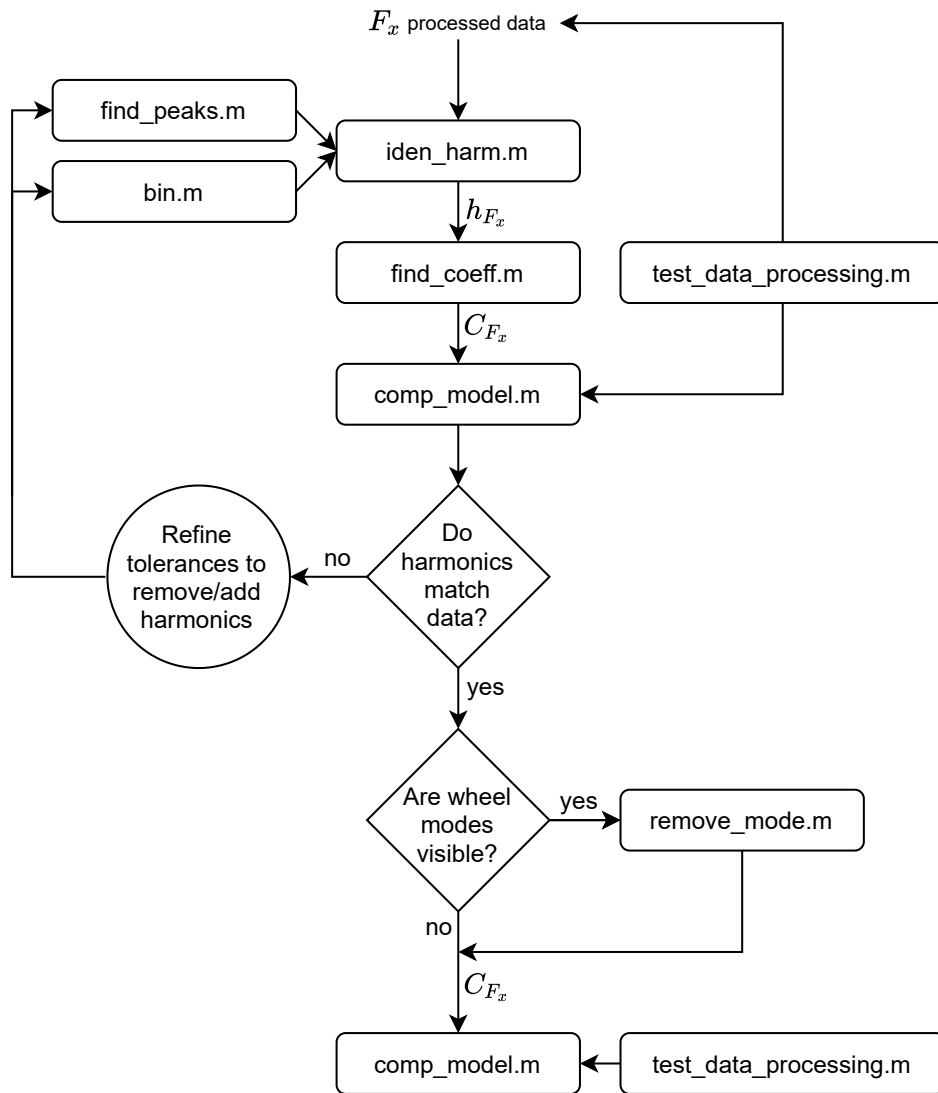


Figure 5.1: High-level workflow of the empirical model - Example with F_x disturbance as input

Notice that often in literature the axial forces F_x and F_y are merged to obtain one single set of parameters h_{rad} and C_{rad} for the radial directions of the wheel. After the calculation of h_{F_x} and C_{F_x} , for example, they would need to be compared to the same parameters in the y direction to further filter down the number of harmonics. However, this is only possible due to the symmetry of reaction wheels in the x - y plane. In this case, the whole test setup should be considered. Given that it's not symmetric, being the y side of the top base longer than the x one, the corresponding disturbances are always treated separately. The same goes for torques.

In the following paragraphs, a more in-depth description of each block will be given. Throughout the explanation, it will be useful to remember that the index i will always be used for speeds, j for frequencies, and k for harmonic orders.

5.1.1. Harmonic numbers identification

The harmonic identification block is shown more in detail in the workflow diagram below:

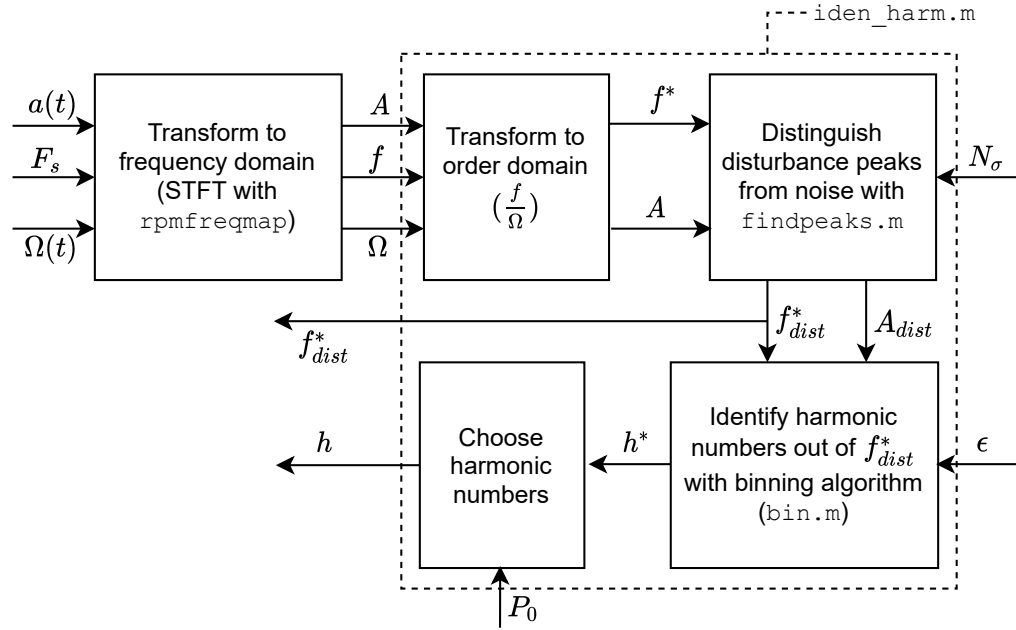


Figure 5.2: Harmonic number identification block

Where the input/output parameters are described in the table below:

Name	Description	Unit
$x(t)$	Amplitude array of force/Torque in time domain	N or Nm
F_s	Sampling frequency	Hz
$\Omega(t)$	Fan speed array in time domain	$rps(Hz)$
A	Amplitude map (matrix) in frequency domain	N or Nm
f	Frequency array	Hz
Ω	Fan speed array mapped in frequency domain	$rps(Hz)$
f^*	Normalized frequency matrix	None
N_σ	Noise isolation tolerance	None
f_{dist}^*	Normalized frequency matrix of selected disturbances	None
A_{dist}	Matrix of selected disturbances	N or Nm

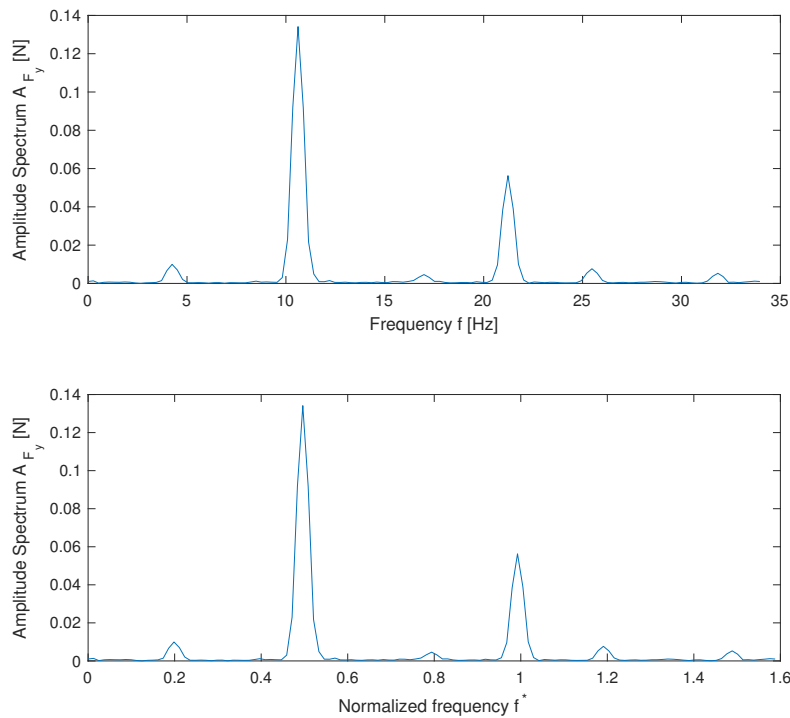
ϵ	Binning tolerance	None
h^*	Harmonic numbers after binning	None
P_0	Bin percentage threshold	None (%)
h	Final harmonic numbers after further filtering	None

Table 5.1: Empirical model parameters (1)

The single diagram blocks of figure 5.2 will be followed in sequence in the explanation below.

First of all, the input signal array $x(t)$ from the experimental results is transformed into frequency domain with the in-built MATLAB function `rpmfreqmap`, as already occurred to plot the test results (chapter 4). This time, however, the peak amplitude is chosen as output, instead of RMS, to get the actual value of disturbances. This function requires the above-mentioned array, the sampling frequency of the test F_s , and the fan speed array of the test $\Omega(t)$, in RPM or rps. The outputs are an amplitude map A in the frequency domain, with each row corresponding to a single frequency and each column corresponding to single speed (but transposed right after), a frequency array f and a speed array Ω , which are the results of the STFT performed by the function on segments of the signal. Therefore, the output Ω array, in the frequency domain, is typically shorter than the input one, since the speeds are averaged for each time window.

The second step is to create a normalized frequency matrix f^* , whose rows are the frequency array divided by each value of Ω . The i^{th} row of f^* , for example, will be f/Ω_i . Beware that frequencies and speeds must have the same units, in this case, i.e. Hz and rps, so if the speed was in RPM before, it must be divided by 60. An example of an amplitude plot in frequency and order domain (normalized frequency) is shown in figures 5.3. These are exactly slices of the waterfall plots (in frequency or order domain) already seen in the test chapter, for a single speed value.

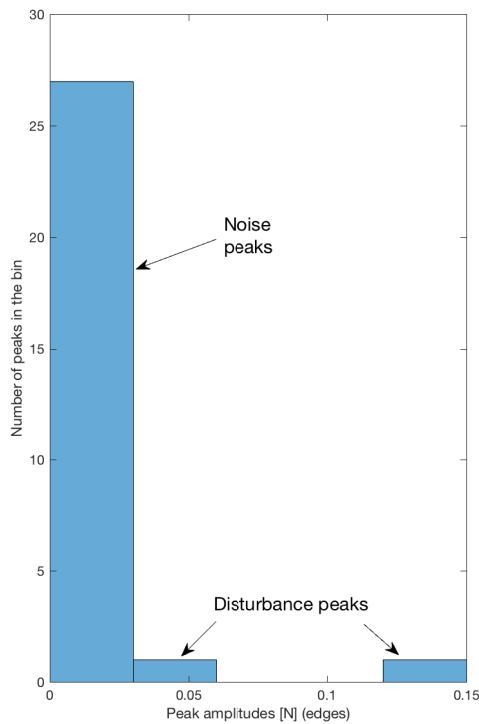
Figure 5.3: Example of amplitude spectrum in frequency and order domain for the USBfan F_y data (@1281.5RPM)

Then, the amplitude A and the matrix f^* are input to the `findpeaks` function. The goal of this function is to distinguish disturbance peaks from noise. The first step of this function is to locate all peaks, including noise. This is done by evaluating the sign of the difference of two adjacent values of amplitude. If at a certain index in the loop the sign is negative and the sign of the previous iteration is positive, it means a peak has been located. Two new matrices are therefore created, A_{peak} and f_{peak}^* , of the same sizes of A and f^* . At the indices where a peak was found these new matrices are equal to A and f^* , and 0 elsewhere. However, not all these peaks correspond to disturbance harmonics.

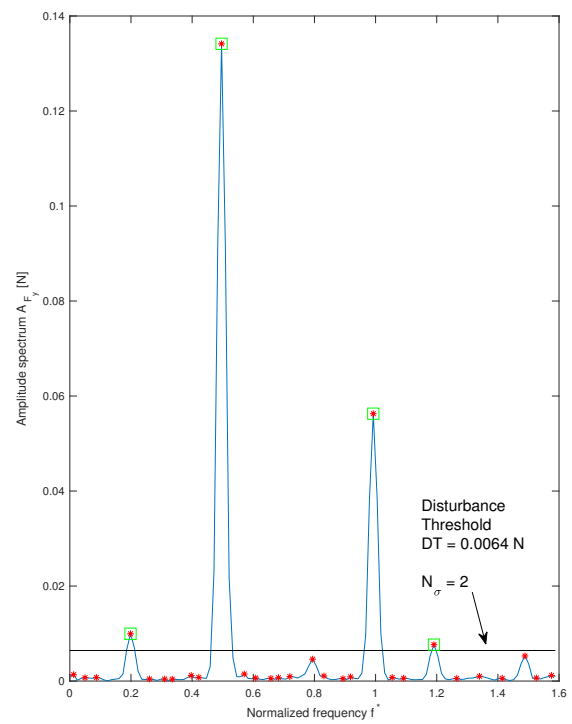
The following step in `findpeaks` is the actual noise analysis, where noise peaks are eliminated. First, amplitude peaks in each row of A_{peak} are grouped in histogram bins with the in-built MATLAB function `histcounts`, which returns the number of elements in each bin and an array of bin edges. An example of this function's output can be seen in figure 5.4a. Noise peaks are assumed to be located in the bin with the greatest number of peaks. Given this assumption, all peaks in A_{peak} with amplitude less than or equal to the one of the noise peak at the rightmost edge of the largest bin (i.e. the largest noise peak) are considered noise. Therefore, a Disturbance Threshold DT can be defined, below which peaks are deleted, so that only disturbance peaks remain:

$$DT = \mu_{noise} + N_{\sigma} \sigma_{noise} \quad (5.3)$$

Where μ_{noise} and σ_{noise} are the mean and standard deviation of the identified noise peaks and N_{σ} is an arbitrary tolerance level defined by the user (usually 2 or 3 is suggested). A greater tolerance will set the threshold higher and eliminate more noise peaks. In this case, the Signal to Noise Ratio (SNR) of the amplitude row (at a certain speed) was taken into account. If the SNR is greater than 20 (according to the in-built MATLAB function `snr`), N_{σ} is set to 3, so more peaks can be deleted, else it is set to 2. An example of noise peaks that have been eliminated under this threshold can be seen in figure 5.4b. The red stars correspond to all peaks contained in A_{peak} , including noise, while the green squares correspond to remaining disturbance peaks only, after the noise has been eliminated.



(a) Noise peaks binned into largest bin



(b) Noise eliminated below DT and remaining disturbance peaks identified

Figure 5.4: Noise identified in histogram bin and eliminated below Disturbance Threshold. USBfan F_y data (@1281.5RPM)

Finally, all amplitudes of A_{peak} above DT and the corresponding frequencies in f_{peak}^* are copied into two new matrices, A_{dist} and f_{dist}^* , which therefore contain only disturbances and are equal to 0 elsewhere.

The results of the noise analysis, however, are not the final harmonic disturbances. For a disturbance to be classified as harmonic, it should occur at the same normalized frequency over all fan speeds. That normalized frequency will then be a harmonic order, as defined in equation 5.2. That is to say that harmonic disturbances in waterfall plots (in order domain) appear as straight ridges at a constant harmonic order (e.g. 1). Therefore, a further binning algorithm is needed to extract the harmonic orders out of f_{dist}^* , and this is implemented by the function `bin`. This works as follows: a new cell array, F_{bin} , of the same length of the normalized frequency array f_{dist}^* , is created. Then, the script iterates through rows of f_{dist}^* setting a row as the baseline, f_{base}^* , for the following search procedure. Another iteration now happens through the elements of f_{base}^* . For the k^{th} element of f_{base}^* , the script is going to verify which non-zero elements of f_{dist}^* , satisfy the following equation:

$$f_{basek}^* - \epsilon \leq f_{distij}^* \leq f_{basek}^* + \epsilon \quad (5.4)$$

Where ϵ is a user-defined tolerance, which equals the maximum difference between two desired harmonic orders (in this case, 0.05).

Whenever an element f_{distij}^* satisfies the condition above, it is copied to the bin F_{bin_k} and it is set to 0 in the f_{dist}^* matrix. If more than one normalized frequency satisfies the condition for a given row i , the average is placed in the bin and both are set to 0 in the matrix, to make sure they're not accounted for more than once. The script continues with the following row of f_{dist}^* as f_{base}^* . At end, all elements are binned into F_{bin} and f_{dist}^* is a matrix of zeros. The outputs of this script are F_{bin} and another cell array F_{stat} , containing the averages and number of elements of each bin of F_{bin} .

Finally, the harmonic numbers can be selected from F_{bin} . A bin percentage threshold, P_0 , can be selected by the user so that only bins containing more than a certain percentage of the maximum possible elements (length of the speed array) will be the ones corresponding to harmonic numbers. That means bins will have to satisfy the following condition:

$$P_k = \frac{N_{bin_k}}{N_\Omega} \cdot 100\% > P_0 \quad (5.5)$$

Where N_{bin_k} is the number of elements in the k^{th} bin, saved in F_{stat} , and N_Ω the number of elements in the speed array. P_0 in this case was chosen as 30%. That means, if a normalized frequency occurs at more than 30% of all speeds, it is considered a harmonic order. The average of the corresponding bin, therefore, which was previously saved in F_{stat} , is saved into a new array of final harmonic orders, h . This is the final output of the `iden_harm.m` script, together with the f_{dist}^* matrix, which will also be used for the amplitude coefficient calculation.

5.1.2. Amplitude coefficient calculation

The amplitude coefficient calculation block, entirely contained in the `find_coeff.m` script, is shown more in detail in the diagram below:

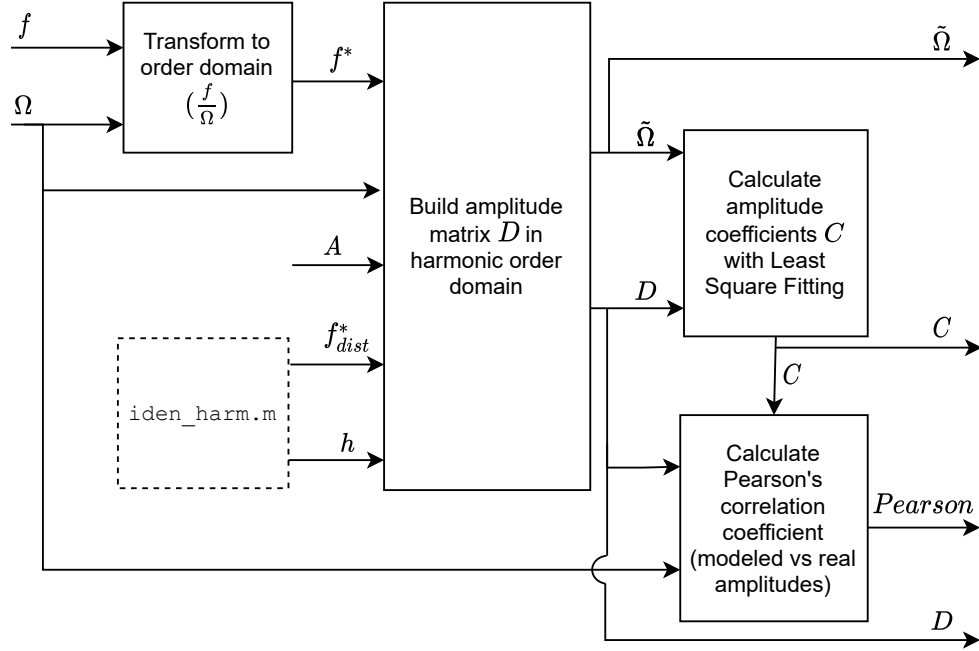


Figure 5.5: Amplitude coefficient calculation block

Where the input/output parameters that are not already included in table 5.1 are described in the table below:

Name	Description	Unit
D	Amplitude map (matrix) corresponding to harmonic orders h only	N or Nm
$\tilde{\Omega}$	Fan speed map (matrix) corresponding to harmonic orders h only	$rps(Hz)$
C	Array of calculated amplitude coefficients	kgm or kgm^2
$Pearson$	Pearson's coefficient	None (0 to 1)

Table 5.2: Empirical model parameters (2)

First of all, a vector of normalized frequencies f^* is obtained, exactly like in the first step of the `iden_harm` function.

Then, an amplitude map D is built, such that only disturbance peaks at the selected harmonic orders are saved, while at all other locations the map is equal to 0. The matrix D therefore will have as many rows as the speed array Ω and as many columns as the order array h . The construction of this matrix is done by iterating over rows and columns of f^* . First, the script double-checks whether f_{ij}^* is contained in f_{dist}^* , that is to say if it corresponds to a disturbance peak. If so, a further iteration begins over the harmonic orders h_k , to check for the existence of peaks close to these orders, within a given tolerance range. This is expressed by the following condition:

$$h_k - \epsilon \leq f_{ij}^* \leq h_k + \epsilon \quad (5.6)$$

The tolerance was chosen as 0.05 in this case too.

For all indices i, j, k , satisfying the condition above, the D matrix can then be updated as follows:

$$D_{ik} = A_{ij} \quad (5.7)$$

Furthermore, also a corresponding map of fan speeds is created in the same way. This will be especially useful for plotting:

$$\tilde{\Omega}_{ik} = \Omega_i \quad (5.8)$$

The amplitude coefficients can now be calculated. This is done via a Least Square Approximation of the columns of D , corresponding to one single harmonic order. This approximation is an optimization of the error between the real and expected disturbance. The assumption, as can also be inferred by equation 5.1, is that the expected disturbance amplitude is as follows:

$$E(D_{ik}) = C_k \tilde{\Omega}_{ik}^2 \quad (5.9)$$

The error will then be:

$$e_{ik} = D_{ik} - E(D_{ik}) = D_{ik} - C_k \tilde{\Omega}_{ik}^2 \quad (5.10)$$

The error must then be squared and summed over speeds at a constant harmonic order h_k (where m is the number of speeds):

$$\sum_{i=1}^m e_{ik}^2 = \sum_{i=1}^m D_{ik}^2 - 2C_k \sum_{i=1}^m \tilde{\Omega}_{ik}^2 D_{ik} + C_k^2 \sum_{i=1}^m \tilde{\Omega}_{ik}^4 \quad (5.11)$$

A minimization can be done by equaling the derivative of the error with respect to C_k to 0:

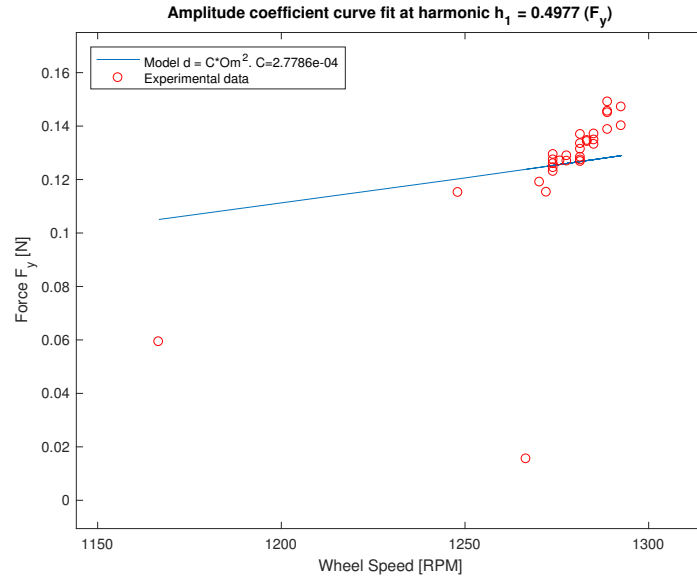
$$\frac{\partial}{\partial C_k} \sum_{i=1}^m e_{ik}^2 = -2 \sum_{i=1}^m \tilde{\Omega}_{ik}^2 D_{ik} + 2C_k \sum_{i=1}^m \tilde{\Omega}_{ik}^4 = 0 \quad (5.12)$$

Which yields the final Least Squares Approximation for C_k :

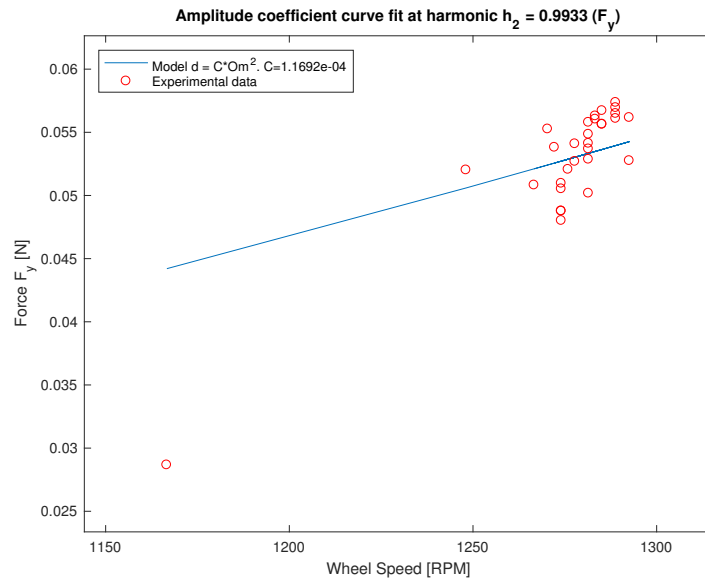
$$C_k = \frac{\sum_{i=1}^m D_{ik} \tilde{\Omega}_{ik}^2}{\sum_{i=1}^m \tilde{\Omega}_{ik}^4} \quad (5.13)$$

The script then calculates a correlation coefficient between each modeled amplitude $E(D_{ik})$ and the true amplitude D_{ik} . The correlation coefficient to experimental data in the case of Least Square methods is often called Pearson's coefficient and it is a direct measure of the quality of the model.

Finally, for each harmonic order h_k , the script plots the true and modeled amplitudes and shows the corresponding calculated amplitude coefficient C_k on the plot. Some examples are shown in the figure 5.6 below:



(a) $C_1 = 2.7786e-4 \text{ kgm}$; $Pearson = 0.6397$



(b) $C_2 = 1.1692e-4 \text{ kgm}$; $Pearson = 0.9037$

Figure 5.6: Least Squares Approximation model and data - USBfan F_y data

The final outputs of `find_coeff` are: $\tilde{\Omega}$, C , D and $Pearson$.

5.1.3. Mode removal

The `remove_mode` script works very similarly to `find_coeff`. Its only additional feature, besides calculating the coefficients, is to remove some data of D_{ik} within a certain range of given speeds (inside $\tilde{\Omega}_{ik}$). Therefore, two new matrices of acceptable speeds and data are constructed, and the amplitude coefficient is calculated again with 5.13, exactly like in the "find coefficient" procedure.

There are some ranges of data where the experimental amplitudes don't follow exactly the quadratic model. Here, some spikes are likely caused by the resonance of these fan speeds with the fan modes. Beware that the bracket modes were chosen on purpose for the speed ranges of the fan to get close to its resonance modes, so the whole range of data should be amplified, but the fan modes are unknown and could influence

the results. Furthermore, bracket modes will be accounted for later in the unified model, with a transmissibility function 5.67. In the case of the fan resonance modes, instead, it may be possible that only a portion of data is amplified by resonance. To make sure that this resonance does not corrupt data, the experimental data in this range can be ignored and the amplitude coefficient can be recalculated only with the rest of the data. This is done by visual inspection of the amplitude coefficient model vs data plots (as in figure 5.6), to check for any unwanted spikes that deviate too much from the quadratic model. Then, a user-defined RPM range of unwanted data is given in input to the `remove_mode.m` function, together with the old C array, the D and \tilde{Q} matrices, and the index k of the harmonic order of interest, and it outputs the new C_k , D_k , \tilde{Q}_k and $Pearson$ for that harmonic. An example is shown in the figure below.

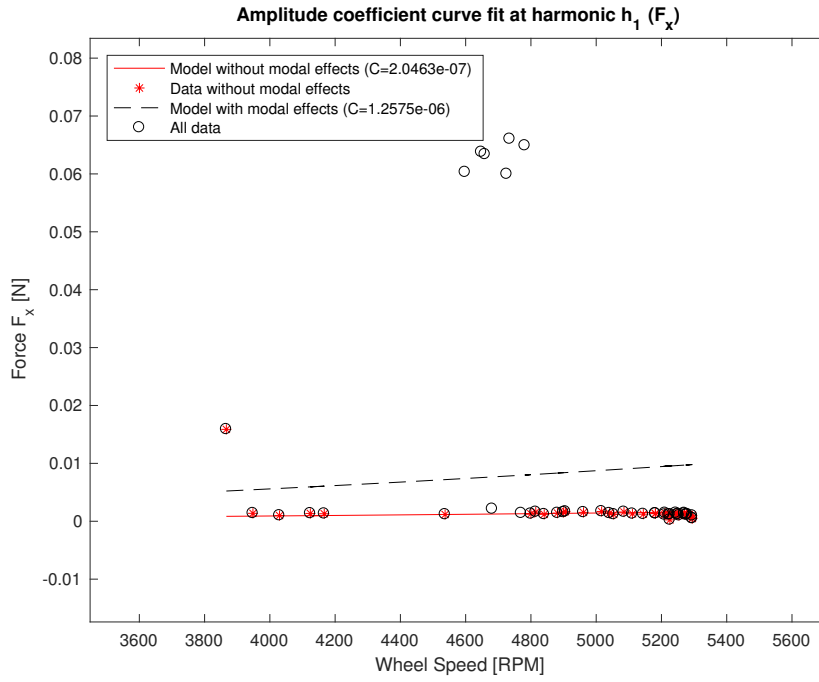


Figure 5.7: Example of mode removal at $h_1=0.388$. $C_{1old} = 1.2575e-6 \text{ kgm}$; $C_{1new} = 2.0463e-7 \text{ kgm}$. $Pearson_{old} = -0.2368$; $Pearson_{new} = -0.4532$. Pi-Fan 5V F_x data.

The data marked in red are the data not corrupted by modal effect and which therefore have not been removed. The data not marked in red and represented only by an empty black circle have been removed. The dashed line represents the model before removing these data, and the red line the new model.

However, in this case, it was still more likely that these peaks were caused by the whole bracket modes rather than by the fan modes alone. That is because fan eigenfrequencies are expected to be far from the ones of the mounting bracket (otherwise they would resonate at their own rated speed) and to affect the results only in a negligible way compared to the whole system. Therefore, it was decided not to use the `remove_mode` function for these data and accept the results in their whole range.

5.1.4. Comparison of model and data

The empirical model has now produced all necessary data to make a comparison with the experimental results. These data just need to undergo some final manipulation in the `comp_model.m` script and in the last section of `empirical_model`, so that four final plots can be produced for the input disturbance, namely:

- Waterfall plots of the amplitude (peak) spectra of experimental data and model
- Waterfall plots of the PSD (Power Spectral Density) of experimental data and model
- Model vs test data Amplitude and Cumulative RMS over frequency plot at one given speed
- Model vs test data RMS over speed plot

Before these plots are shown, a brief explanation of the newly introduced terms, such as PSD, RMS, and cumulative RMS, is going to be given.

First of all, the power spectrum is calculated (with the option `'power'`, as opposed to `'peak'`) by the `rpmfreqmap` function, with a Fourier transform, which corresponds to the following equation, where $x(t)$ is the input disturbance array and $Y(f)$ its analogous in the frequency domain:

$$P = \int_{-\infty}^{+\infty} x(t)^2 dt = \int_{-\infty}^{+\infty} |Y(f)|^2 df \quad (5.14)$$

The PSD of the experimental data, indicated as S here, can then be simply calculated as the power per unit frequency, where the frequency, in this case, is the frequency interval Δf of the Fourier transform returned by the `rpmfreqmap` function.

$$S(f) = \frac{P(f)}{\Delta f} \quad (5.15)$$

The PSD is in fact a measure of the signal's power content versus frequency, and it has units of N^2/Hz for forces and N^2m^2/Hz for torques. Therefore, the PSD amplitudes will not be a good validation for the amplitude coefficients, because these coefficients were retrieved from peak amplitude values. However, since PSD is amplified with respect to real peaks and it's independent of frequency resolution, it can be a better indicator of the validity of the harmonic numbers h , given that a better visual inspection of the comparison plots is possible. That is why PSD waterfall plots of model and data are going to be compared.

The inputs of the `comp_model` function are therefore the following arrays: h , C (calculated in the harmonic identification block), S , A of the data (calculated by `rpmfreqmap`), f and Ω . The script is then quickly recalculating the empirical model harmonic frequency and amplitude matrices, through the following equations:

$$\omega_{modik} = h_k \Omega_i \quad (5.16)$$

$$A_{modik} = C_k \Omega_i^2 \quad (5.17)$$

These parameters can directly be compared with the f and A input variables, through waterfall plots, as shown below:

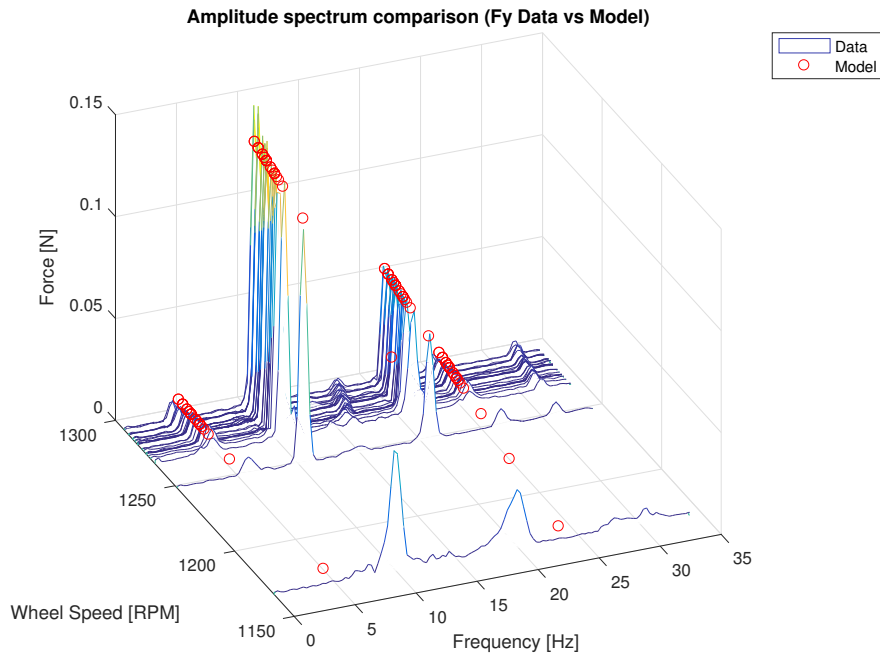


Figure 5.8: Amplitude spectrum comparison of experimental data and empirical model. USBfan F_y data.

It can already be noticed that the amplitudes match the data well in this case, and the harmonic numbers have been recognized correctly, since the red dots, representing the empirical model, are all above disturbance ridges. However, two ridges have not been classified as disturbance, but rather as noise, even though they are only slightly smaller than two of the disturbance ridges. This, if desired, could be further improved by regulating the tolerances for the Disturbance Threshold in the noise analysis.

Then, the PSD of the model can be calculated directly from the modeled peak amplitude spectrum through the following equation:

$$S_{mod} = \frac{1}{2} \frac{A_{mod}^2}{\Delta f} \quad (5.18)$$

The factor 2 comes from a procedure performed inside the Fourier transform, to convert double-sided spectra into single-sided spectra, which are double in amplitude [42].

The PSD's of model and data can now be compared as well:

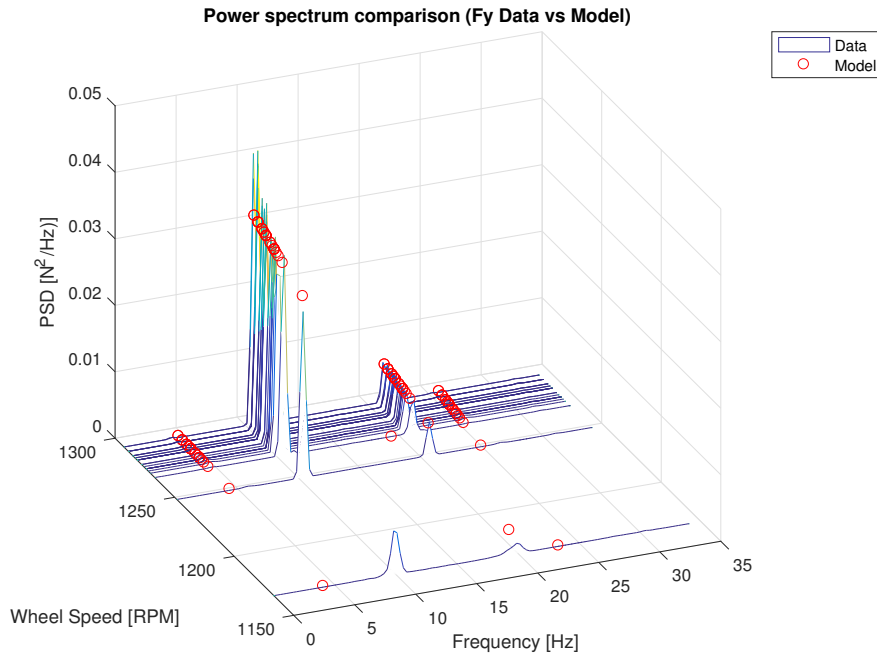


Figure 5.9: Power Spectral Density comparison of experimental data and empirical model. USBfan F_y data.

In this case, however, since original amplitudes are always smaller than 1, the result is not an amplification factor but rather a shrinking one. PSD's are generally useful for identifying where the greatest changes in energy happen within the signal, by amplifying the difference between small and large peaks. This will be even more evident when calculating the corresponding variance or cumulative RMS, which are directly related to the area under the PSD.

Further estimators of the quality of the model can now be calculated. To get to the definition of variance, it is useful to first define the autocorrelation function, which is an estimator of how well a random process $X(t)$ (such as vibrations) correlates with itself at two instants in time:

$$R_X(\tau) = E[X(t)X(t + \tau)] \quad (5.19)$$

Where $E[\cdot]$ is the estimation function.

Variance σ^2 , instead, can be defined as an estimate of the mean-square of a process:

$$\sigma_X^2(t) = E[X(t) - \mu_X(t)]^2 \quad (5.20)$$

Where $\mu_X(t)$ is the mean of process $X(t)$.

Vibrations can generally be approximated as zero-mean processes, meaning that the phase, as defined in equation 5.1, is assumed to be uniformly distributed between 0 and 2π . That means that $\mu_X(t)$ equals zero, and the variance is then equal to the autocorrelation function for $\tau = 0$:

$$\sigma_X^2(t) = R_X(0) = E[X(t)^2] \quad (5.21)$$

Now, the autocorrelation function is also defined as the inverse Fourier transform of the PSD, which, for $\tau = 0$, simply equals the integral of PSD over frequency:

$$R_X(\tau) = \mathcal{F}^{-1}[S_X(f)] = \int_{-\infty}^{+\infty} S_X(f) e^{i\omega\tau} df \quad (5.22)$$

$$R_X(0) = \sigma_X^2(t) = \int_{-\infty}^{+\infty} S_X(f) df \quad (5.23)$$

That means variance, for random zero-mean processes, equals the area under the PSD in PSD-frequency plots.

For this model, recalling equation 5.1, the autocorrelation can be written as:

$$R_X(\tau) = \sum_{k=1}^n \frac{C_k^2 \Omega_i^4}{2} \cos(\Omega_i h_k \tau) \quad (5.24)$$

The variance of the model, that is the autocorrelation in 0, is calculated as:

$$\sigma_{mod}^2 = \sum_{k=1}^n \frac{C_k^2 \Omega_i^4}{2} \quad (5.25)$$

Also, for zero-mean processes, the total RMS, here indicated as σ_X , is equal to the square root of the variance. For the model, therefore, the RMS can be calculated as such:

$$\sigma_{mod} = \sqrt{\sigma_{mod}^2} \quad (5.26)$$

The cumulative RMS, instead, or CRMS, is equal to the square root of the cumulative integral (up to a certain value of frequency f_1, f_2, \dots, f_{end}) of the PSD:

$$CRMS = \left[\sqrt{\int_{f_1}^{f_1} S(f) df}, \sqrt{\int_{f_1}^{f_2} S(f) df}, \dots, \sqrt{\int_{f_1}^{f_{end}} S(f) df} \right]^T \quad (5.27)$$

Therefore, the CRMS contains all values of RMS up to the final frequency, and in all intermediate intervals, while the RMS is the whole integral calculated only until the last frequency. Therefore, at each speed, the last value of CRMS is always equal to the corresponding RMS.

The CRMS is therefore calculated as in equation 5.27, both for the data and the model, through the in-built MATLAB function `cumtrapz`, approximating the cumulative integral of the PSD's S and S_{mod} .

The RMS of the model, instead, is calculated as the square root of the variance, as explained in equation 5.26, while the RMS of the data is calculated as the square root of the integral of the PSD S , with the function `trapz`. By double-checking the last values of the CRMS and these RMS arrays, it can be verified that they are the same.

Figure 5.10 shows an example of CRMS over frequency at a chosen speed, for model and data, below the corresponding amplitude plot.

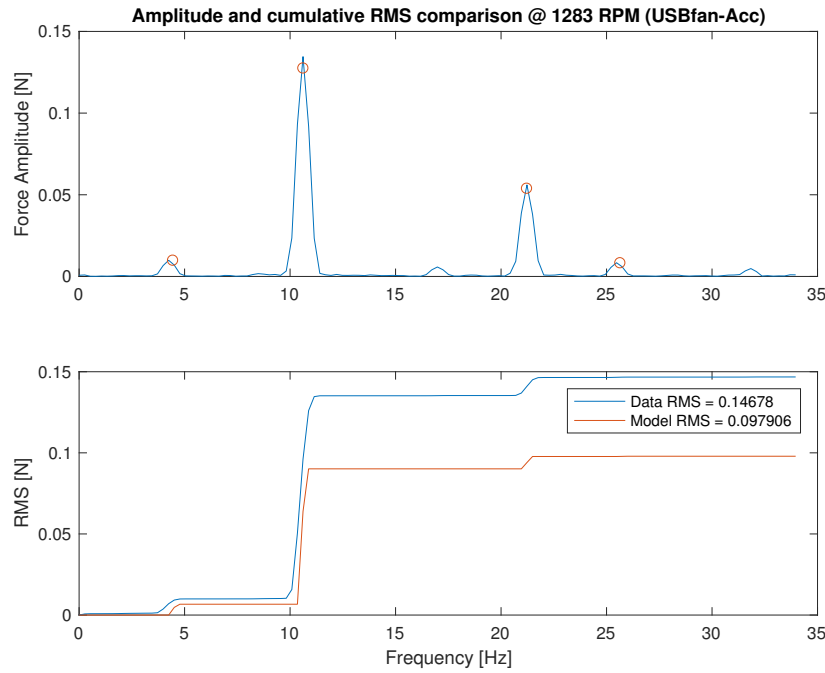


Figure 5.10: Data vs Empirical model: Peak Amplitudes and cumulative RMS comparisons. USBfan F_y data (@1283 RPM).

The plot shows that the energy content has a major increase at around 10 Hz , where the greatest peak is present, and then the cumulative RMS stays almost constant, growing only a little at the second peak at around 21 Hz . The CRMS of the model follows this trend. However, it underestimates the experimental values, probably because small peaks were discarded and wrongly considered as noise. At the end of the CRMS plot, it can be seen that the total RMS values are respectively 0.1468 and 0.0979 for the data and the model, indicating that there's a 33.3% error between the two.

Below, these values can also be seen in the RMS over speeds plot, and they even grow at larger speeds:

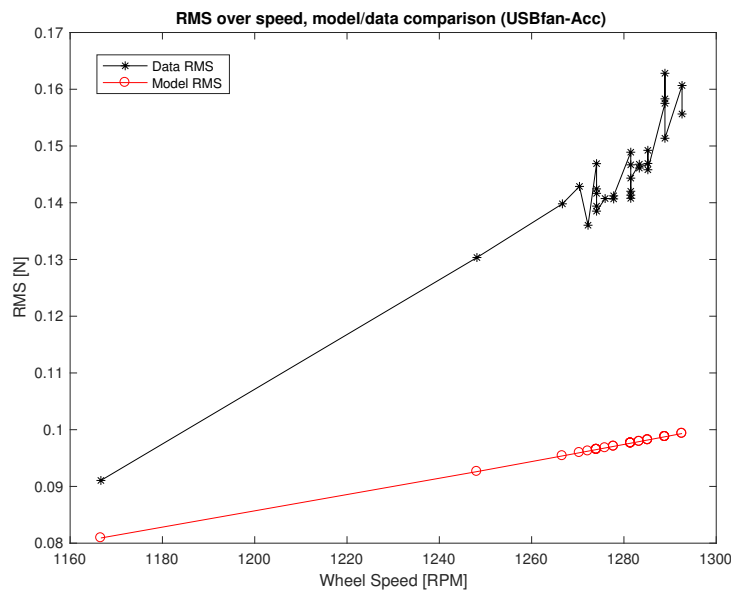


Figure 5.11: Data vs Empirical model: Total RMS over speed comparison. USBfan F_y data.

5.2. Analytical model

In this section, the equations of motion of the test bench will be derived.

An energetic approach will be used, starting from the kinematics of the system and the definition of kinetic and potential energy. Then, the equations of motion will be written analytically through a Lagrangian approach 5.38.

Throughout this discussion, figure 5.12, representing a simplified model of the test setup with a balanced fan on top, can be referred to as the rationale behind the writing of the equations and necessary parameters. A more in-depth explanation of how parameters were calculated or where they were taken from is summarized in table 5.5, paragraph 5.3.2, after the derivation of all equations.

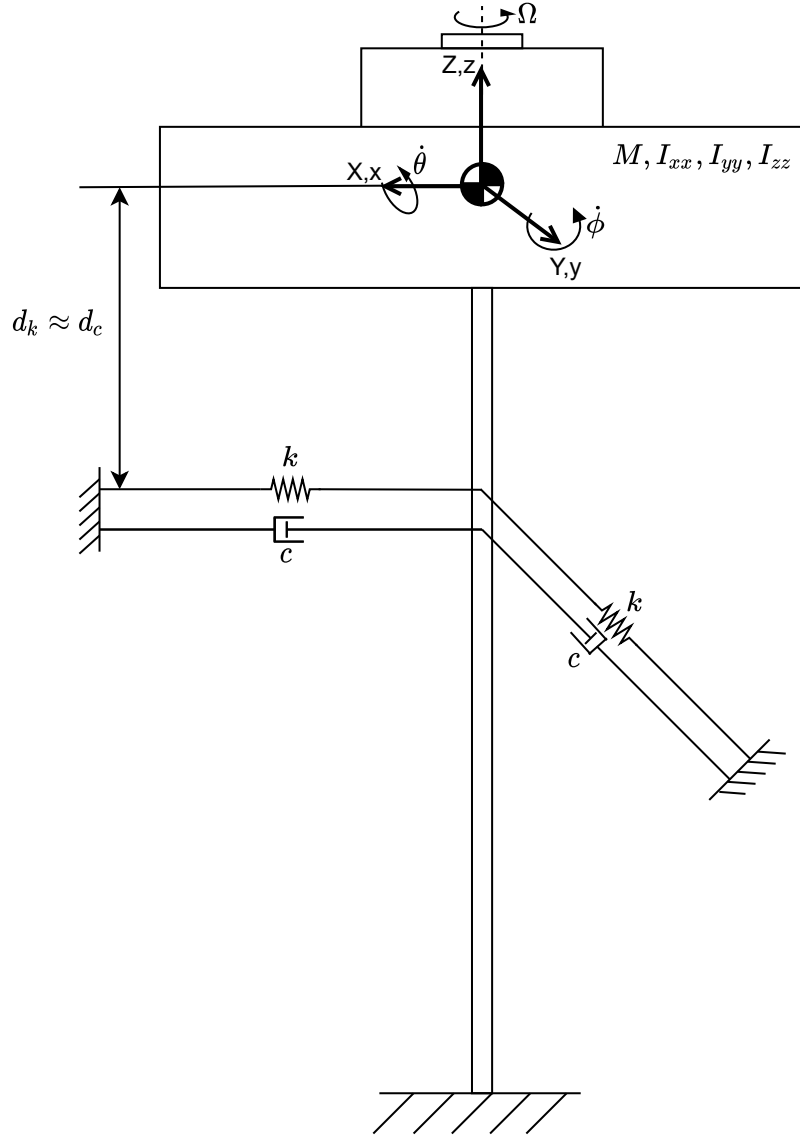


Figure 5.12: Analytical model of the balanced test setup

The coordinate frames represented in the figure above are the ground-fixed frame XYZ and the body-fixed frame xyz , which are coincident in a static condition. A full definition of frames will be given in 5.13. The radial stiffness k and damping c of the iron bars are represented here as a couple of springs and dashpots along x and z , at an imaginary distance d_k and d_c from the center of mass of the system.

Note that this test bench may look like a coupled system (mounting bracket and reaction wheel). Coupled microvibration setups have been studied several times recently [14][43][44][15], to simulate the behavior of

reaction wheels when they are fixed to spacecraft in space. However, their main feature is that they are used in a free-free boundary condition. That means the reaction wheel is fixed to a representative support structure, which is "floating" (usually hooked to a ceiling with ropes) to simulate in-orbit conditions. Therefore, coupled models are used in this case, with more extensive equations, where the dynamics of the spacecraft-representative support is included and a coupled influence between this and the wheel dynamics (and hence also microvibrations) happens.

When the support (i.e. mounting bracket) is fixed to the ground, instead, the system is never coupled [43, p. 39]. In this case, the setup is tested in hard-mounted conditions, and therefore the equations will be similar to the case of a wheel directly fixed to a Kistler table [10][27]. However, there are obvious differences due to the stiffness of the iron bars in the mounting bracket (a soft-suspension system with low stiffness). Furthermore, the displacement of the test bench in the z direction is not representative of the fan axial movement, since it's limited by the four iron bars. The coordinate z will thus not be present in this model, and that is why the axial stiffness and damping are not drawn in figure 5.12. Hence, the system will just have four degrees of freedom (the two radial coordinates x and y and the rotations around them θ and ϕ). The rotation around z is also excluded because it's not representative of the fan rotation.

Therefore, the dynamics of the whole test system, rather than that of the fans only, will be studied, assuming no motion at the interface between the fans and the mounting bracket. Of course, the amplification of microvibrations that happens thanks to the mounting bracket will also be taken into account, through a transmissibility function 5.67.

The first step in the energetic approach is to define all coordinate frames and corresponding Tait-Bryan angles (of rotation), so that the kinematics of the system can be defined in one single frame and conversions from one frame to another can be done where necessary. Tait-Bryan angles are exactly like Euler angles, except for the fact that the rotation sequence between the defined frames differs. While for proper Euler angles the first and third rotation occur around the same (transformed) axes (e.g. $z - x' - z''$), for Tait-Bryan angles they can happen about three distinct axes (e.g. $x - y' - z''$). In this case, the rotation sequence will be $Y - x' - z''$ and the frames are shown in the figure below and defined in table 5.3:

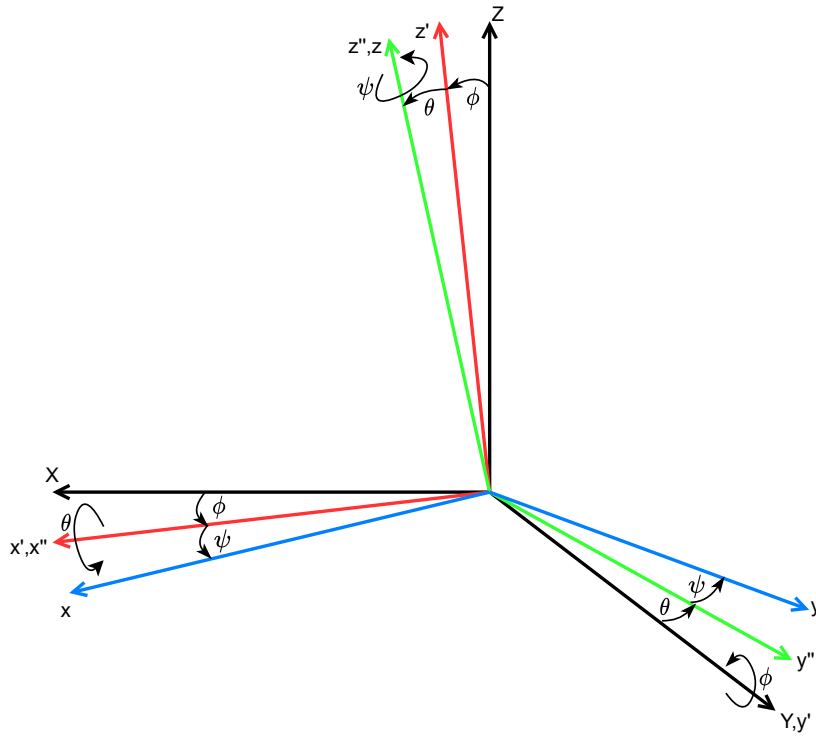


Figure 5.13: Coordinate frames and Tait-Bryan rotations

Coordinate Frame	Name	Transformation
XYZ	Ground-fixed frame	$\begin{bmatrix} 1 & 0 & 0 \\ 0 & 1 & 0 \\ 0 & 0 & 1 \end{bmatrix}$
$x'y'z'$	Intermediate frame	$\begin{bmatrix} \cos\phi & 0 & \sin\phi \\ 0 & 1 & 0 \\ -\sin\phi & 0 & \cos\phi \end{bmatrix}$
$x''y''z''$	Rocking frame	$\begin{bmatrix} 1 & 0 & 0 \\ 0 & \cos\theta & -\sin\theta \\ 0 & \sin\theta & \cos\theta \end{bmatrix}$
xyz	Body-fixed frame	$\begin{bmatrix} \cos\psi & -\sin\psi & 0 \\ \sin\psi & \cos\psi & 0 \\ 0 & 0 & 1 \end{bmatrix}$

Table 5.3: Coordinate frames names and Tait-Bryan transformation sequence for the fan test bench model

So, to get from ground-fixed frame to body-fixed frame ($XYZ \rightarrow xyz$), first, there is a rotation ϕ about the ground-fixed axis Y , then a rotation θ about the intermediate axis x' , and lastly a rotation ψ around the rocking axis z'' . The transformation matrices shown in table 5.3 describe the transformation that occurs from the previous to the current frame (besides which the matrix is written).

To find the Lagrangian and the equations of motion 5.38, first, the kinetic energy, the potential energy, and the virtual external work of the system must be written. These can be defined as follows.

Definition of kinetic energy:

$$T = \frac{1}{2}\omega^T I \omega + \frac{1}{2}M v^T v \quad (5.28)$$

Definition of potential energy:

$$V = \sum_{k=1}^{n_k} \frac{1}{2} k_k X_k(q)^2 \quad (5.29)$$

Where n_k is the number of elastic elements in the system and X_k is the elongation function of the k^{th} spring, which is dependent on one or more generalized coordinates q .

Definition of virtual external work (of dissipative forces, in this case), according to D'Alembert's principle:

$$\delta W = - \sum_{d=1}^{n_d} c_d \dot{X}_d(q) \cdot \delta X_d(q) \quad (5.30)$$

Where n_d is the number of dissipative elements in the system and \dot{X}_d and δX_d are the elongation velocity and virtual displacement of the d^{th} dashpot (damper), which are dependent on one or more generalized coordinates q .

Then, the angular and translational velocities must be found to write an expression of the kinetic energy of the system.

The angular velocity of the system is:

$$\vec{\omega} = \dot{\theta} \hat{u}_{x'} + \dot{\phi} \hat{u}_Y + \Omega \hat{u}_{z''} \quad (5.31)$$

Where $\dot{\theta}$ and $\dot{\phi}$ are conveniently written in the coordinate frames in which they were defined, and Ω is the fan spin rate ($\dot{\psi} = \Omega = \text{const}$ for the purpose of this model, meaning there is a quasi-steady-state assumption, as explained in section 5.1 and later in section 5.3).

To be able to find an expression of kinetic energy, however, angular velocity first needs to be written in the coordinates of a single frame. Therefore, 5.31 is converted into rocking frame coordinates (x'', y'', z''), according to the rotation matrices written above (by pre-multiplying by their transpose):

$$\begin{aligned} \dot{\theta} \hat{u}_{x'} : & \begin{bmatrix} 1 & 0 & 0 \\ 0 & \cos \theta & \sin \theta \\ 0 & -\sin \theta & \cos \theta \end{bmatrix} \begin{bmatrix} \dot{\theta} \\ 0 \\ 0 \end{bmatrix} = \dot{\theta} \hat{u}_{x''} \\ \dot{\phi} \hat{u}_Y : & \begin{bmatrix} 1 & 0 & 0 \\ 0 & \cos \theta & \sin \theta \\ 0 & -\sin \theta & \cos \theta \end{bmatrix} \begin{bmatrix} \cos \phi & 0 & -\sin \phi \\ 0 & 1 & 0 \\ \sin \phi & 0 & \cos \phi \end{bmatrix} \begin{bmatrix} 0 \\ \dot{\phi} \\ 0 \end{bmatrix} = \begin{bmatrix} 0 \\ \dot{\phi} \cos \theta \\ -\dot{\phi} \sin \theta \end{bmatrix} = \dot{\phi} \cos \theta \hat{u}_{y''} - \dot{\phi} \sin \theta \hat{u}_{z''} \\ & \Downarrow \\ \vec{\omega} = & \dot{\theta} \hat{u}_{x''} + \dot{\phi} \cos \theta \hat{u}_{y''} + (\Omega - \dot{\phi} \sin \theta) \hat{u}_{z''} \end{aligned} \quad (5.32)$$

The translational velocity in rocking frame coordinates (x'', y'', z'') is:

$$\vec{v} = \dot{x} \hat{u}_{x''} + \dot{y} \hat{u}_{y''} \quad (5.33)$$

By substituting 5.32 and 5.33 into 5.28, the kinetic energy can be written:

$$T = \frac{1}{2} [I_{xx} \dot{\theta}^2 + I_{yy} \dot{\phi}^2 \cos^2 \theta + I_{zz} (\Omega - \dot{\phi} \sin \theta)^2 + M(\dot{x}^2 + \dot{y}^2)] \quad (5.34)$$

The potential energy of the system is:

$$\begin{aligned} V &= \frac{1}{2} k(x + d_k \sin \phi)^2 + \frac{1}{2} k(y - d_k \sin \theta)^2 \\ &= \frac{1}{2} kx^2 + kxd_k \sin \phi + \frac{1}{2} kd_k^2 \sin^2 \phi + \frac{1}{2} ky^2 - kyd_k \sin \theta + \frac{1}{2} kd_k^2 \sin^2 \theta \\ &= \frac{1}{2} k[x^2 + y^2 + d_k^2(\sin^2 \phi + \sin^2 \theta) + 2xd_k \sin \phi - 2yd_k \sin \theta] \end{aligned} \quad (5.35)$$

The virtual external work is:

$$\begin{aligned} \delta W &= -c[(\dot{x} + \dot{\phi} d_c \cos \phi)(\delta x + \delta \phi d_c \cos \phi) + (\dot{y} - \dot{\theta} d_c \cos \theta)(\delta y - \delta \theta d_c \cos \theta)] \\ &= -c(\dot{x} \delta x + \dot{x} \delta \phi d_c \cos \phi + \delta x \dot{\phi} d_c \cos \phi + \dot{\phi} \delta \phi d_c^2 \cos^2 \phi \\ &\quad + \dot{y} \delta y - \dot{y} \delta \theta d_c \cos \theta - \delta y \dot{\theta} d_c \cos \theta + \dot{\theta} \delta \theta d_c^2 \cos^2 \theta) \end{aligned} \quad (5.36)$$

The Lagrangian, then, can be defined and written as follows:

$$\mathcal{L} = T - V = \frac{1}{2} [I_{xx}\dot{\theta}^2 + I_{yy}\dot{\phi}^2 \cos^2 \theta + I_{zz}(\Omega - \dot{\phi} \sin \theta)^2 + M(\dot{x}^2 + \dot{y}^2)] - \frac{1}{2} k[x^2 + y^2 + d_k^2(\sin^2 \phi + \sin^2 \theta) + 2xd_k \sin \phi - 2yd_k \sin \theta] \quad (5.37)$$

The equations of motion, according to Lagrange theory, are defined as:

$$\frac{d}{dt} \left(\frac{\partial \mathcal{L}}{\partial \dot{q}_i} \right) - \frac{\partial \mathcal{L}}{\partial q_i} = \frac{\partial \delta W}{\partial \delta q_i} \quad (5.38)$$

The right-hand sides of the equations, then, can be expressed as:

$$\frac{\partial \delta W}{\partial \delta x} = -c\dot{x} - c\dot{\phi}d_c \cos \phi \quad (5.39)$$

$$\frac{\partial \delta W}{\partial \delta y} = -c\dot{y} + c\dot{\theta}d_c \cos \theta \quad (5.40)$$

$$\frac{\partial \delta W}{\partial \delta \theta} = -cd_c^2\dot{\theta} \cos^2 \theta + c\dot{y}d_c \cos \theta \quad (5.41)$$

$$\frac{\partial \delta W}{\partial \delta \phi} = -cd_c^2\dot{\phi} \cos^2 \phi - c\dot{x}d_c \cos \phi \quad (5.42)$$

Finally, after substituting 5.37 and 5.39 → 5.42 into 5.38, the full equations are obtained for each generalized coordinate:

x:

$$M\ddot{x} + kx + kd_k \sin \phi + c(\dot{x} + \dot{\phi}d_c \cos \phi) = 0 \quad (5.43)$$

y:

$$M\ddot{y} + k(y - d_k \sin \theta) + c(\dot{y} - \dot{\theta}d_c \cos \theta) = 0 \quad (5.44)$$

θ:

$$I_{xx}\ddot{\theta} + I_{yy}\dot{\phi}^2 \cos \theta \sin \theta + \Omega I_{zz}\dot{\phi} \cos \theta - I_{zz}\dot{\phi}^2 \cos \theta \sin \theta + kd_k^2 \sin \theta \cos \theta - kyd_k \cos \theta + c(d_c^2\dot{\theta} \cos^2 \theta - \dot{y}d_c \cos \theta) = 0 \quad (5.45)$$

φ:

$$I_{yy}\ddot{\phi} \cos^2 \theta - 2I_{yy}\dot{\phi}\dot{\theta} \cos \theta \sin \theta - \Omega I_{zz}\dot{\phi} \cos \theta + I_{zz}\ddot{\phi} \sin^2 \theta + 2I_{zz}\dot{\phi}\dot{\theta} \cos \theta \sin \theta + kd_k^2 \sin \phi \cos \phi + kxd_k \cos \phi + c(d_c^2\dot{\phi} \cos^2 \phi + \dot{x}d_c \cos \phi) = 0 \quad (5.46)$$

The equations can be linearized around the static equilibrium position ($\theta_0 = 0, \phi_0 = 0$), where also $\dot{\theta}_0, \ddot{\theta}_0, \dot{\phi}_0, \ddot{\phi}_0$ equal 0. With the assumption of small-angle displacements around the equilibrium position, every linearization can be performed as a first-order Taylor series approximation:

$$f(\alpha, \beta) = f(\alpha_0, \beta_0) + \left. \frac{\partial f}{\partial \alpha} \right|_{\alpha_0, \beta_0} (\alpha - \alpha_0) + \left. \frac{\partial f}{\partial \beta} \right|_{\alpha_0, \beta_0} (\beta - \beta_0)$$

Where (α_0, β_0) is the static equilibrium position.

Therefore, besides the known approximations $\sin \theta \approx \theta$ and $\cos \theta \approx 1$, the following linearizations are calculated:

$$\dot{\phi} \cos \theta \approx \dot{\phi}_0 \cos \theta_0 + \left. \cos \theta \right|_{\theta_0} (\dot{\phi} - \dot{\phi}_0) + \left. \dot{\phi}(-\sin \theta) \right|_{\theta_0, \dot{\phi}_0} (\theta - \theta_0) = \dot{\phi}$$

$$\dot{\phi}^2 \cos \theta \sin \theta \approx \dot{\phi}_0^2 \cos \theta_0 \sin \theta_0 + 2\dot{\phi} \cos \theta \sin \theta \Big|_{\dot{\phi}_0, \theta_0} (\dot{\phi} - \dot{\phi}_0) + \dot{\phi}^2 (\cos^2 \theta - \sin^2 \theta) \Big|_{\dot{\phi}_0, \theta_0} (\theta - \theta_0) = 0$$

$$\sin \theta \cos \theta \approx \sin \theta_0 \cos \theta_0 + (\cos^2 \theta - \sin^2 \theta) \Big|_{\theta_0} (\theta - \theta_0) = \theta$$

$$\ddot{\phi} \cos^2 \theta \approx \ddot{\phi}_0 \cos^2 \theta_0 + \cos^2 \theta \Big|_{\theta_0} (\ddot{\phi} - \ddot{\phi}_0) + \ddot{\phi} (2 \cos \theta \sin \theta) \Big|_{\ddot{\phi}_0, \theta_0} (\theta - \theta_0) = \ddot{\phi}$$

$$\dot{\phi} \dot{\theta} \cos \theta \sin \theta \approx \dot{\phi}_0 \dot{\theta}_0 \cos \theta_0 \sin \theta_0 + \dot{\theta} \cos \theta \sin \theta \Big|_{\dot{\theta}_0, \theta_0} (\dot{\phi} - \dot{\phi}_0) + \dot{\phi} \cos \theta \sin \theta \Big|_{\dot{\phi}_0, \theta_0} (\dot{\theta} - \dot{\theta}_0) + \dot{\phi} \dot{\theta} (\cos^2 \theta - \sin^2 \theta) \Big|_{\dot{\phi}_0, \dot{\theta}_0, \theta_0} (\theta - \theta_0) = 0$$

$$\ddot{\phi} \sin^2 \theta \approx \ddot{\phi}_0 \sin^2 \theta_0 + \sin^2 \theta \Big|_{\theta_0} (\ddot{\phi} - \ddot{\phi}_0) + \ddot{\phi} (2 \sin \theta \cos \theta) \Big|_{\ddot{\phi}_0, \theta_0} (\theta - \theta_0) = 0$$

Therefore, the linearized equations of motion become:

$$M\ddot{x} + c(\dot{x} + d_c \dot{\phi}) + k(x + d_k \phi) = 0 \quad (5.47)$$

$$M\ddot{y} + c(\dot{y} - d_c \dot{\theta}) + k(y - d_k \theta) = 0 \quad (5.48)$$

$$I_{xx} \ddot{\theta} + \Omega I_{zz} \dot{\phi} + c(d_c^2 \dot{\theta} - d_c \dot{y}) + k(d_k^2 \theta - d_k y) = 0 \quad (5.49)$$

$$I_{yy} \ddot{\phi} - \Omega I_{zz} \dot{\theta} + c(d_c^2 \dot{\phi} + d_c \dot{x}) + k(d_k^2 \phi + d_k x) = 0 \quad (5.50)$$

or in matrix form:

$$\begin{bmatrix} M & 0 & 0 & 0 \\ 0 & M & 0 & 0 \\ 0 & 0 & I_{xx} & 0 \\ 0 & 0 & 0 & I_{yy} \end{bmatrix} \begin{bmatrix} \ddot{x} \\ \ddot{y} \\ \ddot{\theta} \\ \ddot{\phi} \end{bmatrix} + \begin{bmatrix} c & 0 & 0 & cd_c \\ 0 & c & -cd_c & 0 \\ 0 & -cd_c & cd_c^2 & \Omega I_{zz} \\ cd_c & 0 & -\Omega I_{zz} & cd_c^2 \end{bmatrix} \begin{bmatrix} \dot{x} \\ \dot{y} \\ \dot{\theta} \\ \dot{\phi} \end{bmatrix} + \begin{bmatrix} k & 0 & 0 & kd_k \\ 0 & k & -kd_k & 0 \\ 0 & -kd_k & kd_k^2 & 0 \\ kd_k & 0 & 0 & kd_k^2 \end{bmatrix} \begin{bmatrix} x \\ y \\ \theta \\ \phi \end{bmatrix} = \begin{bmatrix} 0 \\ 0 \\ 0 \\ 0 \end{bmatrix} \quad (5.51)$$

Now, it can be recalled from the introduction that the static imbalance can be modeled as a point mass m_s at one edge of the wheel, as in figure 1.1.

Similarly, the dynamic imbalance can be modeled as two point masses m_d at the sides of the wheel, as in figure 1.2.

The complete equations, including imbalances, will therefore contain these centrifugal forces/torques on the right-hand sides. To derive these equations for the unbalanced system, the kinetic energy will have to be updated and the Lagrangian should be calculated again. An updated model figure is shown below 5.14, representing also imbalance masses.

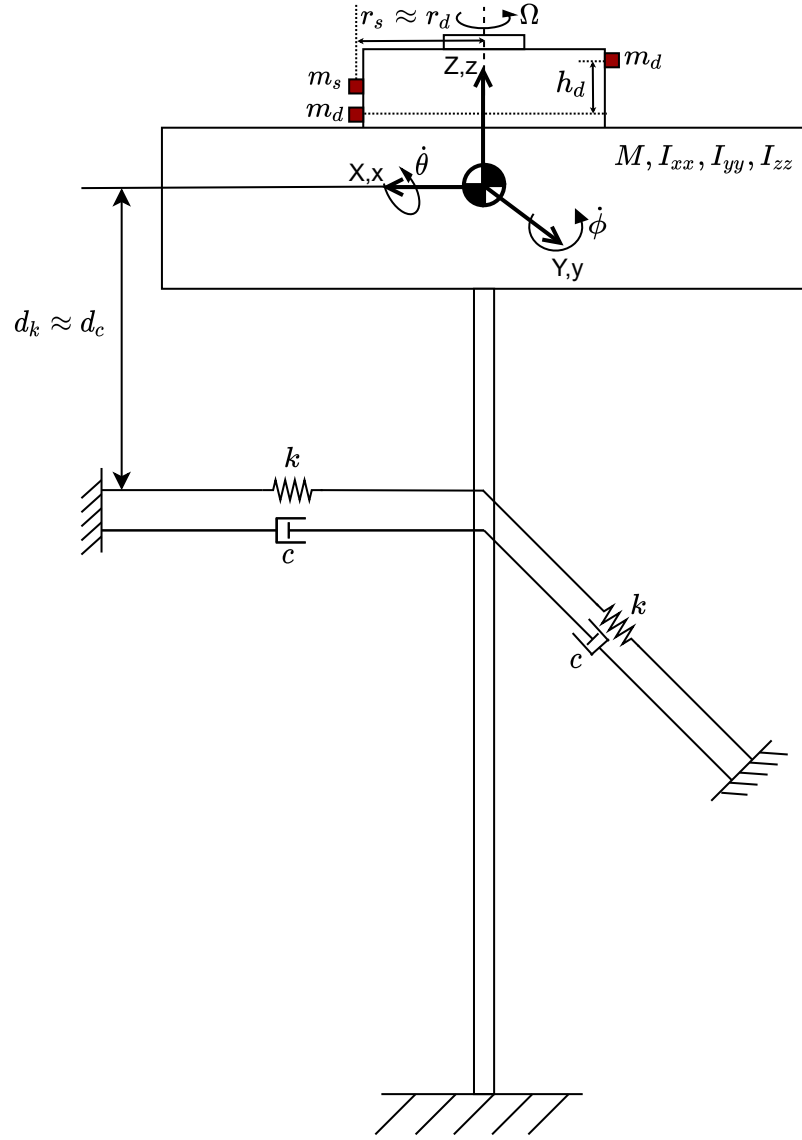


Figure 5.14: Analytical model of the unbalanced test setup

Let's assume for simplicity that – for the following calculations – a fan body-fixed reference frame (centered at the center of mass of the fan) is equivalent to the system body-fixed reference frame xyz since they move jointly (fan and top base are rigidly connected). The constant distance from the fan center of mass to the system center of mass is then ignored.

The positions of the imbalance point masses in a body-fixed frame can then be written respectively as:

$$\vec{u}_{m_s} = r_s \hat{u}_x \quad (5.52)$$

$$\vec{u}_{m_{d1}} = r_d \hat{u}_x - h_d \hat{u}_z \quad (5.53)$$

$$\vec{u}_{m_{d2}} = -r_d \hat{u}_x + h_d \hat{u}_z \quad (5.54)$$

Furthermore, the center of the wheel, due to the radial gap between the bearing and motor axis and bearing flexibility, can translate in the X-Y plane. This translation will be expressed as:

$$\vec{\Delta} = x \hat{u}_X + y \hat{u}_Y$$

Therefore, in a ground-fixed inertial frame, the static imbalance can be described as:

$$\vec{U}_{m_s} = \Phi \vec{u}_{m_s} + \vec{\Delta} \quad (5.55)$$

Where Φ is the direction cosine matrix from body-fixed to ground-fixed frame, calculated as a multiplication of all matrices, from last to first, listed in table 5.3.

Similarly:

$$\vec{U}_{m_{d_1}} = \Phi \vec{u}_{m_{d_1}} + \vec{\Delta} \quad (5.56)$$

$$\vec{U}_{m_{d_2}} = \Phi \vec{u}_{m_{d_2}} + \vec{\Delta} \quad (5.57)$$

Hence, by differentiating the imbalance positions and substituting the velocities in 5.34, the respective kinetic energies can be found and summed to the kinetic energy of the balanced system. The same procedure for the Lagrangian method is then repeated by substituting these equations in 5.37 so that the complete equations including imbalances can be derived:

$$\begin{aligned} & \begin{bmatrix} M_t & 0 & 0 & 0 \\ 0 & M_t & 0 & 0 \\ 0 & 0 & I_\theta & \frac{1}{2}\tilde{I}\sin(2\Omega t) \\ 0 & 0 & \frac{1}{2}\tilde{I}\sin(2\Omega t) & I_\phi \end{bmatrix} \begin{bmatrix} \ddot{x} \\ \ddot{y} \\ \ddot{\theta} \\ \ddot{\phi} \end{bmatrix} + \begin{bmatrix} c & 0 & 0 & cd_c \\ 0 & c & -cd_c & 0 \\ 0 & -cd_c & cd_c^2 - \Omega\tilde{I}\sin(2\Omega t) & \Omega I_{zz} + 2\Omega\tilde{I}\cos^2(\Omega t) \\ cd_c & 0 & -\Omega I_{zz} - 2\Omega\tilde{I}\sin^2(\Omega t) & cd_c^2 + \Omega\tilde{I}\sin(2\Omega t) \end{bmatrix} \begin{bmatrix} \dot{x} \\ \dot{y} \\ \dot{\theta} \\ \dot{\phi} \end{bmatrix} \\ & + \begin{bmatrix} k & 0 & 0 & kd_k \\ 0 & k & -kd_k & 0 \\ 0 & -kd_k & kd_k^2 & 0 \\ kd_k & 0 & 0 & kd_k^2 \end{bmatrix} \begin{bmatrix} x \\ y \\ \theta \\ \phi \end{bmatrix} = \begin{bmatrix} -U_s\Omega^2\sin\Omega t \\ U_s\Omega^2\cos\Omega t \\ U_d\Omega^2\cos\Omega t \\ U_d\Omega^2\sin\Omega t \end{bmatrix} \quad (5.58) \end{aligned}$$

Where

$$M_t = M + m_s + 2m_d \quad (5.59)$$

$$I_\theta = I_{xx} + 2m_d h^2 + \tilde{I}\cos^2\Omega t \quad (5.60)$$

$$I_\phi = I_{yy} + 2m_d h^2 + \tilde{I}\sin^2\Omega t \quad (5.61)$$

$$\tilde{I} = 2m_d r_d^2 + m_s r_s^2 \quad (5.62)$$

$$U_s = m_s r_s \quad (5.63)$$

$$U_d = 2m_d r_d h_d \quad (5.64)$$

Finally with the following assumptions, the equations can be further simplified:

$$\begin{aligned} & I_{xx}, I_{yy}, I_{zz} \gg \tilde{I} \\ & \Downarrow \\ & I_\theta \approx I_{xx} \\ & I_\phi \approx I_{yy} \\ & I_{zz} + 2\tilde{I}\cos^2(\Omega t) \approx I_{zz} \\ & \Downarrow \end{aligned} \quad (5.65)$$

$$\begin{aligned}
& \begin{bmatrix} M_t & 0 & 0 & 0 \\ 0 & M_t & 0 & 0 \\ 0 & 0 & I_{xx} & \frac{1}{2}\tilde{I}\sin(2\Omega t) \\ 0 & 0 & \frac{1}{2}\tilde{I}\sin(2\Omega t) & I_{yy} \end{bmatrix} \begin{bmatrix} \ddot{x} \\ \ddot{y} \\ \ddot{\theta} \\ \ddot{\phi} \end{bmatrix} + \begin{bmatrix} c & 0 & 0 & cd_c \\ 0 & c & -cd_c & 0 \\ 0 & -cd_c & cd_c^2 - \Omega\tilde{I}\sin(2\Omega t) & \Omega I_{zz} \\ cd_c & 0 & -\Omega I_{zz} & cd_c^2 + \Omega\tilde{I}\sin(2\Omega t) \end{bmatrix} \begin{bmatrix} \dot{x} \\ \dot{y} \\ \dot{\theta} \\ \dot{\phi} \end{bmatrix} \\
& + \begin{bmatrix} k & 0 & 0 & kd_k \\ 0 & k & -kd_k & 0 \\ 0 & -kd_k & kd_k^2 & 0 \\ kd_k & 0 & 0 & kd_k^2 \end{bmatrix} \begin{bmatrix} x \\ y \\ \theta \\ \phi \end{bmatrix} = \begin{bmatrix} -U_s\Omega^2\sin(\Omega t) \\ U_s\Omega^2\cos(\Omega t) \\ U_d\Omega^2\cos(\Omega t) \\ U_d\Omega^2\sin(\Omega t) \end{bmatrix}
\end{aligned} \tag{5.66}$$

The static and dynamic imbalances U_s and U_d , however, are unknown. This is where the unified model comes in, taking inputs from the empirical model to be able to solve the system.

5.3. Unified model

The purpose of the unified model is to combine the empirical and analytical models, which have been described above. The analytical model, on the right-hand side of the system (5.66), contains only the imbalance forces and hence only the fundamental harmonic. The goal is therefore to substitute those forces with the results of the empirical model, so that all harmonic orders h , as well as the system dynamics, can be simulated in a single (unified) model.

The amplitude coefficients C and harmonic orders h have been determined with the empirical model. These are the two parameters needed to model the output force (on the accelerometer), with a quadratic model of the form $C\Omega^2\sin(h\Omega t)$ which has been shown in section 5.1. However, the amplitudes obtained through this model do not correspond exactly to the ones of the input forces on the right-hand side of the analytical model. The former are the forces/torques that take into account the amplification of the imbalance forces by the mounting bracket, while the latter are the (centrifugal) imbalance forces/torques at the source, generated by the fans, and are therefore much smaller.

The amplification factor that exists between the two disturbances (which will be indicated as F_{out} , at the accelerometer, and F_{in} , at the source) is called transmissibility and is a function of the damping ratio of the mounting bracket ξ , the fan speed Ω in Hz (i.e. rps), and the natural frequency of the corresponding mode, either ω_t (translational) or ω_r , rocking (it will be written as a general ω_n below). The transmissibility can be written as ([10, p. 94]):

$$T(\xi, \Omega, \omega_n(\Omega)) = \left| \frac{F_{out}}{F_{in}} \right| = \sqrt{\frac{1 + 4\xi^2 \left(\frac{\Omega}{\omega_n(\Omega)} \right)^2}{\left(1 - \left(\frac{\Omega}{\omega_n(\Omega)} \right)^2 \right)^2 + 4\xi^2 \left(\frac{\Omega}{\omega_n(\Omega)} \right)^2}} \tag{5.67}$$

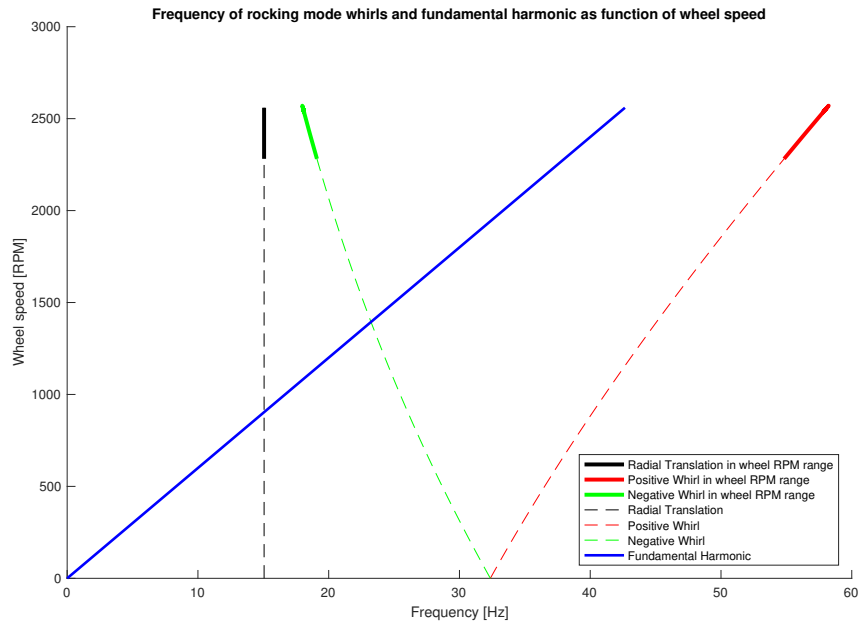
The damping ratio ξ , in this case, is assumed to be 0.002, a value that is typical of metallic materials (like the iron bars in the mounting bracket) and can also be found in literature [20].

Note that while ω_t is a constant, ω_r is speed-dependent, and can be approximated through the following relation ([27, p. 115]):

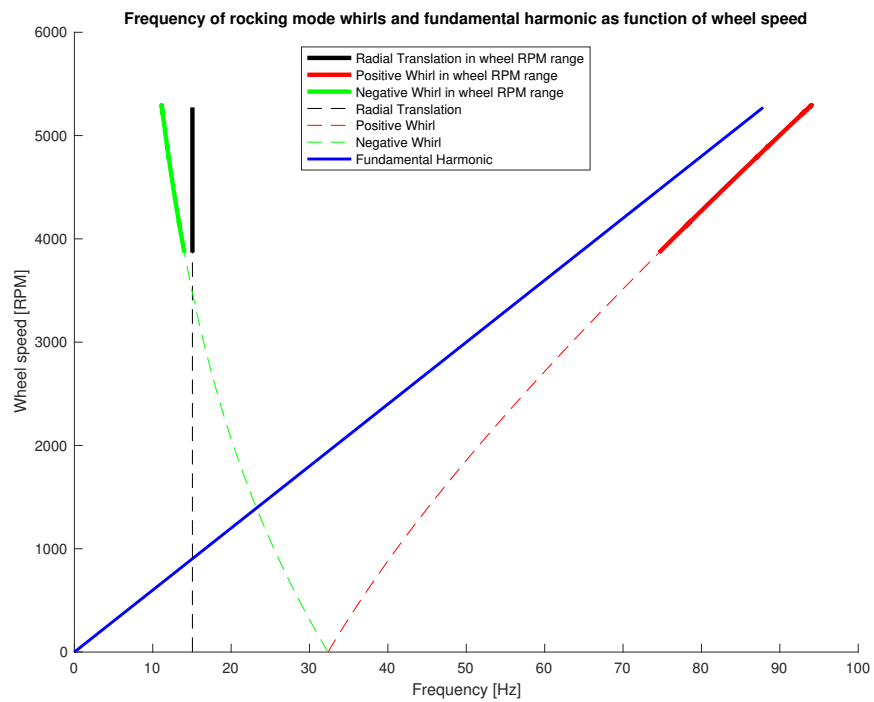
$$\omega_r \approx \mp \frac{\Omega I_{zz}}{I_{xx} + I_{yy}} + \sqrt{\left(\frac{\Omega I_{zz}}{I_{xx} + I_{yy}} \right)^2 + \frac{2kd_k^2}{I_{xx} + I_{yy}}} \quad (5.68)$$

The exact analytical solution of $\omega_r(\Omega)$ would contain I_{rr} instead of $\frac{I_{xx}+I_{yy}}{2}$, but since the setup is not symmetric with respect to the x and y axes, the radial inertia I_{rr} cannot be used. Instead, an average of the radial inertias I_{xx} and I_{yy} was used, so that the rocking frequency can be approximated.

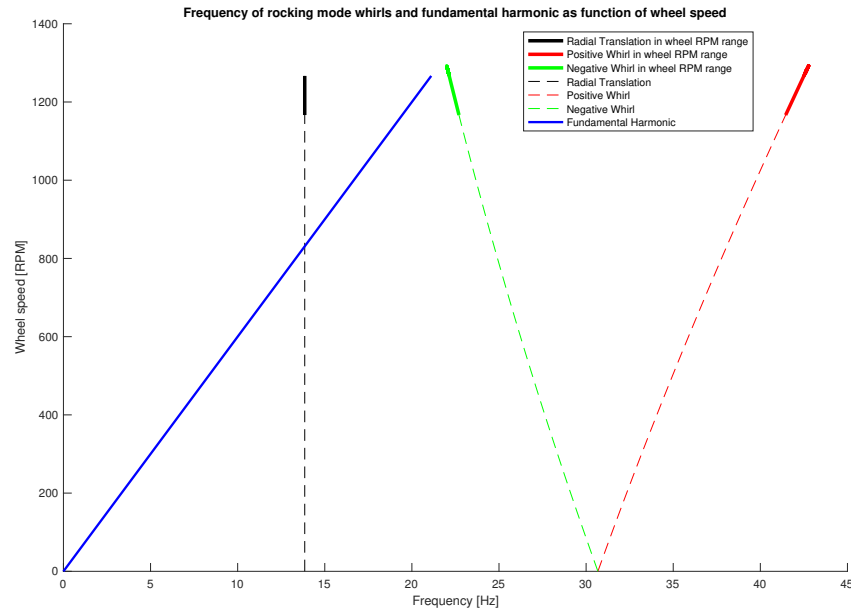
The \mp symbol denotes the fact that the rocking frequencies are two separate modes: the negative and positive whirls. Only one of these two modes is selected in the script to calculate transmissibility, depending on which mode is most excited in the speed range of interest. To understand which mode should be chosen for each fan, the translational and rocking modes are plotted together with the fundamental harmonic ($h = 1$), that is the straight line $\Omega = \omega$, where Ω are the wheel speeds in rps (Hz) in the y axis, and ω the frequencies in the x axis [Figure 5.15].



(a) Modes of the PiFan bracket (3.3V)



(b) Modes of the PiFan bracket (5V)

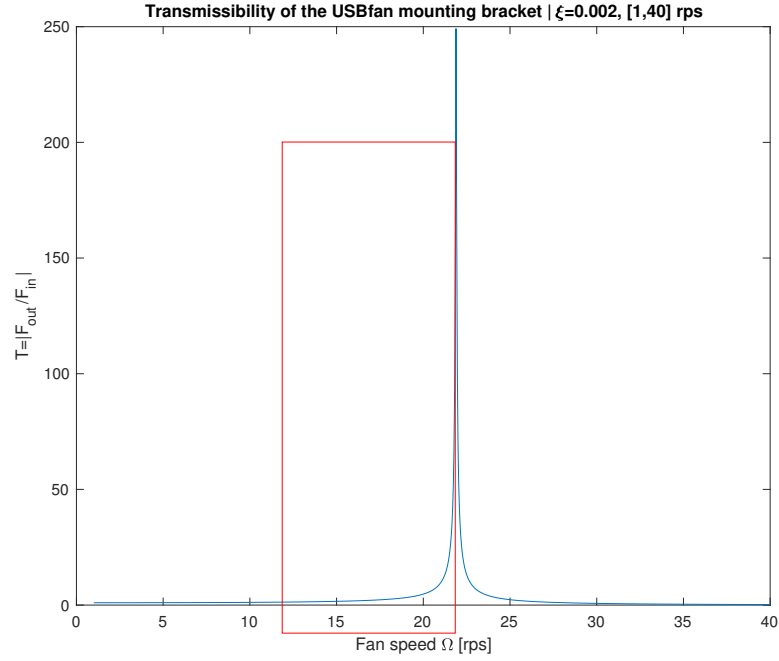


(c) Modes of the USB bracket

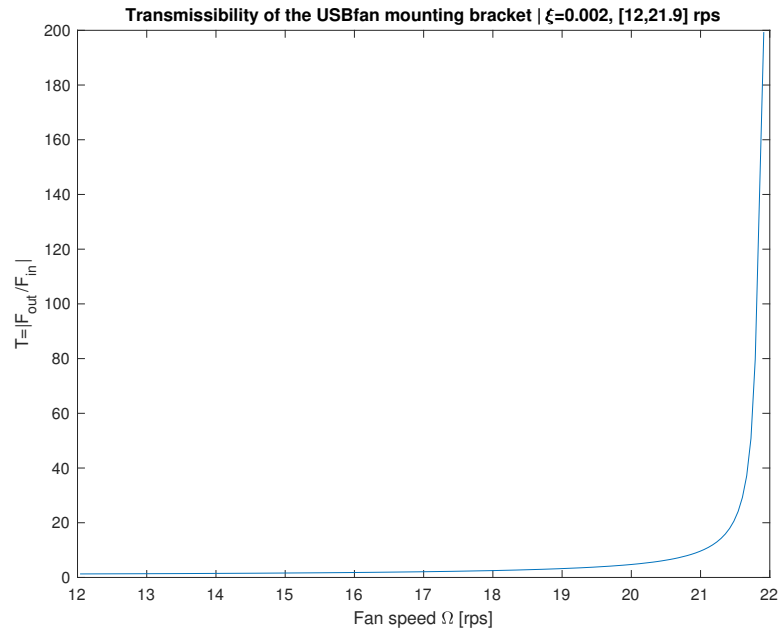
Figure 5.15: Vibrating modes of the mounting brackets and fundamental harmonic

It can be noticed from the mode plots that, in the case of the PiFan bracket at 5V and 3.3V, the fan speed (blue line) only approaches the positive whirl mode (red line). Therefore this mode will be used to calculate transmissibility for the PiFan bracket at each step (as a function of speed). In the case of the USB fan mounting bracket, instead, the fundamental harmonic approaches the negative whirl mode, so this will be used in the calculation of transmissibility. In the following equations of the model, for simplicity, this mode will be generally indicated as ω_r , the rocking mode, although it should be remembered that different whirls are used in the calculation for the two fans.

An example of the transmissibility function for the mounting bracket with the USB fan mounted on top is shown in figure 5.16.



(a) Transmissibility in the [1,40] rps speed range



(b) Transmissibility in the fan speed range

Figure 5.16: Example of transmissibility function of the USB mounting bracket

The figure on the top shows the transmissibility amplitude over a [1,40] rps speed range. A transmissibility function usually equals 1 for forcing frequencies (speeds in this case) lower than the natural frequency of the system (at the left of the peak). Then, as the speed increases, there is an amplification region, followed by an isolation region, where the amplitude of the outer force is lower than that of the input force. The mounting brackets built for this project are such that the speeds of the two fans partly take advantage of this amplification region so that vibrations are amplified at the output (accelerometer). The USB fan speed, for example, covers only the speed range in the figure on the bottom during tests, which is a zoom of the red

rectangle in the top figure. Therefore, an amplification of disturbances of 200 times occurs at around 21.9Hz , where the fan speed approaches the resonance zone of the bracket negative whirl mode, as shown in figure 5.15c.

Finally, as equation 5.67 suggests, the empirical model forces F_{out} will have to be divided by the transmissibility function to get the source forces F_{in} . The right-hand sides of the system therefore become:

$$\begin{bmatrix} -U_s \Omega^2 \sin(\Omega t) \\ U_s \Omega^2 \cos(\Omega t) \\ U_d \Omega^2 \cos(\Omega t) \\ U_d \Omega^2 \sin(\Omega t) \end{bmatrix} \rightarrow \frac{1}{T(\xi, \Omega, \omega_r)} \begin{bmatrix} -\sum_{k=1}^{n_h} C_{x_k} \Omega^2 \sin(h_{x_k} \Omega t) \\ \sum_{k=1}^{n_h} C_{y_k} \Omega^2 \cos(h_{y_k} \Omega t) \\ \sum_{k=1}^{n_h} C_{\theta_k} \Omega^2 \cos(h_{\theta_k} \Omega t) \\ \sum_{k=1}^{n_h} C_{\phi_k} \Omega^2 \sin(h_{\phi_k} \Omega t) \end{bmatrix} \quad (5.69)$$

And the full unified model, then, becomes:

$$\begin{bmatrix} M_t & 0 & 0 & 0 \\ 0 & M_t & 0 & 0 \\ 0 & 0 & I_{xx} & \frac{1}{2} \tilde{I} \sin(2\Omega t) \\ 0 & 0 & \frac{1}{2} \tilde{I} \sin(2\Omega t) & I_{yy} \end{bmatrix} \begin{bmatrix} \ddot{x} \\ \ddot{y} \\ \ddot{\theta} \\ \ddot{\phi} \end{bmatrix} + \begin{bmatrix} c & 0 & 0 & cd_c \\ 0 & c & -cd_c & 0 \\ 0 & -cd_c & cd_c^2 - \Omega \tilde{I} \sin(2\Omega t) & \Omega I_{zz} \\ cd_c & 0 & -\Omega I_{zz} & cd_c^2 + \Omega \tilde{I} \sin(2\Omega t) \end{bmatrix} \begin{bmatrix} \dot{x} \\ \dot{y} \\ \dot{\theta} \\ \dot{\phi} \end{bmatrix} + \begin{bmatrix} k & 0 & 0 & kd_k \\ 0 & k & -kd_k & 0 \\ 0 & -kd_k & kd_k^2 & 0 \\ kd_k & 0 & 0 & kd_k^2 \end{bmatrix} \begin{bmatrix} x \\ y \\ \theta \\ \phi \end{bmatrix} = \frac{1}{T(\xi, \Omega, \omega_r)} \begin{bmatrix} -\sum_{k=1}^{n_h} C_{x_k} \Omega^2 \sin(h_{x_k} \Omega t) \\ \sum_{k=1}^{n_h} C_{y_k} \Omega^2 \cos(h_{y_k} \Omega t) \\ \sum_{k=1}^{n_h} C_{\theta_k} \Omega^2 \cos(h_{\theta_k} \Omega t) \\ \sum_{k=1}^{n_h} C_{\phi_k} \Omega^2 \sin(h_{\phi_k} \Omega t) \end{bmatrix} \quad (5.70)$$

5.3.1. Numerical solution of the unified model

The goal of this procedure is to convert the equations 5.70 into an equivalent first-order differential equation system, which can be easily solved with an `ode` method, for example in MATLAB.

The system will be of the following form:

$$M(t, q) \ddot{\vec{q}} = \vec{f}(t, q) \quad (5.71)$$

Where M is the so-called mass matrix and \vec{f} a vector containing elastic, dissipative, and external forces.

To do this, first, a new set of generalized coordinates is defined:

$$\vec{q} = \begin{bmatrix} q_1 & q_2 & q_3 & q_4 & q_5 & q_6 & q_7 & q_8 \end{bmatrix}^T = \begin{bmatrix} x & \dot{x} & y & \dot{y} & \theta & \dot{\theta} & \phi & \dot{\phi} \end{bmatrix}^T \quad (5.72)$$

Then, these coordinates are substituted into 5.70 to obtain the first-order system:

$$\begin{bmatrix}
1 & 0 & 0 & 0 & 0 & 0 & 0 & 0 \\
0 & M_t & 0 & 0 & 0 & 0 & 0 & 0 \\
0 & 0 & 1 & 0 & 0 & 0 & 0 & 0 \\
0 & 0 & 0 & M_t & 0 & 0 & 0 & 0 \\
0 & 0 & 0 & 0 & 1 & 0 & 0 & 0 \\
0 & 0 & 0 & 0 & 0 & I_{xx} & 0 & \frac{1}{2} \tilde{I} \sin(2\Omega t) \\
0 & 0 & 0 & 0 & 0 & 0 & 1 & 0 \\
0 & 0 & 0 & 0 & 0 & \frac{1}{2} \tilde{I} \sin(2\Omega t) & 0 & I_{yy}
\end{bmatrix}
\begin{bmatrix}
\dot{q}_1 \\
\dot{q}_2 \\
\dot{q}_3 \\
\dot{q}_4 \\
\dot{q}_5 \\
\dot{q}_6 \\
\dot{q}_7 \\
\dot{q}_8
\end{bmatrix}
=
\begin{bmatrix}
q_2 \\
-cq_2 - cd_c q_8 - kq_1 - kd_k q_7 - \frac{1}{T(\xi, \Omega, \omega_r(\Omega))} \sum_{k=1}^{n_h} C_{x_k} \Omega^2 \sin(h_{x_k} \Omega t) \\
q_4 \\
-cq_4 + cd_c q_6 - kq_3 + kd_k q_5 + \frac{1}{T(\xi, \Omega, \omega_r(\Omega))} \sum_{k=1}^{n_h} C_{y_k} \Omega^2 \cos(h_{y_k} \Omega t) \\
q_6 \\
cd_c q_4 + (\Omega \tilde{I} \sin(2\Omega t) - cd_c^2) q_6 - \Omega I_{zz} q_8 + kd_k q_3 - kd_k^2 q_5 + \frac{1}{T(\xi, \Omega, \omega_r(\Omega))} \sum_{k=1}^{n_h} C_{\theta_k} \Omega^2 \cos(h_{\theta_k} \Omega t) \\
q_8 \\
-cd_c q_2 + \Omega I_{zz} q_6 - (cd_c^2 + \Omega \tilde{I} \sin(2\Omega t)) q_8 - kd_k q_1 - kd_k^2 q_7 + \frac{1}{T(\xi, \Omega, \omega_r(\Omega))} \sum_{k=1}^{n_h} C_{\phi_k} \Omega^2 \sin(h_{\phi_k} \Omega t)
\end{bmatrix} \quad (5.73)$$

In this case, the system is solved in MATLAB in the `unified_model.m` script. Note that the system can be solved when the wheel is in a steady-state condition, which means Ω has to be constant. To satisfy this condition, the wheel speed Ω is averaged over a time window, which is an arbitrarily small fraction of the time array of the tests so that the system can be locally treated as a quasi-steady-state one. The mass matrix is then calculated for every time window and the solutions are finally calculated with an `ode45` method. At the end of the loop, the initial conditions are updated with the values of the last solution, so that in the next step the `ode45` solver uses those initial conditions.

After the solutions are calculated, the corresponding forces and torques can be found with the following formulas:

$$F_x(t) = kq_1(t) \quad T_\theta(t) = kd_k^2 q_5(t) \quad (5.74)$$

$$F_y(t) = kq_3(t) \quad T_\phi(t) = kd_k^2 q_7(t) \quad (5.75)$$

These arrays are the first final results of the unified model and can be directly compared, in the form of waterfall plots or frequency/order-amplitude plots at a fixed wheel speed, to the corresponding test data and the empirical model to validate the model.

The second set of results includes the static and dynamic imbalances U_s and U_d , which can be calculated, as shown in equation 5.69, as an amplitude coefficient divided by the transmissibility T . Imbalances are, in fact, the amplitudes of the source disturbances F_{in} , which equal the amplitudes of the output disturbances F_{out} (i.e. the amplitude coefficients) divided by T . As T is speed-dependent, an array of transmissibilities is calculated in the loop, together with the solutions, for each averaged speed inside a window.

Arrays of static and dynamic imbalances are then calculated in the following way:

$$U_{sx} = \frac{\max(C_{Fx})}{T} \quad U_{d\theta} = \frac{\max(C_{T_\theta})}{T} \quad (5.76)$$

$$U_{sy} = \frac{\max(C_{Fy})}{T} \quad U_{d\phi} = \frac{\max(C_{T_\phi})}{T} \quad (5.77)$$

Where T is the transmissibility array, and the fraction is meant as an element-wise multiplication of the inverse of T and the constant $\max(C)$.

Note that only the maximum among all amplitude coefficients was selected. Theoretically, to calculate imbalances, the amplitude coefficient corresponding to the fundamental harmonic $h = 1$ should be selected since the imbalance disturbances happen at that order. However, not all tests showed clearly a disturbance as $h = 1$, and hence the order 1 was not even identified in some cases by the empirical model.

Therefore, it was chosen to simply select the greatest amplitude coefficients (greatest disturbances) and assume that they are due to imbalances. These imbalances are thus calculated in the worst-case scenario.

The final values of the imbalances were calculated as an average of the means of the static/dynamic imbalance arrays:

$$U_s = \frac{\overline{U_{sx}} + \overline{U_{sy}}}{2} \quad (5.78)$$

$$U_d = \frac{\overline{U_{d\theta}} + \overline{U_{d\phi}}}{2} \quad (5.79)$$

where $\overline{U_{sx}}$, $\overline{U_{sy}}$, $\overline{U_{d\theta}}$ and $\overline{U_{d\phi}}$ are the mean of each imbalance array.

The static and dynamic imbalances calculated by the script are summarized in the table below:

Fan name	Static imbalance U_s	Dynamic imbalance U_d
USBfan	24.188gmm	154.753gmm ²
PiFan 3.3V	10.694gmm	27.564gmm ²
PiFan 5V	1.244gmm	2.273gmm ²

Table 5.4: Static and dynamic imbalance values calculated by the `unified_model.m` script

An example of the output plots of the unified model is shown below. The rest of the results is shown in Appendix B.

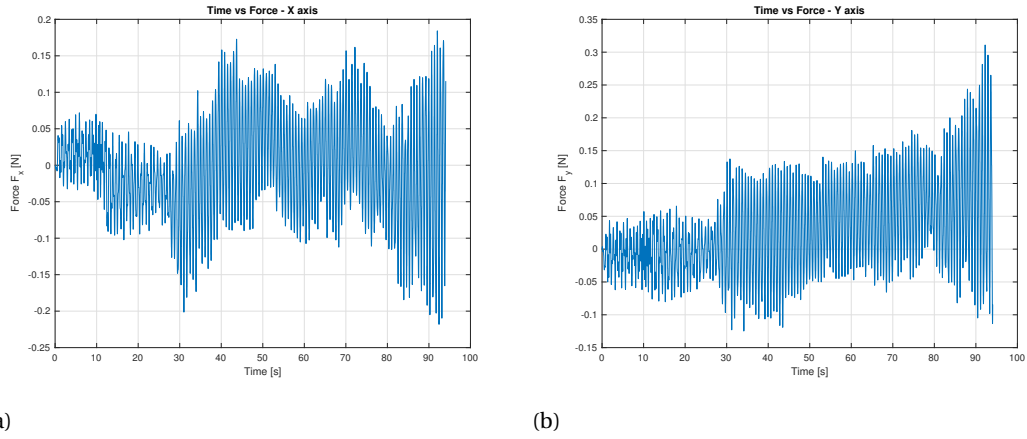


Figure 5.17: Unified model results: Force-time plots of the PiFan 5V mounting bracket

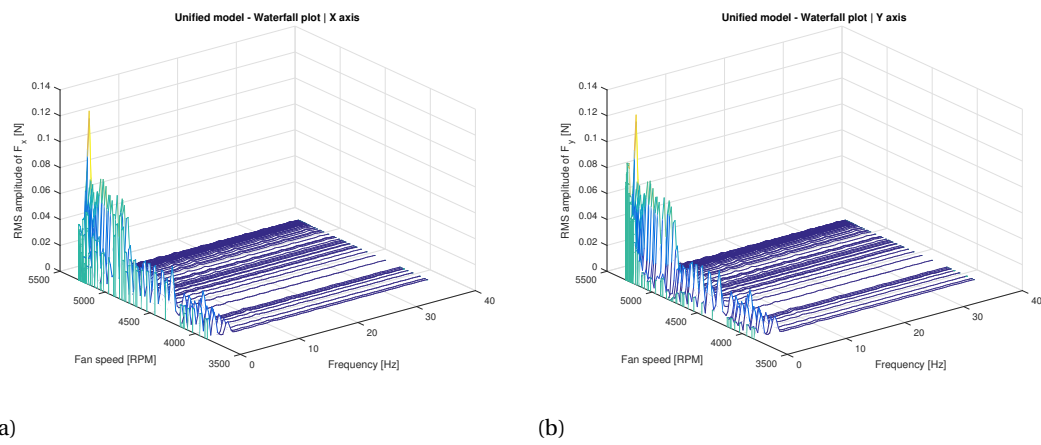


Figure 5.18: Unified model results: Waterfall Force plots of the PiFan 5V mounting bracket

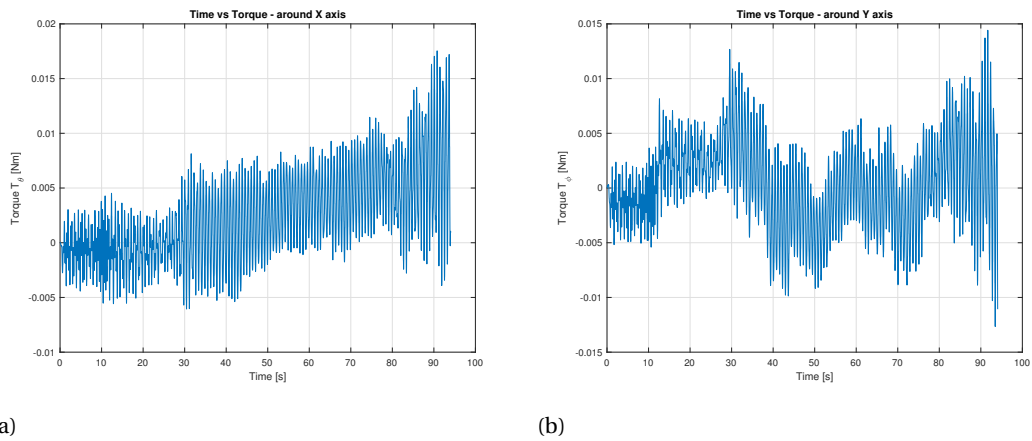


Figure 5.19: Unified model results: Torque-time plots of the PiFan 5V mounting bracket

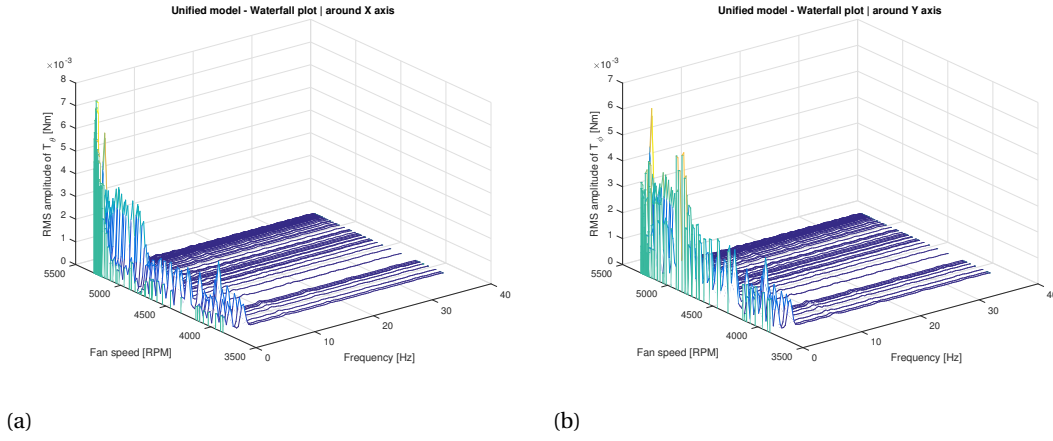


Figure 5.20: Unified model results: Waterfall Torque plots of the PiFan 5V mounting bracket

It can be noticed that the results of the unified model show amplitudes that are very similar to the test data, at A.0.4. However, a major drawback of the unified model appears to be that it cannot reproduce frequencies correctly, although they had been correctly approximated by the empirical model. Therefore, it was decided to compare this model to the test data at different frequencies, where analogous disturbance ridges are present. This is done at least to validate the measurement system for amplitudes, although frequencies cannot be validated.

A further discussion of the model, including a comparison to experimental data and the other models, will be given in the validation chapter (6).

5.3.2. Parameter definition

Many input parameters have been used in the analytical and unified model. For some of them, it has already been explained how they were calculated. Two important parameters whose source was not discussed in detail are the radial stiffness of the system k and the imaginary distance between springs and center of mass of the system d_k .

The radial stiffness was simply calculated inversely from the definition of the translational mode, calculated by a frequency case in CATIA, as explained in the next paragraph.

$$k = \omega_t^2 M \quad (5.80)$$

The distance d_k , instead, was calculated inversely from equation 5.68 of the rocking modes. It can be noticed that the equation in zero becomes:

$$\omega_{r0} = \sqrt{\frac{2kd_k^2}{I_{xx} + I_{yy}}} \quad (5.81)$$

From which d_k can be calculated as:

$$d_k = \omega_{r0} \sqrt{\frac{I_{xx} + I_{yy}}{2k}} \quad (5.82)$$

Where ω_{r0} is the rocking mode calculated by CATIA.

Furthermore, the damping coefficient of the system c was inversely calculated from the definition of damping ratio (ξ), which was taken from literature [20]:

$$c = 2M\omega_t\xi \quad (5.83)$$

Lastly, while the static and dynamic imbalance masses m_s and m_d were assumed as $1mg$ ($1e-6$) in the first iteration of the unified model, they have been recalculated in the following iterations, from the output static and dynamic imbalances 5.78 and 5.79:

$$m_s = \frac{U_s}{r_s} \quad (5.84)$$

$$m_d = \frac{U_d}{2r_d h_d} \quad (5.85)$$

The table below summarizes where parameters of the analytical and unified models were taken from. In case they were calculated with a specific equation, a link to that equation is reported on the right.

Parameter	Description	Source	Equation
M	Mass of fan + mounting bracket top base + iron bars	CATIA (5.7)	-
R	Fan radius	Measurement with a caliper	-
I_{xx}	Moment of inertia around x	CATIA (5.7)	-
I_{yy}	Moment of inertia around y	CATIA (5.7)	-
I_{zz}	Moment of inertia around z	CATIA (5.7)	-
r_s	Static imbalance mass radius	Assumption	R
r_d	Dynamic imbalance mass radius	Assumption	R
h_d	Dynamic imbalance mass axial distance	Assumption from measured fan height (h_f)	$\frac{h_f}{2}$
k	Radial stiffness of the system	Calculated	(5.80)
ξ	Damping ratio of the system	Assumption from literature [20]	0.002
c	Damping coefficient of the system	Calculation	(5.83)
d_k	Distance from system C.o.G. to springs	Calculation	(5.82)
d_c	Distance from system C.o.G. to dashpots	Assumption	d_k
m_s	Static imbalance mass	Assumption in first iteration, calculation later	(5.84)
m_d	Dynamic imbalance mass	Assumption in first iteration, calculation later	(5.85)
ω_t	Translational mode of the system	CATIA (5.6)	-
ω_{r0}	Rocking mode of the system	CATIA (5.6)	-
T	Transmissibility function	Calculation	(5.67)
h_k	Harmonic numbers	Empirical model	-
C_k	Amplitude coefficients	Empirical model	-

Table 5.5: Analytical and unified models: Parameter definition and origin

Notice that I_{xx} , I_{yy} and I_{zz} are the principal moments of inertia, which means they are the diagonal of the inertia tensor centered at the body (fan + mounting bracket top base + iron bars) center of mass. The extra-diagonal terms, in this case, are null.

Also, masses were taken from CATIA. It was realized only after the experimental part, that a measurement of masses with an electronic scale would have given more accurate values (especially for the fan), and therefore it is suggested in case of further experiments in the future.

Lastly, some parameters not listed in the table above have been used in the unified model. Recall that these all come from equations 5.59.

5.3.3. CAD model

A CAD model in CATIA was built to determine the translational and rocking modes of the mounting brackets, with PiFan and USB fan on top respectively. To do this, first, a static case was created in the Generative Structural Analysis workbench. The restraints are four clamps at the base of the iron bars. The loads are the gravitational acceleration and an imposed rotational acceleration of the fan around its axis – until 6000RPM for the PiFan (5V case) and 1250RPM for the USB fan.

Then, a frequency case was created, where connections (e.g. rigid, sliding, seam welding...) between the previously created meshes needed to be specified again (besides the geometry constraints) for the model to be computed correctly. The figures below show the computed modes. Rotational and translational modes can clearly be distinguished in the animations.

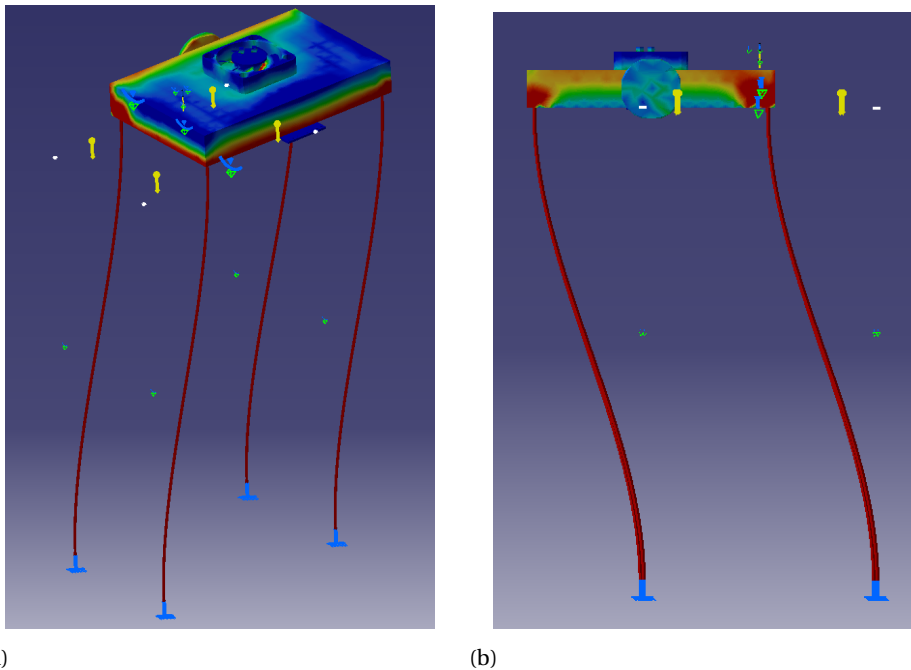


Figure 5.21: Translational mode of the PiFan mounting bracket (15.06Hz)

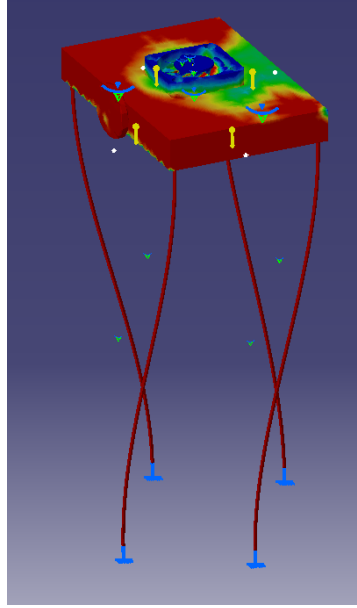
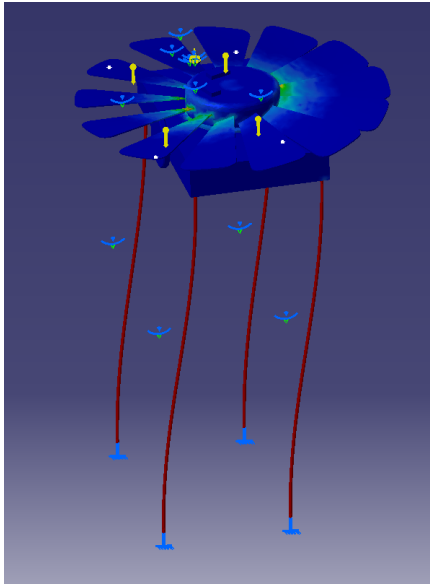
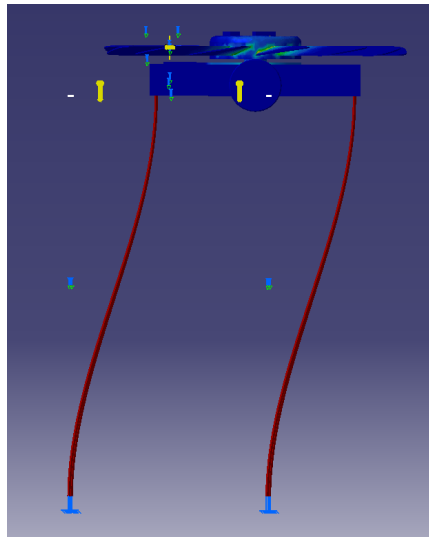


Figure 5.22: Rocking mode of the PiFan mounting bracket (32.36Hz)



(a)



(b)

Figure 5.23: Translational mode of the USBfan mounting bracket (13.85Hz)

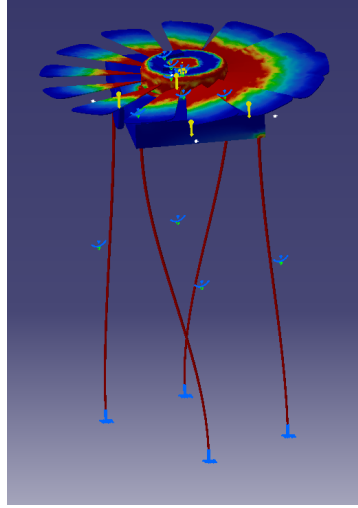


Figure 5.24: Rocking mode of the USBfan mounting bracket (30.68Hz)

The translational (ω_t) and rocking (ω_{r0}) modes of the mounting brackets with the two fans are:

	PiFan	USBfan
ω_t	15.06Hz	13.85Hz
ω_{r0}	32.36Hz	30.68Hz

Table 5.6: Translational and rocking modes calculated by CATIA for the mounting bracket and fan systems

These are the main inputs from CATIA to the unified model, together with masses and moments of inertia, which are reported below.

	PiFan bracket	USBfan bracket
M	0.208kg	0.244kg
I_{xx}	$3.502e-4 \text{ kgm}^2$	$3.715e-4 \text{ kgm}^2$
I_{yy}	$2.556e-4 \text{ kgm}^2$	$2.767-4 \text{ kgm}^2$
I_{zz}	$2.846e-4 \text{ kgm}^2$	$3.125-4 \text{ kgm}^2$

Table 5.7: System masses and principal moments of inertia calculated by CATIA

These values correspond to the system formed by the fan, the top base of the mounting bracket, and the iron bars.

Furthermore, there was also an attempt to create a Harmonic Dynamic Response case of the same models in CATIA, which is a union of the static and frequency cases, and returns plots of position, velocity, and acceleration in the frequency domain. The data were imported in MATLAB by the `CATIA_HDRplots.m` script. The position was multiplied by the radial stiffness of the system, like in the unified model, to obtain F_x and F_y , which could be compared to other models and tests. However, their amplitudes differed from all other

models and data by a least two orders of magnitude. Therefore, these could not be used for comparison. The results are shown below for reference.

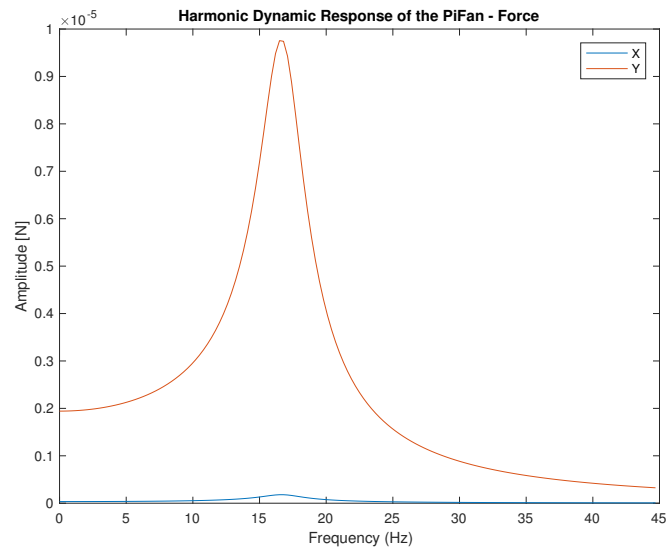


Figure 5.25: CATIA's Harmonic Dynamic Response results - PiFan bracket

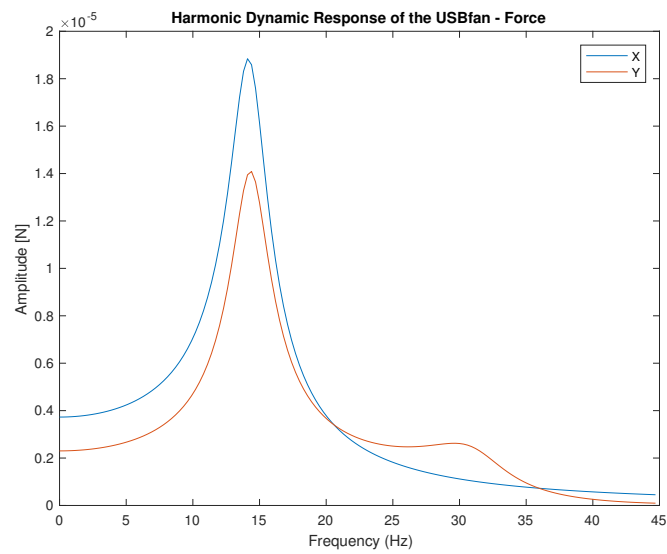


Figure 5.26: CATIA's Harmonic Dynamic Response results - USBfan bracket

5.4. Laser displacement model

In this section, a model of the displacement of the laser projection will be explained. As mentioned in chapter 4, a laser was projected onto a mirror fixed on the top base of the mounting brackets. The laser was then mirrored onto a black surface on a wall and this projected red dot was filmed with a Redmi Note 8 Pro (smartphone) camera in slow-motion at 920fps. The displacement in the videos is proportional to the displacement of the top base of the mounting bracket, which is the same as the accelerometer. Therefore, after multiplying this displacement by the mounting bracket stiffness, the force at the top base is directly comparable to the test data and the results of the other models. The downside of this approach is that, as opposed to the accelerometer, one laser projection corresponds to the displacement in just one direction. Therefore, more lasers would be needed to measure all directions.

With the knowledge of the test setup geometry and some camera sensor data, the real displacement at the top base can be found. The model is exemplified in figure 5.27, where the accelerometer reference frame is used.

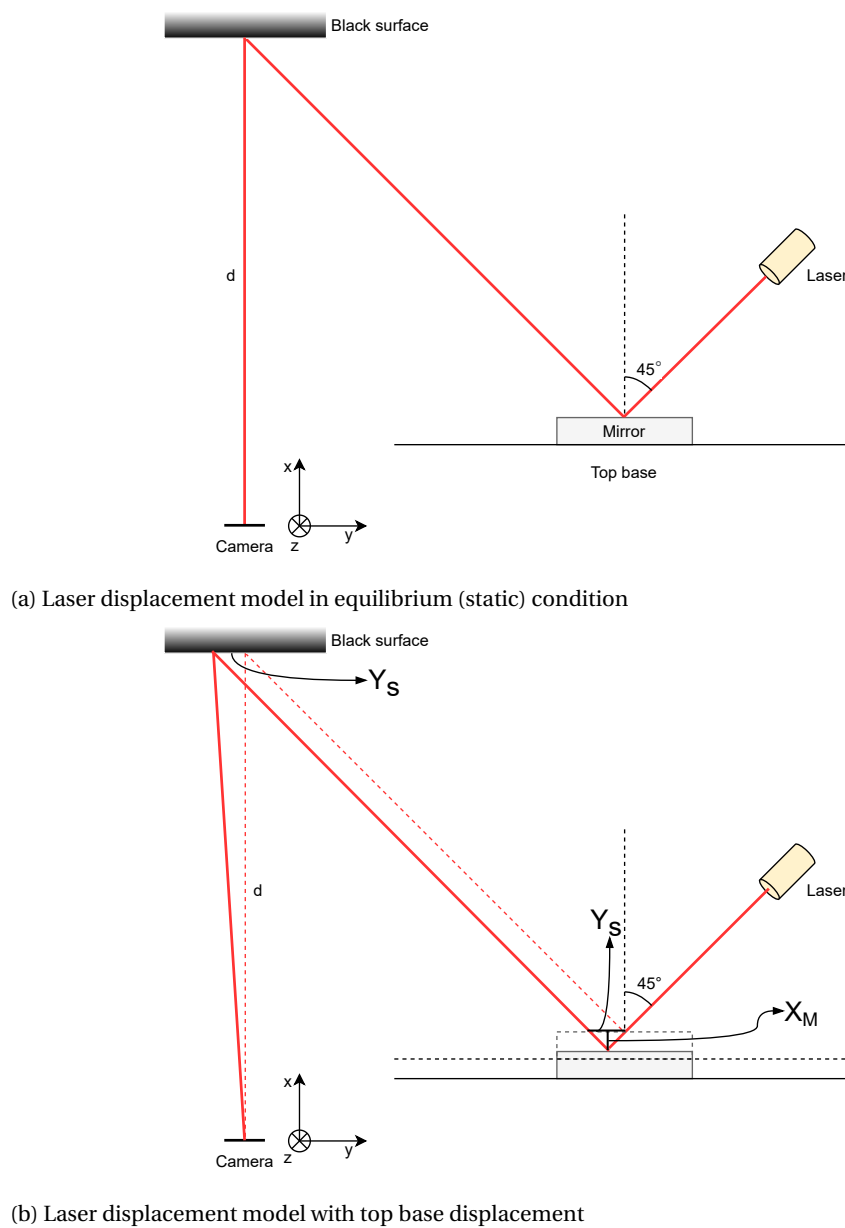


Figure 5.27: Laser displacement model

Figure 5.27a shows the test setup as seen from above in a static condition when the fan is not rotating and hence the top base is not moving. The laser was placed such that the angle of incidence is 45° and the distance between the camera and the black surface was measured ($d = 722\text{mm}$).

Figure 5.27b shows what happens during tests when the top base moves. As the top base and the mirror move down (in the direction -x), the laser impacts the mirror in a different position. The displacement of the mirror in the x direction is called X_M . This determines a displacement Y_S of the laser reflection on the black surface (in the direction -y), which is proportional to X_M . Note that a movement of the top base in the y direction doesn't determine a displacement of the laser reflection, as the laser will hit the mirror at the same point (in a ground-fixed frame). It is easy to see that the following relation exists between X_M and Y_S :

$$\tan \alpha_i = \frac{X_M}{Y_S/2} \quad (5.86)$$

Where α_i is the angle of incidence.

This is true because the triangle formed by the incident and reflected rays and Y_S in figure 5.27b is always an isosceles triangle, for the law of reflection, so the height X_M splits the base of this triangle exactly in half ($Y_S/2$). Therefore, looking at the trigonometry of one of the two right triangles which are visible inside the isosceles triangle, the relation above can be determined. In this case, α_i is 45° , so its tangent equals 1. The relation then becomes:

$$Y_S = 2X_M \quad (5.87)$$

So, the displacement in the y direction on the black surface is equal to twice the displacement of the top base in the x direction, with the same sign. Therefore, the rest of the model is a matter of determining the real displacement on the black surface Y_S , starting from the video clips.

To be able to do this, the size of a pixel in mm on the object plane (black surface) was found. In this case, the radius of the laser dot was used for the conversion from pixel to mm in order to determine the displacement in mm. The problem, therefore, became how to determine the real laser radius on the object plane and the displacement of the laser in time.

This required an object recognition script, which was largely taken by the open-source OpenCV (Python) script by A. Rosebrock [45][46] and adjusted for this purpose with minor changes.

The goal of this script is to detect an object in a video (which can be input with the `--video` or `-v` option from the command line) by its color and track it across video frames by drawing its previous positions, like a trail, whose length is decided according to a buffer parameter (`--buffer` or `-b` option) input by the user. The script was adjusted by changing the object color to the range of red HSV values represented by the laser dot center and contours. Additionally, the coordinates of the laser dot and its radius, which are normally used to draw the trail and a contour around the object, were saved to a `.txt` file, so that they can be further elaborated.

The working principle of the script is to first recognize all parts of the video frame within the given color range. Of course, the background and preferably all other objects in the frame will have to be outside this range. In this case, there are no problems since the background is completely black and the laser dot is the only object in the frame. In order to correctly choose the color range needed for the purpose, the `range_detector.py` script of the `imutils` library can be used on a single frame of a laser displacement video. This script outputs on the terminal the HSV minimum and maximum values selected by the user on a track-bar and it creates a binary mask of the input image with the given range. Therefore, the exact color range of the laser dot can be determined (whenever the created mask looks satisfactory), as shown in figure 5.28, and can then be inserted into the `laser_tracking.py` script.

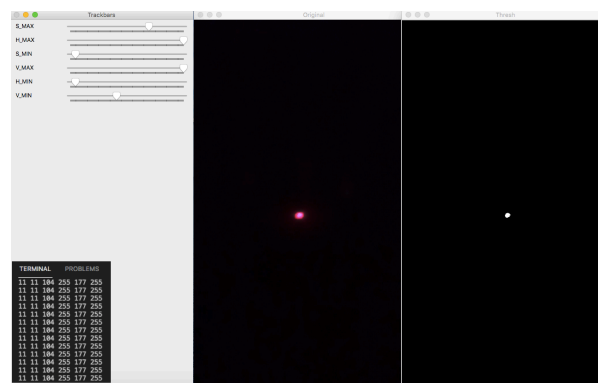


Figure 5.28: Example of usage of the `range_detector.py` script

The same principle for creating a mask is then used in the first part of the laser tracking script, with the in-built OpenCV function `cv2.inRange`. Then, also with in-built functions, it is possible to determine the contour of the mask, the minimum enclosing circle, the coordinates of the center, and the radius (in pixels). These last two parameters are saved as arrays in txt files and they are later read as input by the MATLAB file `laser_displacement.m`, where the post-processing occurs. A sample frame of the `laser_tracking.py` script during execution is shown in figure 5.29, with a yellow contour, a green trail, and the displacement of the center coordinates written in the bottom left corner.

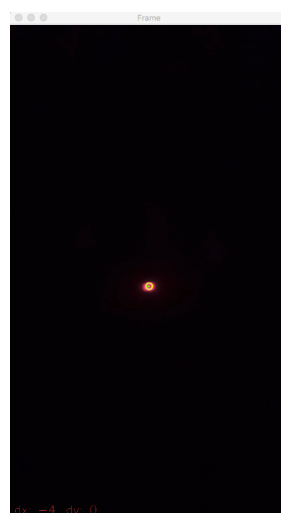


Figure 5.29: Sample output frame of the `laser_tracking.py` script

Notice that in the sample frame, the laser center has a displacement of -4 pixels. The maximum displacement amplitudes of all tests were, in fact, around 4 or 5 pixels. Therefore, a low resolution is expected in the results, with many steps. In other words, this is not an accurate testing method to capture the behavior of the fan in the frequency domain (also because usually a single harmonic is visible in the results), but just to get a taste of what the maximum disturbance amplitude will be. It could be, for example, a fast preliminary test (with little post-processing) to get a rough idea of how much imbalance a wheel has, or if it was reduced after addressing the issue.

After the laser radius in pixels is determined by the laser tracking script, some sensor data are needed to proceed with calculations: in particular, the focal length, sensor size (diagonal), and Aspect Ratio. The Redmi Note 8 Pro mounts a Samsung Isocell GW1 CMOS sensor, whose features can be found online [47], including sensor diagonal and Aspect Ratio. The focal length, instead, can be found in the Exif file of the images taken with the smartphone, which is usually included in the image properties. The needed parameters are summarized in table 5.8.

Name	Symbol	Value
Focal Length	f	5.43mm
Sensor diagonal	d_s	9.21mm
Aspect Ratio	AR	16:9

Table 5.8: Isocell GW1 Sensor data

First, with the sensor diagonal and Aspect Ratio it is possible to calculate the sensor height in mm.

$$d_s = \sqrt{W_{s\text{mm}}^2 + H_{s\text{mm}}^2} = H_{s\text{mm}} \sqrt{1 + \left(\frac{1}{AR}\right)^2} \quad (5.88)$$

Where $W_{s\text{mm}}$ and $H_{s\text{mm}}$ are respectively sensor width and height in mm.

$$H_{s\text{mm}} = \frac{d_s}{\sqrt{1 + \left(\frac{1}{AR}\right)^2}} \quad (5.89)$$

Then, by looking at a simplified object-sensor drawing, as represented in figure 5.30, some proportions can be derived.

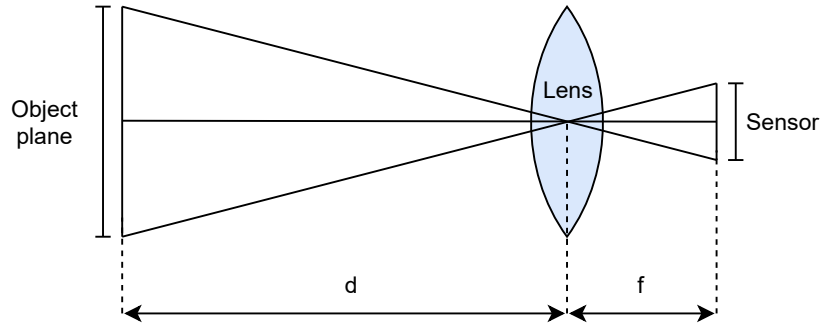


Figure 5.30: Lens optics math: sensor and object plane proportions

First of all, given the geometry of similar triangles formed on the left and on the right of the lens, the ratios of their bases and heights will be the same:

$$\frac{H_{s\text{mm}}}{f} = \frac{H_{O\text{mm}}}{d} \quad (5.90)$$

Where $H_{O\text{mm}}$ is the height of the object plane in mm (that is the real size of the video frame).

This holds true not only for the sizes of the whole sensor and object planes but also for the sizes of the same object on the sensor and object planes, where the latter is the true size of the object. So, for the laser dot it will be:

$$R_L = \frac{dR_{Ls\text{mm}}}{f} \quad (5.91)$$

Where $R_{Ls\text{mm}}$ is the radius of the laser in the sensor plane and R_L its true radius on the object plane. In some cases, the videos were taken with a zoom. Therefore R_L will need to be further divided by this zoom to obtain the real size of the laser radius on the object plane.

The size of the laser radius in the sensor plane $R_{Ls\text{mm}}$ can be found with a simple conversion of units from pixels, where $R_{L\text{px}}$ was found by the tracking script (and was later averaged in MATLAB to obtain a

single number). This is done through the known ratio of the sensor height in mm and pixels (1280), which is equal to the size of a pixel in the sensor plane in mm.

$$R_{Lsmm} = R_{Lpx} \frac{H_{smm}}{H_{spx}} \quad (5.92)$$

After inserting this value into equation 5.91, R_L can be determined. This will allow the final calculation needed to determine the displacement of the laser in mm, which is the pixel size in mm in the object plane:

$$px_{mm} = \frac{R_L}{R_{Lpx}} \quad (5.93)$$

Given the displacement found by the tracking script in pixels Y_{Spx} (i.e the array of the dot center coordinates), the corresponding array in mm is then:

$$Y_S = Y_{Spx} px_{mm} \quad (5.94)$$

And finally, through equation 5.87 the displacement of the top base can be found by dividing by 2. Then, similarly to the unified model, the displacement is multiplied by the mounting bracket stiffness, to obtain the force at the top base. This can be compared directly to the results of the other models for forces in the x direction.

Below only results for one of the laser tests are shown, namely the USB fan. Further results are present in appendix C and comparisons can be found in chapter 6.

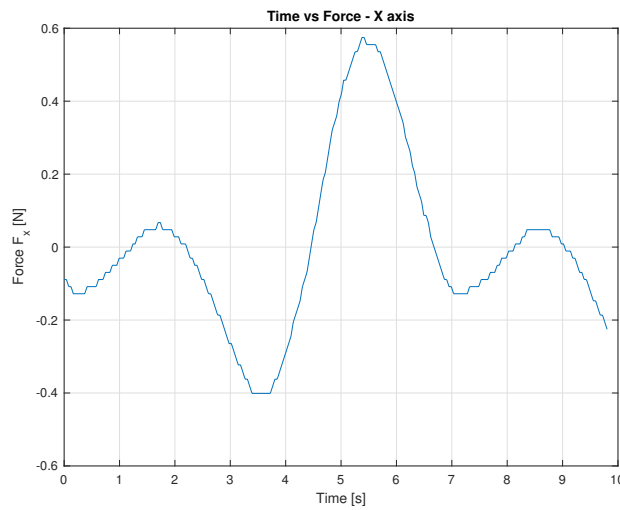


Figure 5.31: Time-Force plot of the USB fan laser displacement model

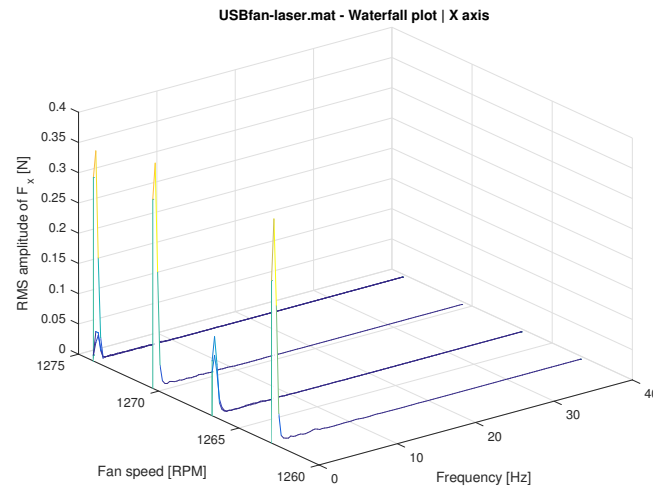


Figure 5.32: Waterfall plot of the USB fan laser displacement model

As expected, the treatment of the data in the frequency domain doesn't give much insight in this case, as it is clear from the Time-Force plot that the displacement shows just two harmonics (all other tests showed just one instead). The amplitudes, however, will be compared to those recorded by the accelerometer and the ones determined by other models, to verify whether they could be a first indicator of how much residual imbalance a wheel has.

A quick visual comparison of amplitudes can be done already at this stage, looking at figures 5.31, 4.9 from the test results, and B.6 from the unified model. In the laser tests, it can be seen that the amplitude reaches about $0.6N$. In the MPU6050 test results, instead, the major peak had an amplitude of about $0.1N$. The unified model, finally, shows a peak at about $0.35N$ for F_x . Therefore, it can already be understood that the results are generally a bit distant from each other and surely do not comply with the 30% error requirement. The main reasons for this may be: a bad approximation of the transmissibility function for the unified model, which could instead be measured empirically. Inexact values of transmissibility would cause an incorrect approximation of the external force in the equations of motion and therefore inaccurate solutions. A second reason could be the inaccuracy of the laser itself and of the image recognition script. The measurement of the laser displacement was based, in fact, on the estimation of the laser size, from pixels to mm. However, the pixels were not always clearly defined as the frames are in low definition and some laser dot contour pixels change from one frame to another. Furthermore, the zoom used in some recordings may have changed the actual focal length, and this would also change the calculations. As for the accelerometer tests, the main problems are related to the low-pass filter at $21Hz$ and the multiplication of speeds by a constant factor, as explained in chapter 4, which don't help in matching the results at the exact same frequencies and speeds with other types of tests.

Focusing just on the time-force plot of the laser model (5.31), the two identified harmonics (at about $0.6N$ and $0.05N$) may correspond to the ones at $10Hz$ and $21Hz$ which are also clearly visible in the test results (4.9). The bigger peak would be the fundamental harmonic 1, caused by static imbalance, and the smaller one 0.5. Rotating objects, in fact, often show harmonics which are multiples of a fundamental one, and as such, they are also called sub-harmonics. The frequencies in the waterfall plot don't match simply because the videos were taken at 920fps and the plots represent the time of the video, not the time of the real recorded tests, which would be much shorter and change the frequencies as well. Lastly, little local peaks can be seen throughout the time-force curve and even on top of the major peak. These are not actual disturbance peaks, but they are simply related to the low resolution of the videos. It can also be seen in the laser tracking script, that displacements change rapidly across only a few pixels, and the maximum displacement is equal to just 50 pixels, which causes all the steps present on the curve.

Validation of experimental data

In this chapter, all tests and corresponding models are going to be compared through RPM-peak amplitude plots, at specific frequencies. This is going to help fill a requirement verification matrix, shown in chapter 7, and summarize for which requirements of the initial matrix 2.5 the systems built in this project are compliant, partially compliant, or not compliant.

6.1. Identification of frequency ranges for comparison

It was mentioned in the previous chapter that the unified and laser tests/models didn't manage to capture frequencies correctly from the test data. For this reason, and due to the initial mistake of setting a digital low-pass filter at 21 Hz on the MPU6050, it can be concluded that frequencies cannot be validated, as they are certainly not reliable. For the same reason, the harmonic orders found by the empirical model cannot be validated, although the model appeared to identify them correctly. However, a similarity between the peaks of the unified model, laser tests, and MPU6050 test data was noticed at different frequencies. In other words, there was a frequency shift from the original ones of the accelerometer test to the ones in the unified and laser models, which had content only up to 3 Hz . Therefore, to at least check the difference between these peaks, it was decided to compare amplitudes at different frequency ranges.

The frequency ranges used for comparison are summarized in the table below:

	MPU6050 + Empirical model	Unified model	Laser test/model
PiFan 3.3V	$[20 - 25]\text{ Hz}$	$[0 - 3]\text{ Hz}$	$[0 - 2]\text{ Hz}$
PiFan 5V	$[26 - 32]\text{ Hz}$	$[0 - 2]\text{ Hz}$	$[0 - 2]\text{ Hz}$
USBfan	$[9 - 11]\text{ Hz}$	$[0 - 2]\text{ Hz}$	$[0 - 2]\text{ Hz}$

Table 6.1: Frequency ranges within which the maximum peaks are taken for comparison

The same frequency ranges were used for all 4 disturbances of the same tests/models, given that they all showed the greatest peaks in the same range.

The rationale for generating the comparison figures was to select all disturbances (from all tests and models) only at these frequency ranges and in their whole speed range. Then, at each speed, the maximum disturbance within the given range is selected (since within that range there is only one peak). The results are one-dimensional peak amplitude arrays over all wheel speeds. These are plotted by the script `final_comparison_plot.m`, as RPM-amplitude 2D plots. The results are shown in the sections below.

6.2. PiFan 3.3V tests and models comparison

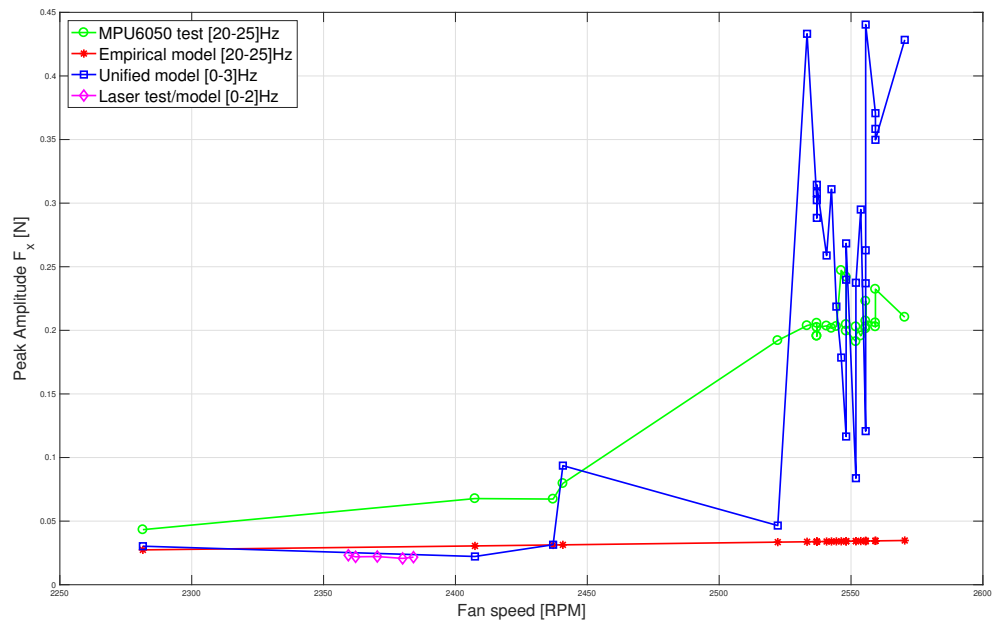


Figure 6.1: Comparison of all tests and models. PiFan 3.3V F_x data

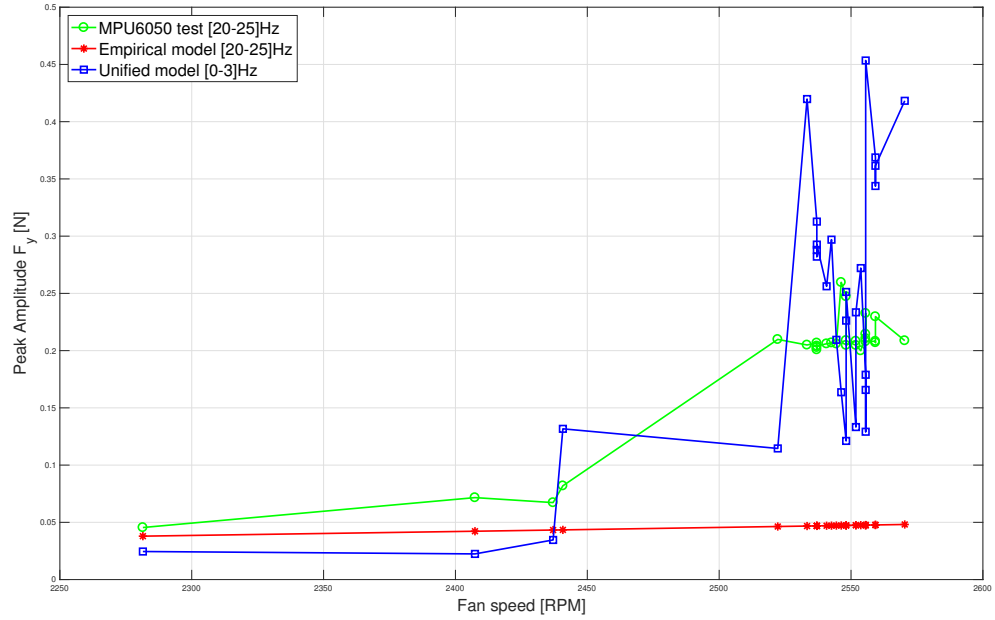
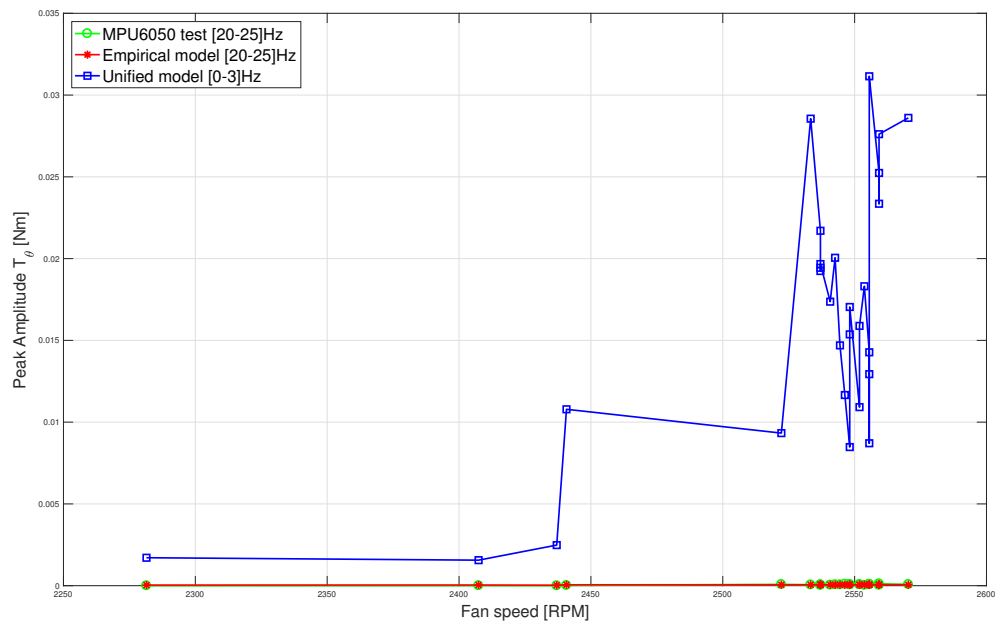
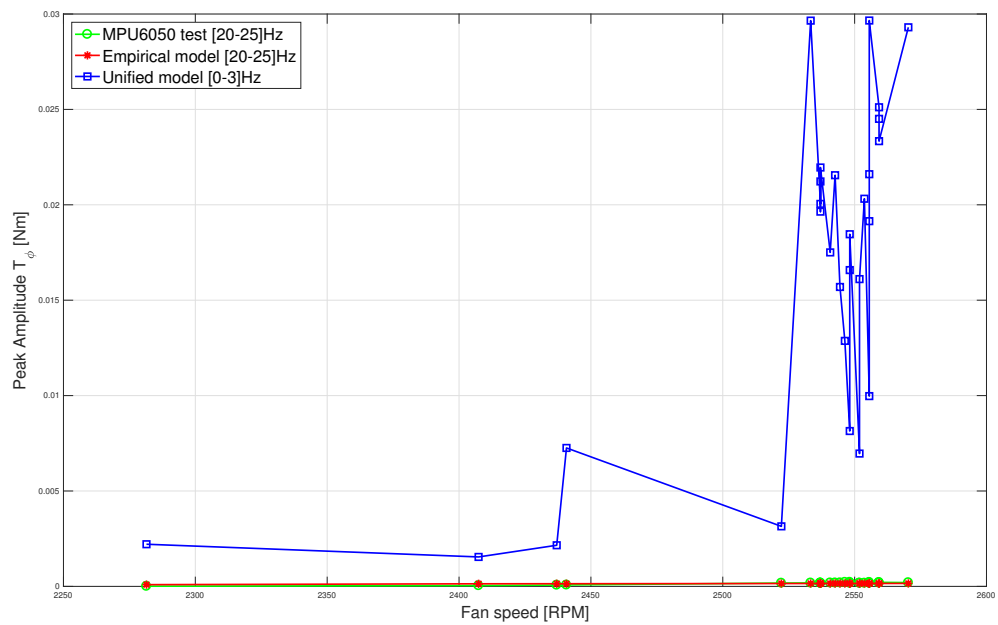


Figure 6.2: Comparison of all tests and models. PiFan 3.3V F_y data

Figure 6.3: Comparison of all tests and models. PiFan 3.3V T_θ dataFigure 6.4: Comparison of all tests and models. PiFan 3.3V T_ϕ data

It can be noticed from the plots above that, although the tests and models sometimes follow a similar pattern, there are big differences in amplitude at specific speeds. The unified model, in particular, generally overpredicts the MPU6050 test data, while the empirical model and the laser model underpredict them. For example, it can be seen in figure 6.1, that at 2535RPM the unified model amplitude is more than twice as great as the test data, while the empirical model amplitude is less than 4 times lower. Furthermore, it was mentioned that the speeds recorded during laser tests don't match those of the MPU6050 test, in the case of the PiFan at 3.3V and 5V, while they do for the USB fan. Therefore, it was decided to divide the speeds of the laser model by 1.35 to match the other data.

From all of this, it can be concluded already that the tests models can by no means comply with requirements TES-F-006 and MOD-F-003, asking for maximum errors of 30% at any given frequency and speed. Note also that the torque results are worse than the force ones, since the unified model severely overpredicts all other data, being up to 255 times greater than the test results in figure 6.3. This is probably caused by the fact that the starting data for torque were very noisy and thus they weren't a good input for the models. However, values of force below 0.0186mN and torque below 0.0034mNm (the range of the Delfi-PQ reaction wheel disturbance torque) were recorded by the MPU6050 (after the division of the raw data by transmissibility), even though with a high level of noise in most torque measurements. With some improvements it could be said that the MPU6050 is capable of reading at that range, so the sensor is partially compliant with requirements TES-F-003 and TES-F-004.

6.3. PiFan 5V tests and models comparison

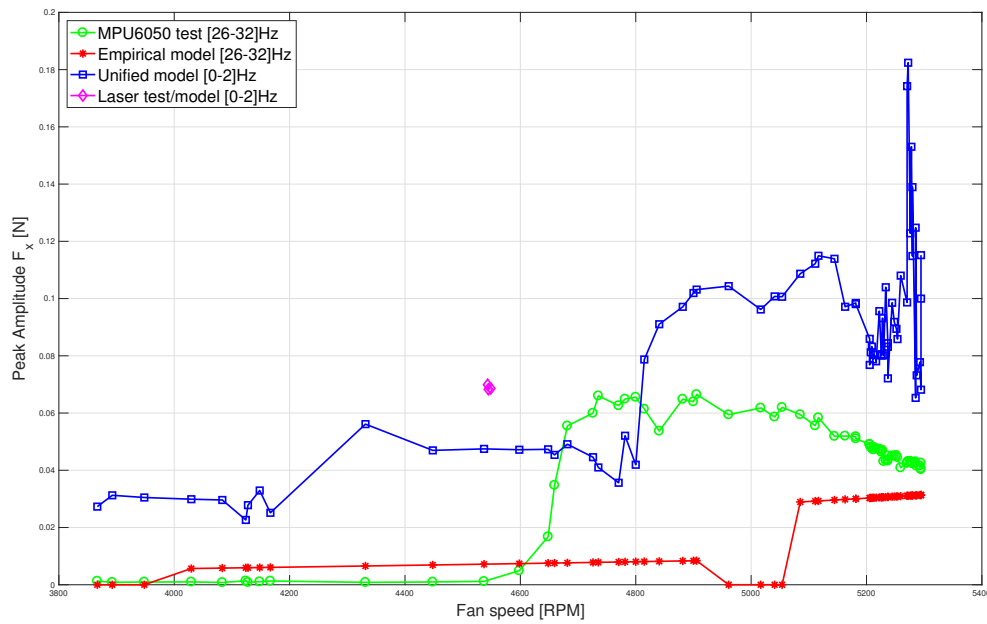
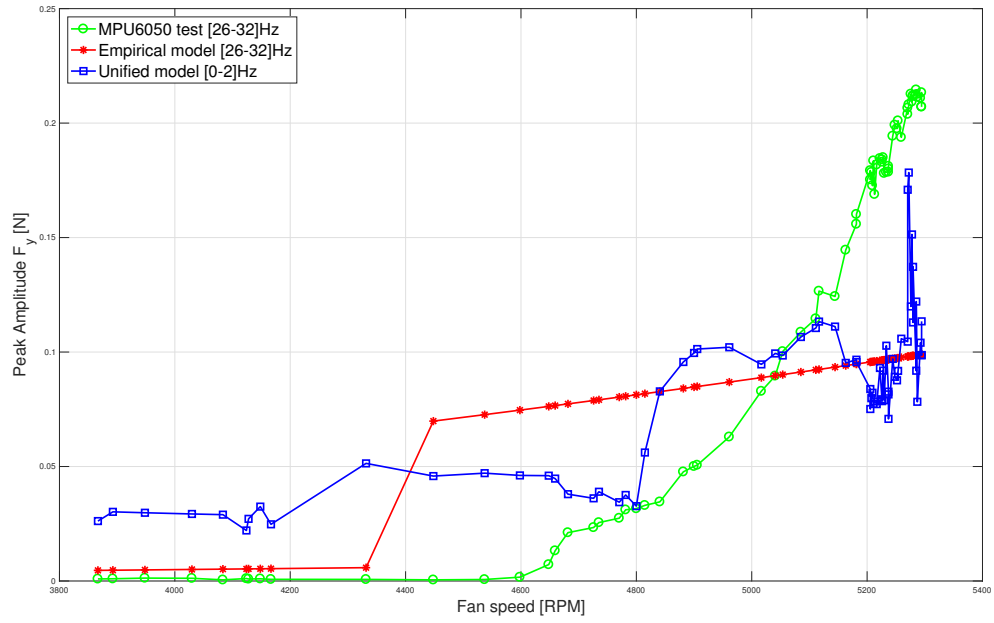
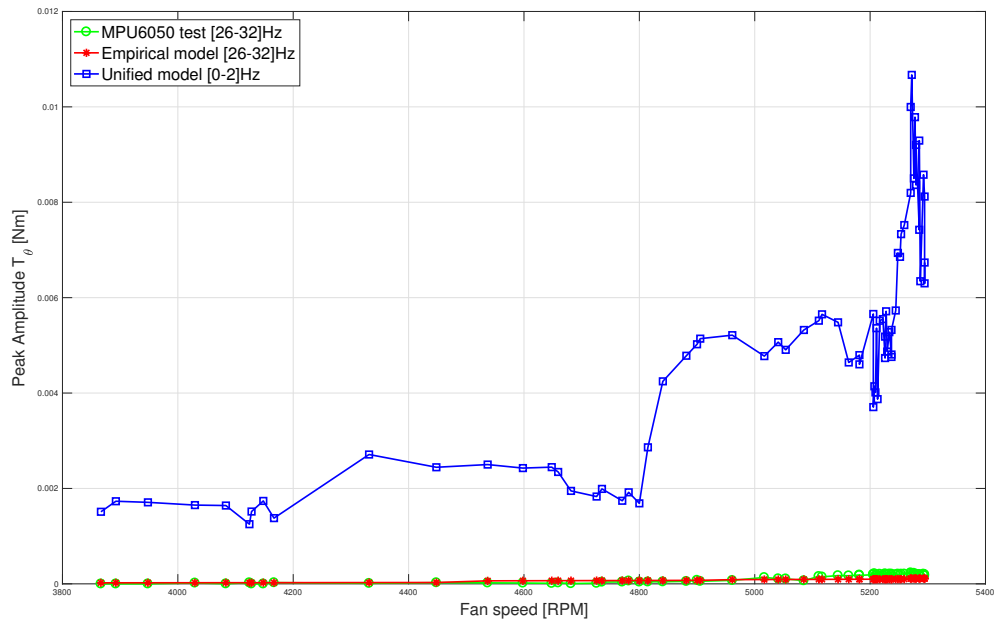


Figure 6.5: Comparison of all tests and models. PiFan 5V F_x data

Figure 6.6: Comparison of all tests and models. PiFan 5V F_y dataFigure 6.7: Comparison of all tests and models. PiFan 5V T_θ data

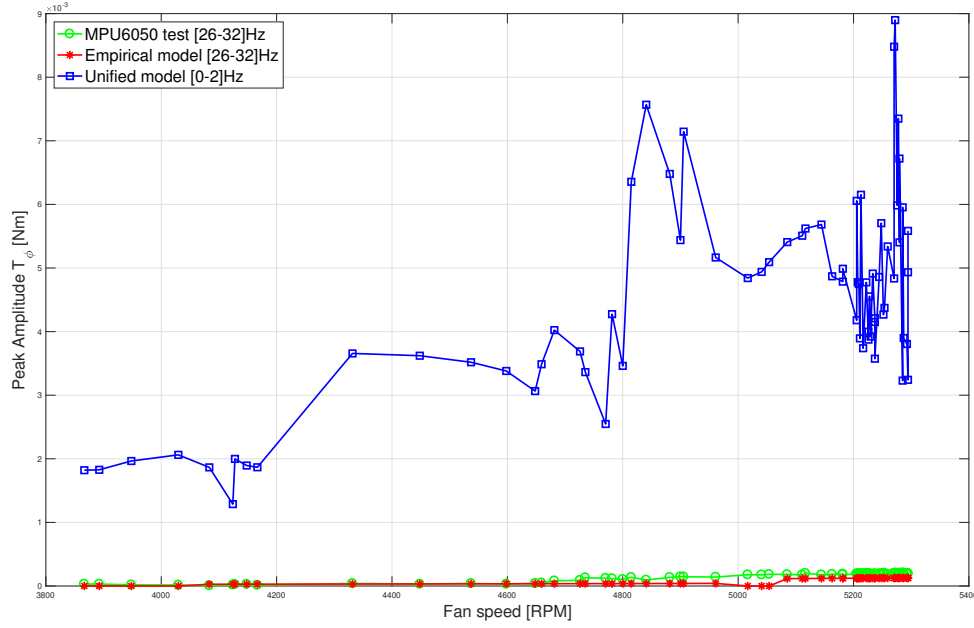


Figure 6.8: Comparison of all tests and models. PiFan 5V T_ϕ data

The closest tests and models results are arguably those of the PiFan at 5V, especially for forces 6.5 and 6.6. Here, the accelerometer data, empirical model, and unified model cross each other several times. However, they do not always follow the same pattern and they are still not close to complying with the 30% error requirements. As a matter of fact, at around 5300RPM, the unified model amplitudes of the F_x data are around 4 times as big as the accelerometer amplitudes, although examples could be made where they are closer to each other.

6.4. USBfan tests and models comparison

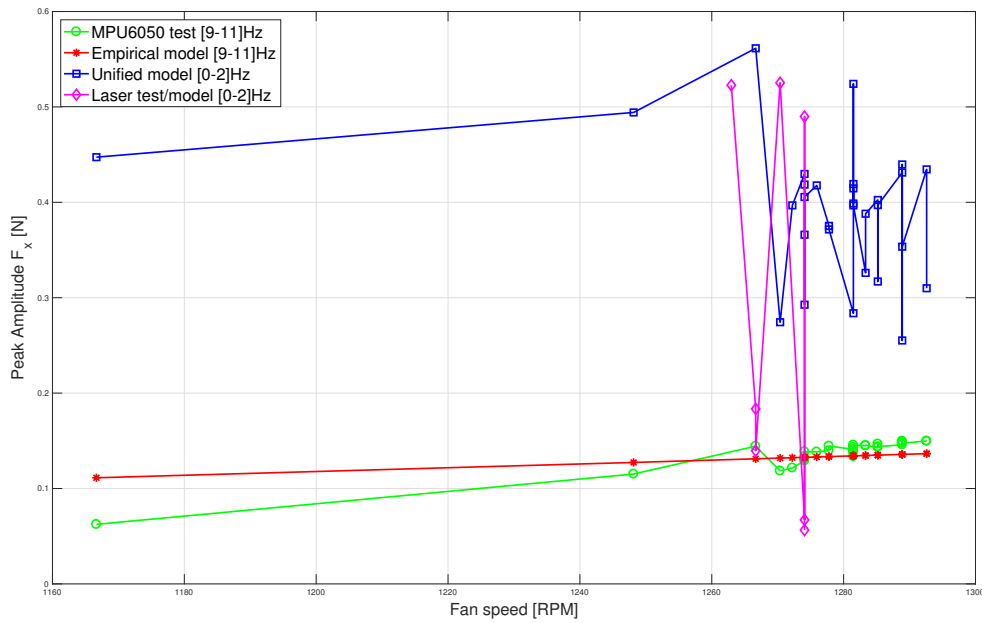


Figure 6.9: Comparison of all tests and models. USBfan F_x data

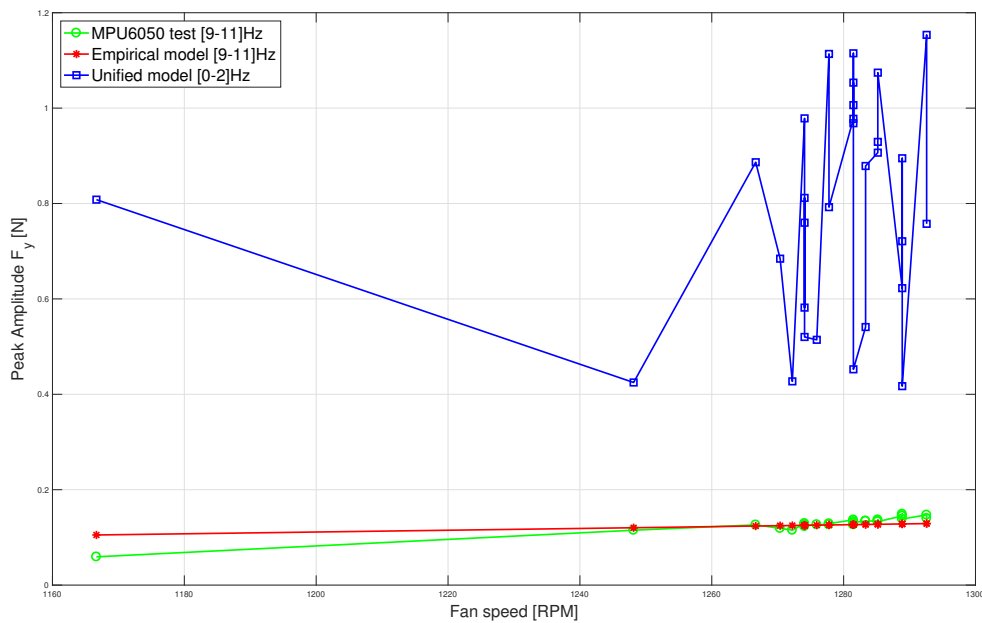
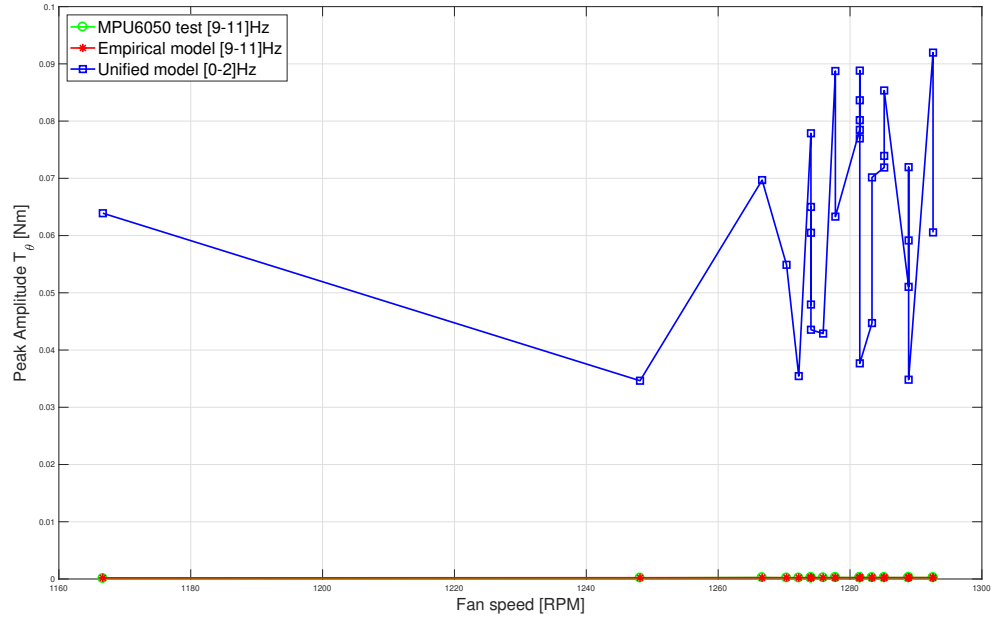
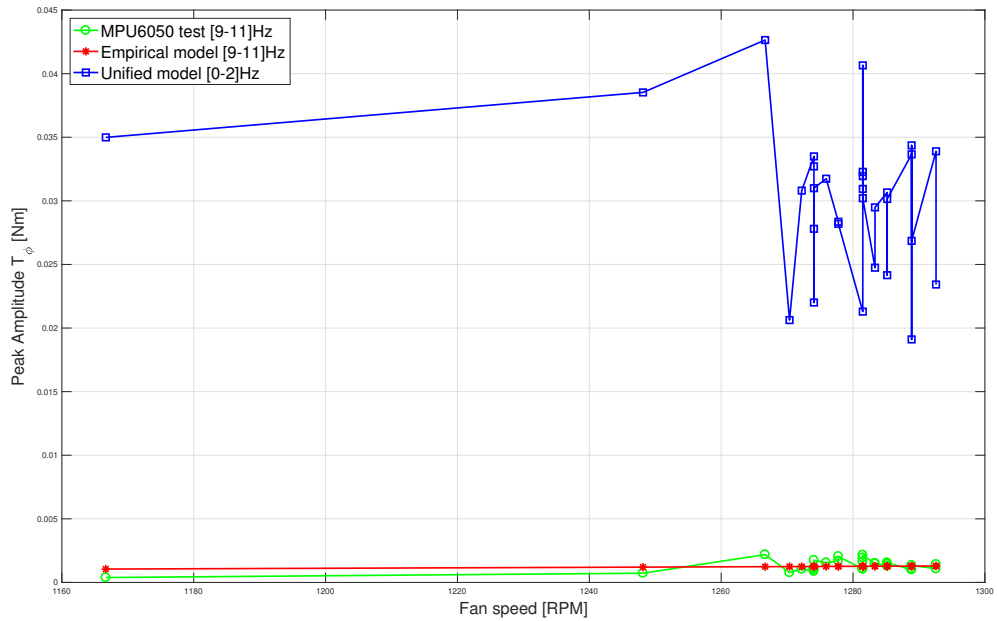


Figure 6.10: Comparison of all tests and models. USBfan F_y data

The best results for the laser test can be seen in figure 6.9, where its amplitude values are generally in between the unified model and accelerometer test data. However, a great difference in amplitudes can still be seen, especially at some RPM values. Slightly after 1260RPM, for example, the laser test and unified model amplitudes are more than 3 times as big as the accelerometer test data.

Figure 6.11: Comparison of all tests and models. USBfan T_θ dataFigure 6.12: Comparison of all tests and models. USBfan T_ϕ data

Overall, the unified model generally overpredicts the experimental data for all types of tests. Forces are generally closer to the model compared to torques. As mentioned, experimental torque data were very noisy, and that is because their amplitude is very small – since the rotational movement of the bracket around the x and y axes is constrained by the iron bars – and approaches the gyroscope noise threshold of the MPU6050. Forces, instead, are better captured by the MPU6050 and the result is also a closer match to the unified model. In the plots where forces get further away from the model, such as 6.9 and 6.10, their amplitudes are about

5 times smaller than the model ones. However, recall that in the soft-suspended mounting bracket by Sui et. al, the test data were about 16 times greater than the simulation, so these results already represent an improvement compared to those. The mounting bracket in this project can still not be validated, since it is not compliant with some requirements, as will be summarized in the next section, and both tests and models shall be improved. While ideas to improve the tests have been previously discussed in section 4.2, problems on the models haven't been discussed thoroughly. The main idea to improve the unified model is to determine input parameters more accurately. These include stiffness k , damping c , masses and inertias, and the transmissibility function. Stiffness requires either a better CAD model or an experimental measurement, which could be done for example by comparing displacement and force test data. Damping could be determined experimentally for example through the method of logarithmic decrement. Masses shall be measured experimentally and fed into the CAD model, in order to improve inertias as well. As a consequence, the transmissibility function will also be more accurate. The analytical values of transmissibility could then also be compared also to experimental ones, where the transfer function is retrieved by dividing disturbances measured with a soft-suspended approach by ones measured with a hard-mounted to ground approach.

All these recommendations will be recalled at the end of the next chapter.

6.5. Other requirements

With regard to requirement TES-F-002, specifying that the sensor shall measure disturbances in the $1-500\text{Hz}$ range, it was already said that for this project a very low bandwidth was set erroneously, which didn't make it possible to capture the whole range. However, in principle, the MPU6050 can achieve a sample rate of 1KHz , by disabling the digital low-pass filter. Therefore, the bandwidth could be set at 500Hz . In any case, the real sample rate would be limited by the Arduino reading speed, and with I2C communication it is unlikely to achieve that rate. Given how the requirement is stated, the MPU6050 would be able to comply with it, with a microcontroller other than Arduino Uno. However, since there was no direct verification of it in this project, it will be said that it's only partially compliant, with further work needed to verify it. To be sure to comply with this requirement, it is even more recommended to focus on other types of sensors, such as piezoelectric sensors [48] or high-precision industrial acceleration sensors [49], which are made on purpose to measure vibrations and can operate in the microvibration frequency range.

As for requirement MB-NF-002, asking that at least one mounting bracket eigenfrequency is in the fan speed range, recall that this was verified by the eigenfrequency plots 5.15, with values taken from the CATIA frequency cases. Even though the modes do not intersect the whole resonance zone of the fan speed, it is enough for all of them to be amplified, since the increase of transmissibility starts at frequencies a little lower than the fan speed, as seen in figure 5.16b. Therefore, the mounting bracket is compliant with this requirement.

For requirement TES-F-005, asking for the visibility of harmonic order 1 in the waterfall plots, only the USB fan is compliant, even though higher peaks are present at order 0.5 in this case. Therefore, this is not enough to comply with this requirement, also because the other tests on the PiFan didn't show order 1. This is related to the fact that the frequencies measured in the tests are not reliable.

Also, it was asked by requirement MOD-F-001 to calculate static and dynamic imbalances. This was done by the unified model, and the values are reported in table 5.4. However, given the discrepancy of model and test amplitudes identified in the previous sections, it can only be said that this requirement is partly validated, as the imbalance values are not so reliable.

As far as the cost is concerned, the cost requirement MB-NF-001 is easily verifiable as the whole test setup costs well below 200€, as shown in the figure below:

STORE	ITEMS	PRICE	TOTAL
Conrad	2 x Iron bars	8,99 €	96,84 €
vanallesmeer	2 x Hall sensors	6,70 €	
	10 x Magnets		
vanallesmeer	1 x Hall sensor	4,25 €	
	4 x Magnets		
Hackerstore	1 x Focus laser	21,05 €	
	1 x Laser module		
	1 x Acc + gyro module		
	1 x fan set		
Dennisdeal	1 x Laser reflecting mirror	16,54 €	
Hackerstore	1 x Breadboard + wires	19,90 €	
Action	1 x Silicon	11,86 €	
	1 x Silicon gun		
	1 x Floor protectors		
	1 x Hook & Loop tape		
	1 x Masking tape		
	1 x Double sided tape		
123-3D	1 x Female jumper wires set	7,55 €	

Figure 6.13: Total cost of test bench components

The only items missing in this list, since they were already owned or borrowed, are the USB fan, Arduino Uno, epoxy glue, and PLA filament for the 3D printer, whose total cost, however, stays well below 104€ (to reach the 200€ requirement). Therefore, the test bench meets requirement MB-NF-001. Since some components were also bought twice, the total cost could even be reduced, amounting to around 100€, including the components not on the list also. Furthermore, requirement MB-NF-001 mentions only test bench components, since the type of wheel that is going to be tested depends on the test operator's needs. Therefore, the costs of the USB fan and the PiFan should be further cut.

Conclusions and recommendations

In this chapter, the conclusions of this thesis project will be drawn. The major output in these conclusions is the Requirements Verification Matrix, which recalls the initial system requirements to indicate the current compliance of the system with each of these. Following this matrix, further conclusions will be given by providing a concise answer to each research question. Finally, recommendations will be given together with a suggestion on their priority.

7.1. Requirement Verification Matrix

In this section, a requirement verification matrix will be shown. This includes all requirements of the initial requirements matrix in 2.5, and it relates each requirement to one or more tests, models, or systems used in this project as verification methods. The cell they have in common will be colored green for Compliant (C), yellow for Partially Compliant (PC), and red for Non-Compliant (NC). The reasons for the state of compliance of each requirement have been explained in the previous chapter (6).

REQUIREMENT ID	REQUIREMENT DESCRIPTION	VERIFICATION METHODS						
		Mounting bracket	MPU6050 tests	Empirical Model	Unified Model	Laser tests	CAD model	Final comparison
MB-NF-001	The total fixed costs of all test bench components shall be less than 200€	C						
MB-NF-002	At least one of the eigenfrequencies of the test bench shall be inside the speed range of the fans						C	
MB-NF-003	The mounting bracket shall contain a soft-suspension made of flexible materials to facilitate the amplification of vibrations	C						
MB-F-001	The mounting bracket shall be able to be fixed to different types of wheels, with diameter within its maximum dimension	C						
MB-F-002	The mounting bracket shall allow microvibration measurements for at least two forces (Fx, Fy) and two torques (Tx, Ty), where x and y are the radial plane of the fan		PC					
TES-F-001	It shall be possible to generate waterfall plots from the tests results, with the disturbance amplitude plotted along the frequency or harmonic order spectrum and the fan speed		C					
TES-F-002	The sensor used in the test bench for microvibration measurements shall be able to measure disturbances in the 1-500Hz frequency band		PC					
TES-F-003	The sensor used in the test bench for measuring microvibrations shall be able to measure disturbance forces in the range [0.0186-2.807]mN		PC					
TES-F-004	The sensor used in the test bench for measuring microvibrations shall be able to measure disturbance torques in the range [0.0034-0.544]mNm		PC					
TES-F-005	The fan rotational speed shall be measured with a maximum uncertainty of ± 10 RPM		NC					
TES-F-006	The harmonic order 1 shall be visible in the mounting bracket test waterfall plots in order domain		NC					
TES-NF-001	At least one more type of microvibration test shall be performed, whose results can be compared to those of the mounting bracket					C		
TES-F-006	The waterfall plots generated by other types of tests shall be compared to the mounting bracket test results with a maximum error of 30% at any given frequency and speed					NC		NC
MOD-F-001	At least one of the models shall be able to calculate the static and dynamic imbalance of the fans				PC			
MOD-F-002	The models shall be able to generate waterfall plots, comparable to those of the tests			C	C	C		
MOD-F-003	The waterfall plots generated by the models shall be compared to the mounting bracket test results with a maximum error of 30% at any given frequency and speed			NC	NC	NC		NC

Figure 7.1: Requirements Verification Matrix

To conclude, a low-cost mounting bracket concept for microvibration testing of small reaction wheels has been proposed. The project presented several obstacles, starting from the test results. The Hall sensor could not measure the rotational speed correctly, and the speed had to be multiplied to match the datasheet values. Therefore, the RPM accuracy requirement could not be verified. Also, the values of frequencies recorded by the MPU6050 were compromised by the digital low-pass filter, which should be eliminated to measure microvibrations correctly in their frequency range. The best recommendation is to change the type of sensor, for example into piezoelectric sensors. Therefore, the flawed test data were input into the empirical and unified models. Although the empirical model was able to capture harmonic numbers correctly, a specific harmonic number that was expected, 1, was present in only one out of three test results. The final comparisons show that also model amplitudes are not to be relied on at all wheel speeds. As a consequence, the calculated static and dynamic imbalances can be a hint of how much imbalance the fans have, but do not represent accurate results. A laser test was also proposed, which could even be a first visual guess of how much residual imbalance a wheel has.

In short, the proposed test bench cannot be validated at the moment, but there is a lot of room for improvement.

7.2. Conclusions

This section reports concise answers to each research question, as defined in table 1.2.

Q1: Can a low-cost microvibration test bench be prototyped in-house?

A low-cost microvibration test bench was prototyped in-house for the cost of just 97€, including all electronics. The design was the outcome of a concept selection, which resulted in the choice of two test approaches and two measurement approaches. The test approaches are the ground-fixed approach, where vibrations are measured directly in contact with the wheel, which is fixed to the ground, and the soft-suspended approach, for which the 3D printed mounting bracket was built, which is where the amplified vibrations are measured from. The measurement approaches were accelerometer+gyroscope (MPU6050, applicable to both test approaches) and a laser pointer on a mirror on the mounting bracket (only in the soft-suspended case). However, the ground-fixed approach with the MPU6050 was soon discarded, due to extremely noisy measurements. The mounting bracket, instead, whose test results have been compared with models, can still not be validated (as seen in the next answers), but a lot of room for improvement is left.

Q2: Is it possible to measure in a systematic and reproducible way the microvibration signature of rotating (RW-like) objects in the order of the Delfi-PQ one ($[0.0186 - 2.807]mN$ forces and $[0.0034 - 0.544]mNm$ torques)?

As said in the previous answer, this is not possible with the ground-fixed approach and cheap sensors. However, the MPU6050 has proved to be able to capture at least the major microvibration peaks (due to imbalance) thanks to the soft-suspended approach. As explained in paragraph 4.3.3, for the USB fan case, a minimum source force of around $0.025mN$ has been measured in tests, together with a minimum source torque of around $0.001mNm$. This is very close to complying with requirement TES-F-003 for forces, and it complies with requirement TES-F-004 for torques. However, torques in particular have proved to be a little noisy, especially for the PiFan tests. Therefore, for both requirements, the system has been judged partially compliant since improvement is needed. To be able to read even lower source disturbances, it could be tried to push the transmissibility function a bit more into the resonance zone, to amplify vibrations even more. This doesn't work however for high-frequency disturbances, and the focus will still be disturbances due to imbalance at low frequencies.

Q2.1: Is it possible to measure the rotational speed of the rotating objects?

In principle, this would be an easy task to accomplish, even with cheap sensors. However, the Hall-effect sensor, controlled by an Arduino sketch, could not read speeds correctly, so the speeds were multiplied by a factor of 3.7 to match the datasheet values. This makes the RPM data not reliable and as such also the harmonic numbers will be inaccurate. Therefore, it should definitely be fixed in a future iteration. Recommendations to achieve this can be found in section 4.2 and include: using an Arduino Mega instead of Arduino Uno, so that data from the MPU6050 and Hall sensor do not have to be logged one after the other (interrupt-I2C), which could cause Arduino to decrease its logging rate, but can be logged simultaneously, thanks to Mega's double set of I2C interfaces. Another possible solution is to add more magnets on the fans,

so that more pulses per revolution would be read, thus making the measurement more reliable. Finally, the mounting bracket could be slightly redesigned to fix the Hall sensor on top of it, so that it moves together with the magnets and doesn't miss pulses. In this case, the sensor stayed still above the fans but was not fixed to the bracket, so the magnets may have gone outside the range of the sensor, which in turn missed some pulses.

Q2.2: *Is it possible to obtain microvibration plots in frequency or order domain?*

Yes, microvibration waterfall plots were successfully visualized after post-processing in MATLAB, as seen in figures 4.9 and 4.11, and in appendix A. For these plots, the major drawback is the low-pass filter at 21 Hz which was embedded in the MPU6050, and made frequencies unreliable. This can be easily eliminated from the Arduino sketch, allowing the MPU6050 to reach a bandwidth up to 500 Hz.

Q2.3: *Can the expected harmonic orders be identified in the test results?*

This is related to the answer Q2.1, as it was said that unreliable RPM data made the harmonic orders inaccurate too. The expected order 1 (the order of imbalance disturbances) has been visualized, in fact, only in one out of three MPU6050 tests (figure 4.9), while it wasn't present in the PiFan results. So, unfortunately, even though some harmonic orders were identified through the empirical model, these are not reliable, and the RPM measurement problem should be solved first, to be able to address this problem as well.

Q3: *Is it possible to calculate static and dynamic imbalances from the test results?*

Static and dynamic imbalances are visualized at harmonic order 1. Therefore, this question is strongly related to Q2.3, for which a negative answer was given. As a result, also in this case the calculated imbalances (table 5.4) cannot be considered accurate, as they are retrieved from the maximum amplitude coefficient (equation 5.69), rather than from the amplitude coefficient of order 1. This was done also because the unified model frequencies didn't match the test ones (and didn't show order 1 either), so it was decided to compare similar amplitudes at different frequency ranges. Therefore, in the next iterations, first it has to be made sure that order 1 is visible in all test and model results, and only then calculate imbalances.

Q4: *Can the test results be validated?*

MPU6050 test results have undergone a validation process through comparison with the laser test results (only in case of F_x) and with the empirical and unified models, as seen in chapter 6. However, the unified model generally overpredicts the test data, often being several times greater than them. The requirements TES-F-006 and MOD-F-003, asking for a maximum 30% error between tests and models, can then not be verified at this stage. The RPM measurement problem and the low-pass filter on the MPU6050 shall be addressed first, to get good test results, and only then the models will be able to show good results as well (since they take parameters from tests, as harmonic numbers and amplitude coefficients). Furthermore, it shall still be determined why the unified model returns peaks at much lower frequencies than the test ones. The most likely identified cause is that the transmissibility function is not accurate enough, hence it could be tried for example to measure it empirically in the next iterations.

Q4.1: *Is it possible to simulate the test results with models?*

Empirical and analytical models have been used in this project. The empirical model is a parameter fitting and harmonic identification model, that takes the test data as input to estimate amplitude coefficients and harmonic orders. The analytical model instead solves the equations of motion of the system. A refined, unified model is built by using the disturbances estimated by the empirical model as the right-hand side of the equations of motion. The results of the models are explained in the answer to Q4.

Q4.2: *Is it possible to compare the test results with other types of tests?*

This was also mentioned in the answer to Q4. The test results of the MPU6050 were compared with the results of the laser tests, where a laser was pointed to a mirror on the top base of the mounting bracket, and the displacement of the reflected dot was determined via an object recognition script. This was done only for F_x since it would require multiple lasers to measure simultaneously along multiple directions. Laser tests also showed problems since their amplitudes are in certain cases 5 or 6 times larger than those of the MPU6050. Therefore, due to the low resolution of this system, it was concluded that laser tests could be only used as a first guess to understand for example if imbalances have decreased or not, but do not provide accurate results. Therefore, they cannot be used to validate MPU6050 results.

7.3. Recommendations

This final recommendations section focuses on possible improvements on the current test bench and also contains proposals for alternative measurement approaches. These will be described according to a list of priorities. That is why recommendations will be enumerated, starting from the one that is considered to be the most important at the moment. The reader's best judgment shall, in any case, be used, joint by further investigation on the subject, to establish a definitive line of action for future work.

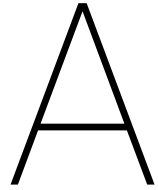
The first two recommendations in this priority list will focus on the current measurement approach. Since they are modifications of the existing system with only moderate changes of design, their implementation will arguably be easier compared to working on a new design. Then, recommendation 3 will recall possible solutions for alternative sensors. In point 4, some suggestions will be given also on how to improve the unified model. Finally, advice on optional general improvements of the mounting bracket will be given in point 5, in case the previous recommendations should not give the desired results yet.

1. A major problem in the current system is that the RPM measurement was not accurate enough. The measured speeds, in fact, were multiplied by a factor of 3.7 to match the datasheet values. As a result, speeds, frequencies, and harmonic numbers are not reliable and this represents a problem for the inputs of the microvibration models. The most likely cause for the inaccurate RPM measurements is the fact that the magnets often moved too far away from the Hall sensor during tests, so the sensor may have skipped some pulses and read lower speeds. A simple test could be done on a ground-fixed wheel to understand whether this was actually the problem, as magnets will not move away from the sensor in this case and therefore this should output accurate speed values. A solution, in this case, could be to make a small design modification to the mounting bracket, so that it can accommodate the Hall sensor and always keep it on top of the trajectory of the magnets. Please follow the answer to Q2.1 (7.2) and section 4.2 for further suggestions on this.
2. In case it is decided to keep working with the MPU6050 in the future, the priority, in this case, is to eliminate the 21 Hz digital low-pass filter embedded in the MPU6050, especially if disturbances happening at frequencies higher than those of imbalances want to be visualized. The low-pass filter, together with the inaccurate RPM measurement, also made frequencies unreliable in this project. The problem can be solved by deleting the `mpu.setFilterBandwidth()` command (from the Adafruit_MPU6050 library) in the Arduino sketch to disable the low-pass filter and reach a bandwidth up to 500 Hz. It may be that the filter will stay on even after deleting this command and will switch to its default value of 260 Hz. In this case, it is possible to delete the `setFilterBandwidth(MPU6050_BAND_260_HZ)` command from the `Adafruit_MPU6050.cpp` library file.
3. Another solution is to choose another type of sensor, which provides multiple advantages. Hints for this could come for example from the concept selection 2.3 or the failed attempts 3.3.3, but should not be limited to them. The first advantage is that by choosing a higher-resolution sensor the ground-fixed approach, which provided noisy results with the MPU6050, could be tried again. Second, a sensor with larger bandwidth could be selected, above 1 kHz, as opposed to the 500 Hz of the MPU6050. However, if the goal is just to measure imbalances, it would not be needed, as these happen at lower frequencies. The first suggestion for another type of sensor, in this case, is the Polytec Laser Doppler Vibrometer, which is also owned by the PME department at TU Delft. In case it is borrowed, of course, this wouldn't affect costs. However, in terms of scientific proposal, the cost of the entire setup would change dramatically, so the goal would not be to build a low-cost measurement test bench anymore. On the other hand, it could be used as a reliable method of validation (for a less expensive sensor), thanks to its extremely high resolution and its capability of reading displacements down to around 1 nm. Furthermore, its bandwidth is well above the microvibration range (1 kHz), namely around 10 kHz. Therefore, it is expected to be possible to use the ground-fixed approach and still obtain the microvibrations on their whole range with this vibrometer. This could also be a way to verify the transmissibility function (whose analytical expression proved to be inaccurate for the unified model), by dividing the mounting bracket results by the ground-fixed results. A major downside of the vibrometer, however, is that it measures only in one direction. Therefore, multiple measurements would have to be done to obtain forces in 3 directions, while torques cannot be measured. In case this is considered important for future iterations (for example if a unified model has to be implemented and torques are absolutely needed), then a contact sensor is suggested. As mentioned, even the Kistler dynamometers wouldn't have a high enough resolution to measure vibrations accurately for these sizes of RW's, with their lowest measurable force

at $2mN$, as opposed to the $0.0186mN$ required. However, Kistler is specialized in dynamometers that are widely used for microvibration measurements. Therefore, the suggestion is to contact Kistler to know if they have any small dynamometer available that could be suitable for this task, or if the actual noise threshold is actually lower than what is reported in datasheets. The last recommended solution is to search for piezoelectric sensors, probably in a little higher price range than that of the MPU6050. This could also lower the noise threshold with respect to cheap accelerometers and especially increase bandwidth, as most piezoelectric sensors can measure above $1kHz$ since they are built for vibration measurements.

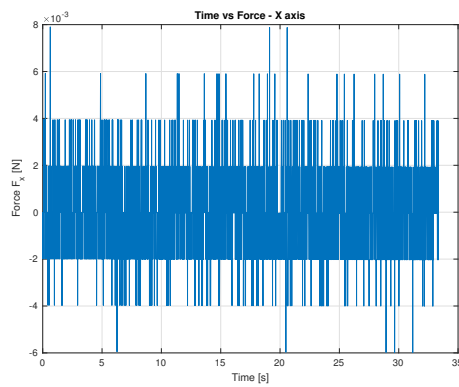
4. To improve the validation procedure, not only test results should be improved, but also microvibration models. The empirical model will improve on its own, as a consequence of improving experimental data, since it is a parameter fitting model. Therefore, after good test data are ingested by the model, this is expected to return more accurate harmonic numbers and amplitude coefficients. The unified model, however, can be further improved independently of other tests and models. In particular, it is recommended to improve the values of the input parameters, especially stiffness k , damping c , masses, and inertias. The task will be quite easy for masses since an electronic scale would suffice to make the mass measurements more precise. However, it is not trivial to improve the other parameters. The improvement of stiffness and mass would require a more representative CAD model, with more details on the fan, for example with the design of the ball bearings and the BLDC motor below the blades, instead of the current mass dummy, and with more details at the interface, including real screws rather than just connections. By inserting real mass values, the calculation of inertias will also be more accurate. Stiffness, together with damping, could also be determined experimentally. Stiffness, for example, could be retrieved by a ratio of force and displacement test amplitudes on the mounting bracket, which could be measured by a laser vibrometer and a Kistler dynamometer respectively. Damping could be determined via the method of logarithmic decrement, which consists in analyzing how much the vibrating system's amplitude has decayed after a certain amount of cycles. This could be implemented by letting the bracket vibrate freely, starting from a different position than the rest state, with no input force or velocity.
5. Finally, even though this is lower on priority, it was mentioned that the desired disturbance ranges, defined by TES-F-003 and TES-F-004, were measured only partially by the MPU6050, since some noise was still present at the lower values. This could be solved by slightly changing the design of the mounting bracket, to modify its eigenfrequencies and make it work fully in its resonance zone, to amplify vibrations even more. Beware that this is recommended only in case the focus is on the calculation of static and dynamic imbalance, but it won't improve higher frequencies, since after the resonance zone these are damped rather than amplified. Furthermore, the design of the mounting bracket shall be done with heavier materials, especially for the bottom base, and the test shall be performed on a heavier table, in order not to transmit vibrations to the ground and obtain a coupling effect between the two. This is a common practice in standard reaction wheel microvibration testing, so it is recommended even though it will probably slightly increase the cost.

Appendices

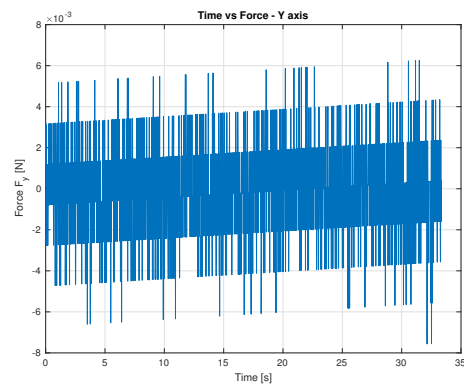


Additional test results

A.0.1. MPU6050 test results (PiFan 3.3V hard-mounted to ground)

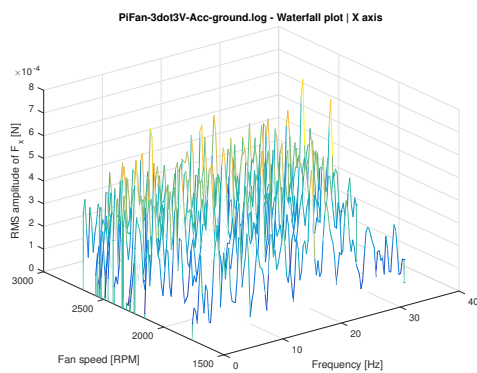


(a)

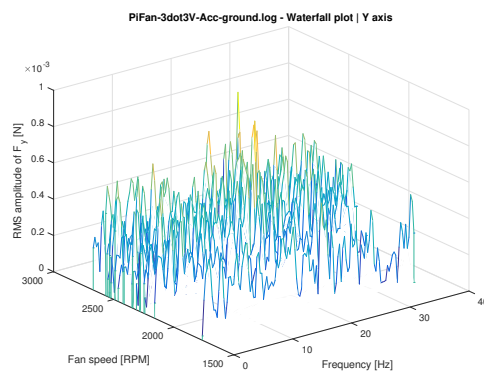


(b)

Figure A.1: Test results: Force-time plots of the ground-fixed PiFan 3.3V

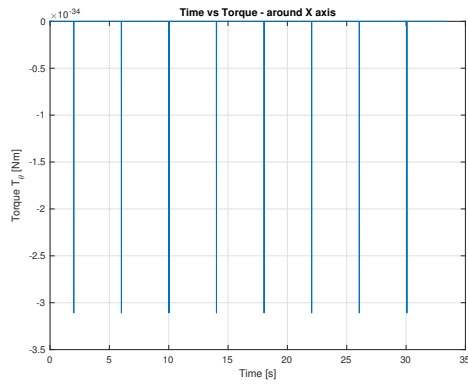


(a)

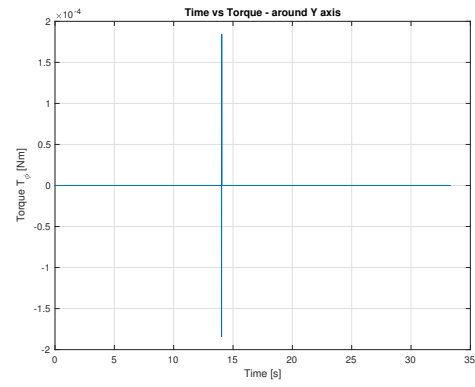


(b)

Figure A.2: Test results: Waterfall Force plots of the ground-fixed PiFan 3.3V

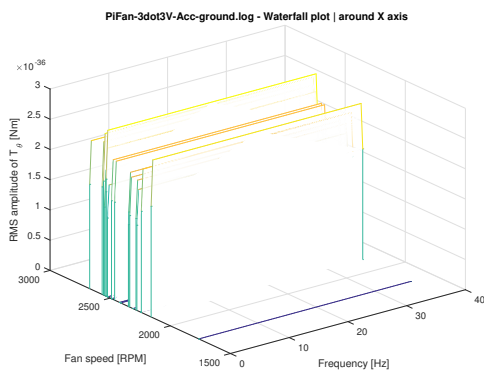


(a)

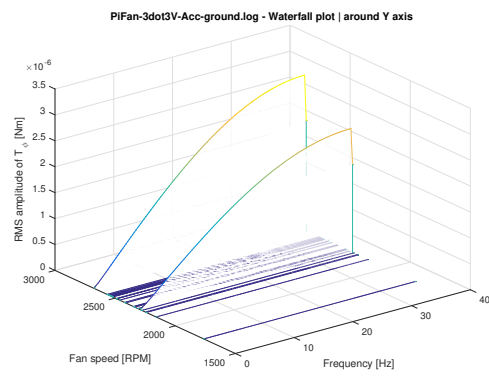


(b)

Figure A.3: Test results: Torque-time plots of the ground-fixed PiFan 3.3V



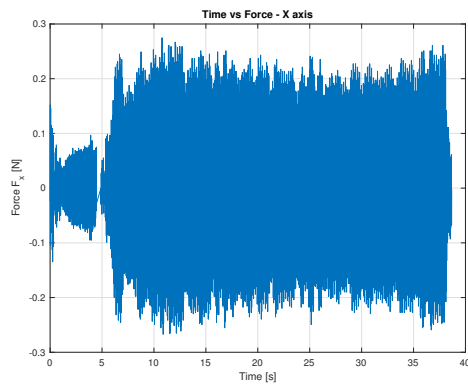
(a)



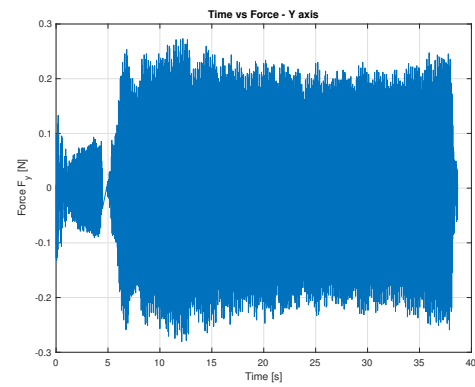
(b)

Figure A.4: Test results: Waterfall Torque plots of the ground-fixed PiFan 3.3V

A.0.2. MPU6050 test results (PiFan 3.3V hard-mounted to mounting bracket)



(a)



(b)

Figure A.5: Test results: Force-time plots of the PiFan 3.3V mounting bracket

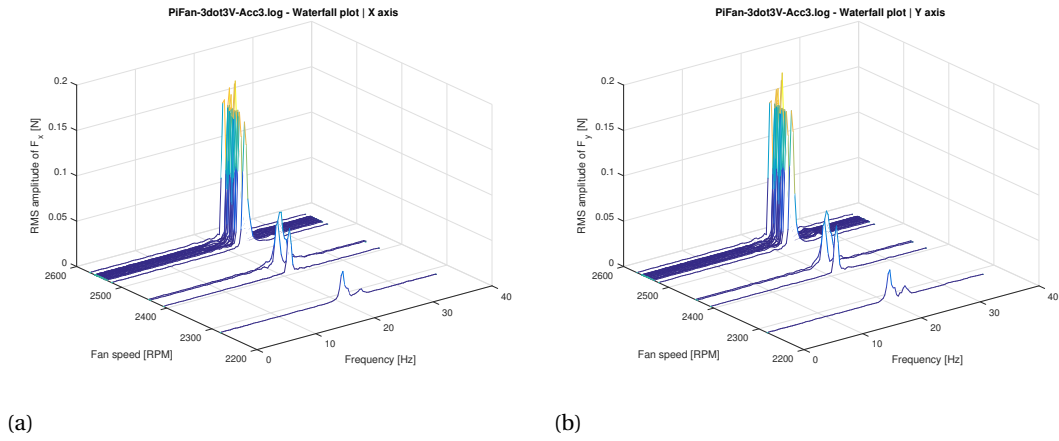


Figure A.6: Test results: Waterfall Force plots of the PiFan 3.3V mounting bracket

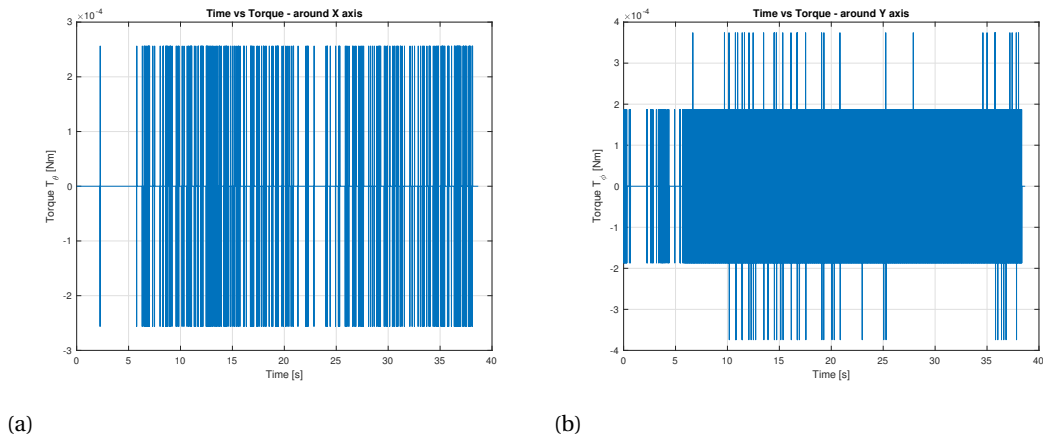


Figure A.7: Test results: Torque-time plots of the PiFan 3.3V mounting bracket

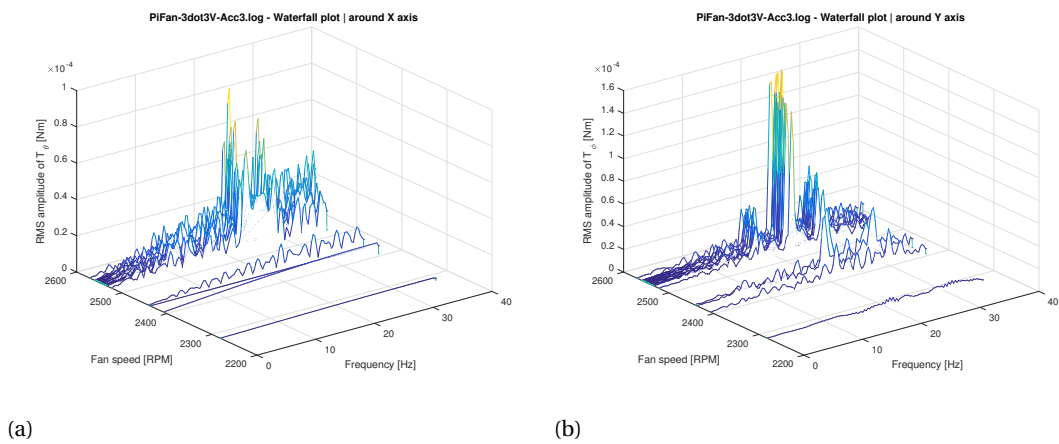


Figure A.8: Test results: Waterfall Torque plots of the PiFan 3.3V mounting bracket

A.0.3. MPU6050 test results (PiFan 5V hard-mounted to ground)

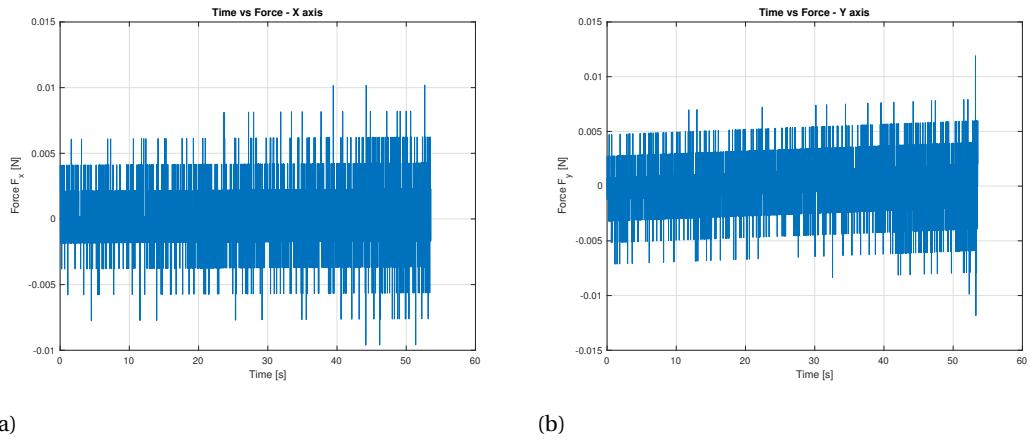


Figure A.9: Test results: Force-time plots of the ground-fixed PiFan 5V

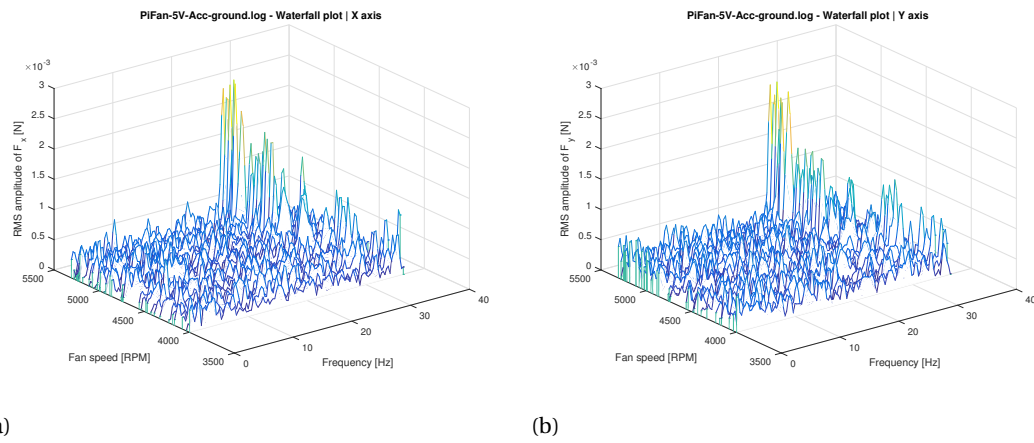


Figure A.10: Test results: Waterfall Force plots of the ground-fixed PiFan 5V

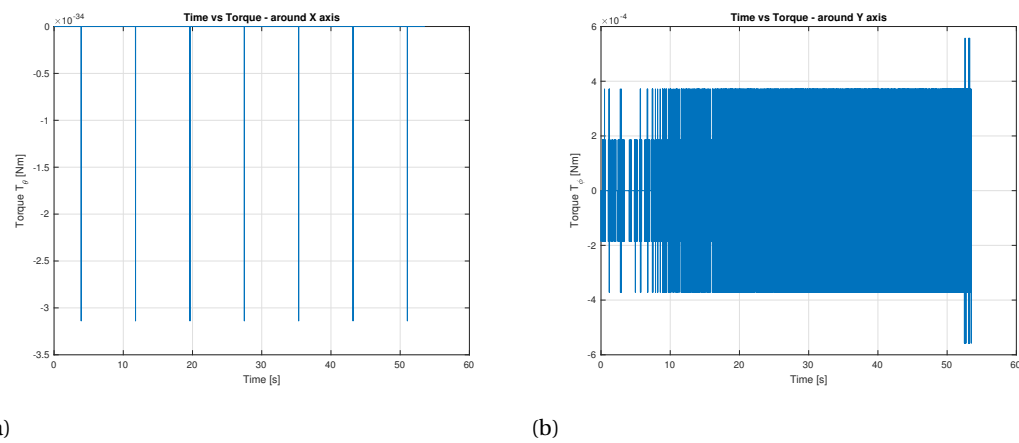
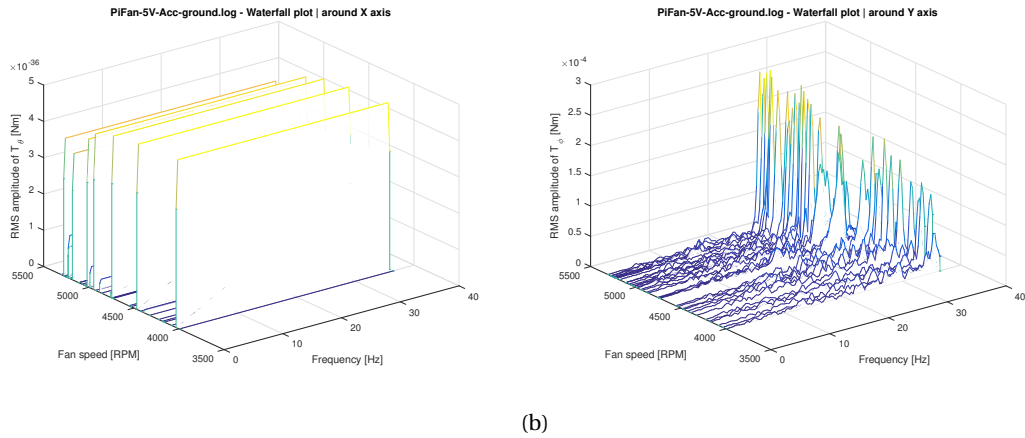


Figure A.11: Test results: Torque-time plots of the ground-fixed PiFan 5V

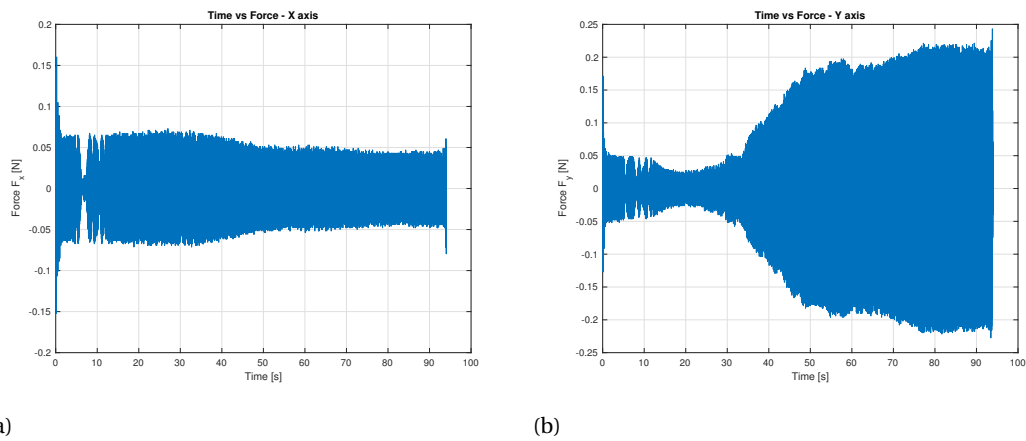


(a)

(b)

Figure A.12: Test results: Waterfall Torque plots of the ground-fixed PiFan 5V

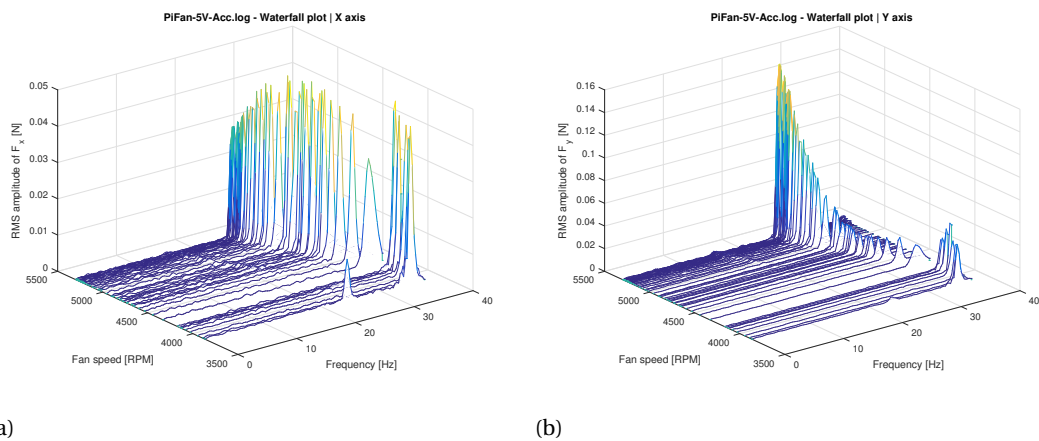
A.0.4. MPU6050 test results (PiFan 5V hard-mounted to mounting bracket)



(a)

(b)

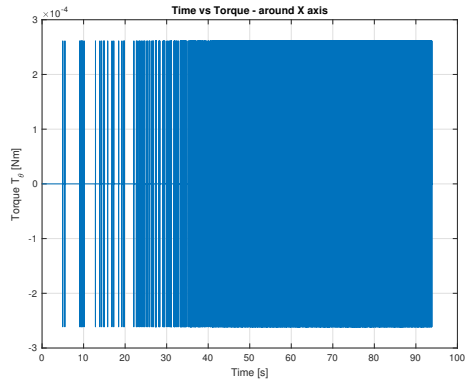
Figure A.13: Test results: Force-time plots of the PiFan 5V mounting bracket



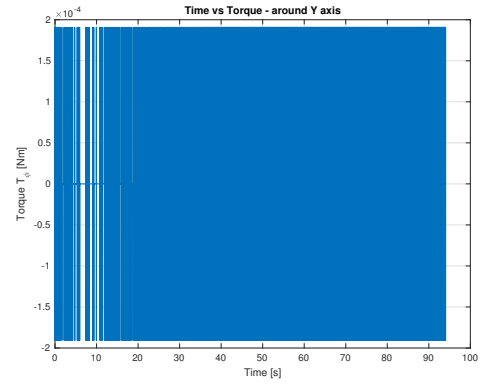
(a)

(b)

Figure A.14: Test results: Waterfall Force plots of the PiFan 5V mounting bracket

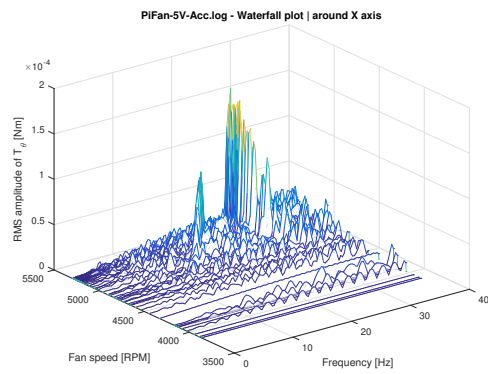


(a)

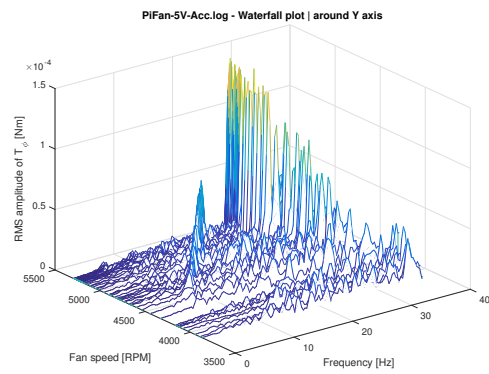


(b)

Figure A.15: Test results: Torque-time plots of the PiFan 5V mounting bracket



(a)



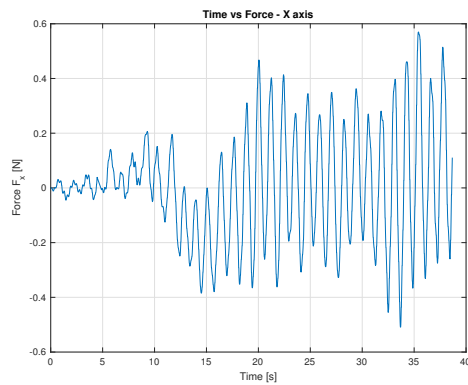
(b)

Figure A.16: Test results: Waterfall Torque plots of the PiFan 5V mounting bracket

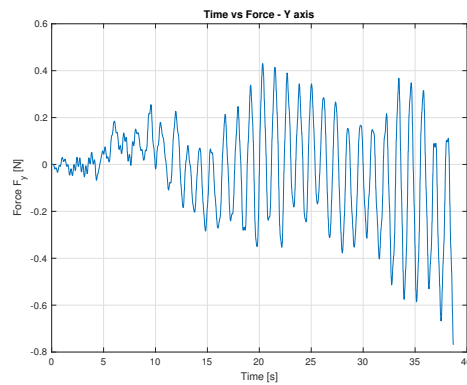
B

Additional unified model results

B.1. PiFan 3.3V

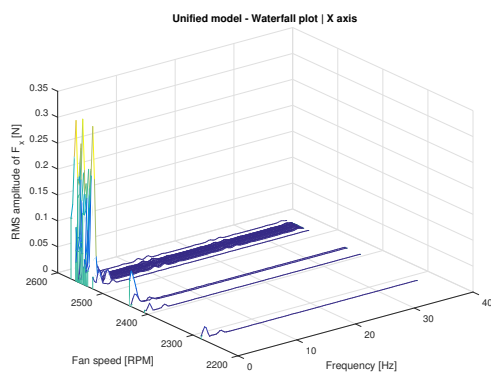


(a)

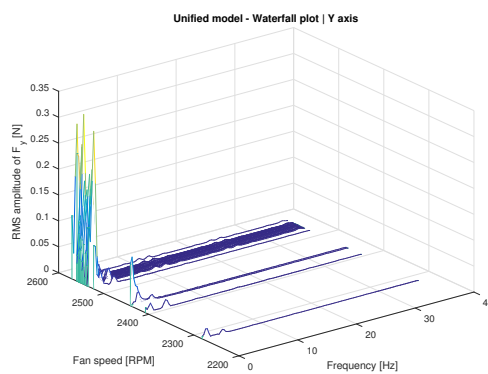


(b)

Figure B.1: Unified model results: Force-time plots of the PiFan 3.3V mounting bracket

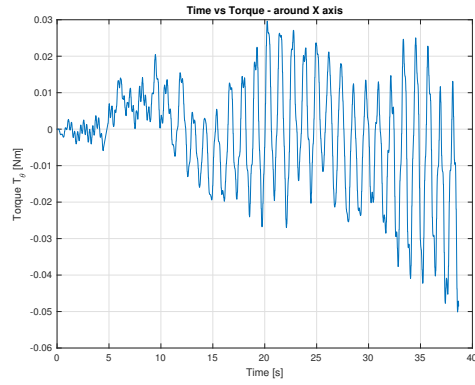


(a)

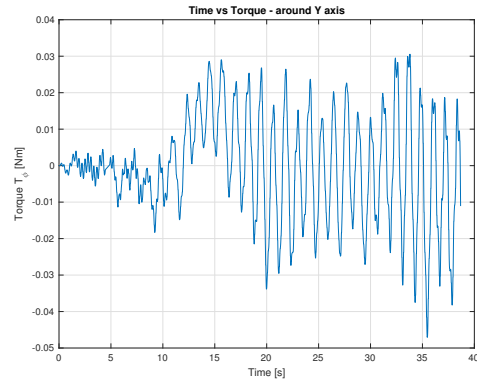


(b)

Figure B.2: Unified model results: Waterfall Force plots of the PiFan 3.3V mounting bracket

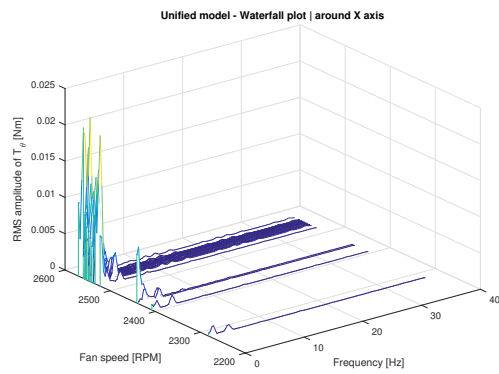


(a)

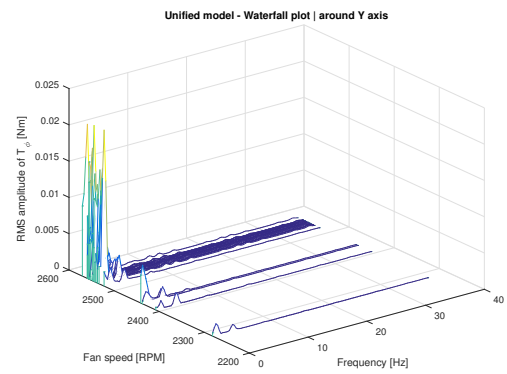


(b)

Figure B.3: Unified model results: Torque-time plots of the PiFan 3.3V mounting bracket



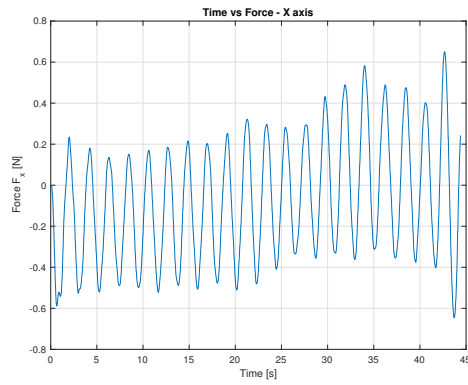
(a)



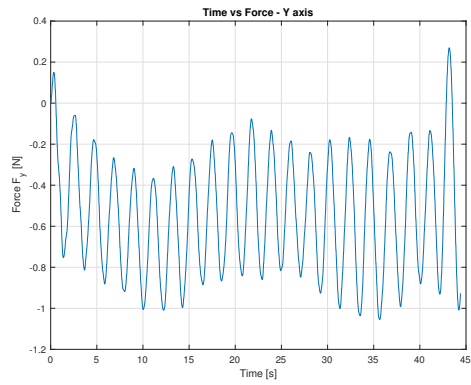
(b)

Figure B.4: Unified model results: Waterfall Torque plots of the PiFan 3.3V mounting bracket

B.2. USBfan

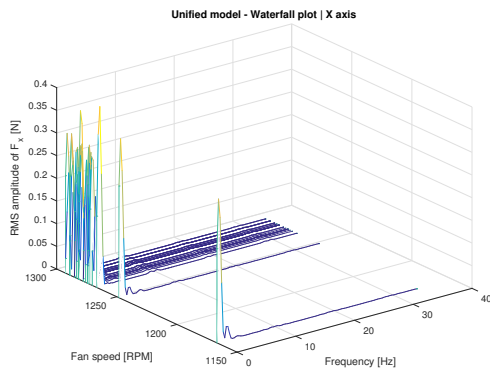


(a)

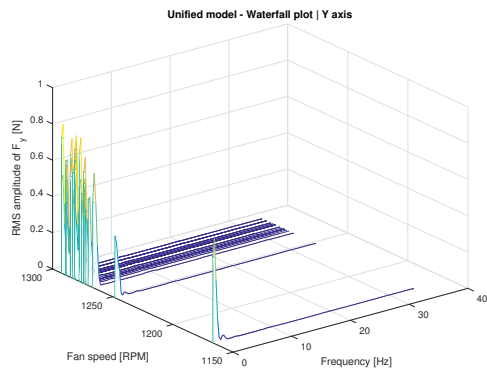


(b)

Figure B.5: Unified model results: Force-time plots of the USBfan mounting bracket

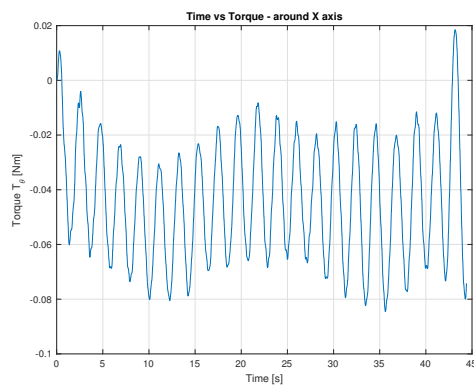


(a)

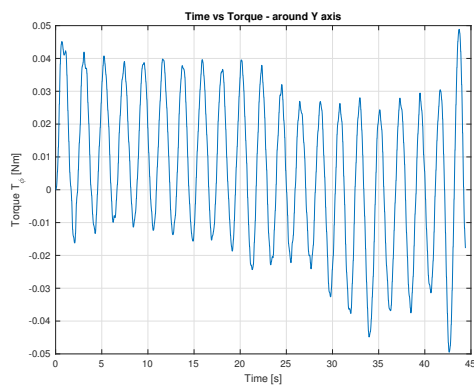


(b)

Figure B.6: Unified model results: Waterfall Force plots of the USBfan mounting bracket



(a)



(b)

Figure B.7: Unified model results: Torque-time plots of the USBfan mounting bracket

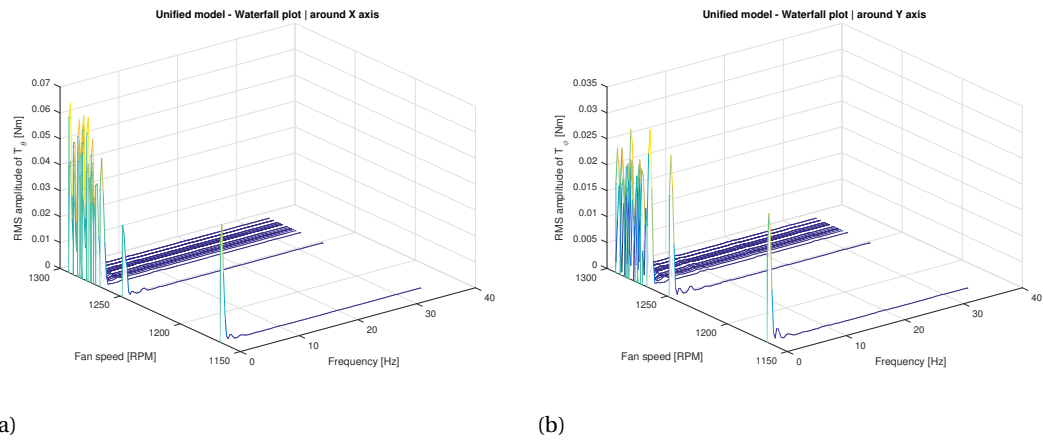


Figure B.8: Unified model results: Waterfall Torque plots of the USBfan mounting bracket

C

Additional laser displacement model results

C.1. PiFan 3.3V

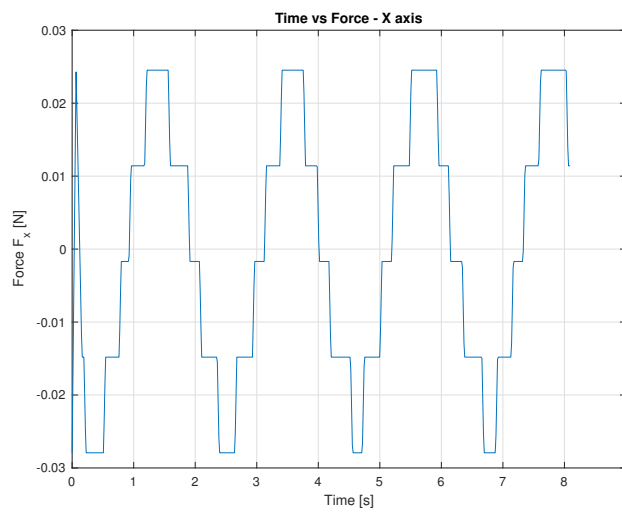


Figure C.1: Time-Force plot of the PiFan (@3.3V) laser displacement model

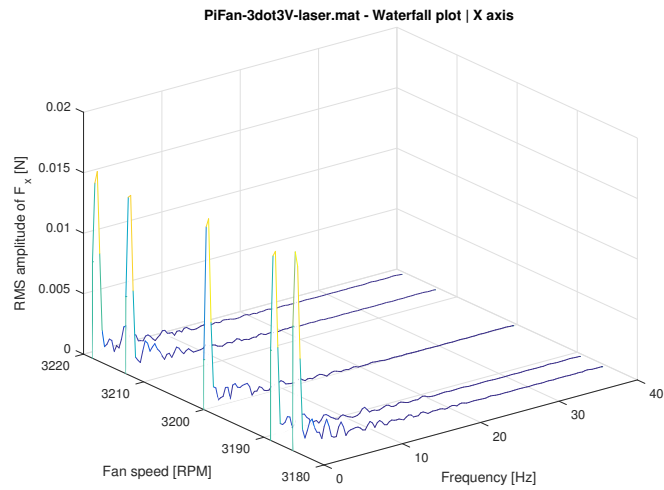


Figure C.2: Waterfall plot of the PiFan (@3.3V) laser displacement model

C.2. PiFan 5V

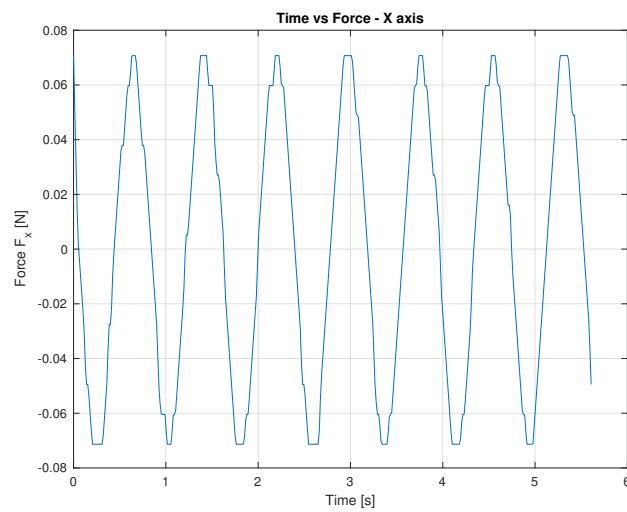


Figure C.3: Time-Force plot of the PiFan (@5V) laser displacement model

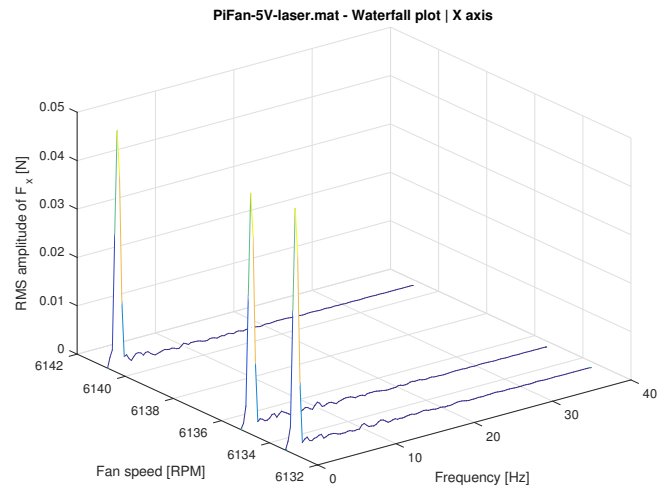


Figure C.4: Waterfall plot of the PiFan (@5V) laser displacement model

Bibliography

- [1] Cornelius Dennehy and Oscar S Alvarez-Salazar. Spacecraft micro-vibration: a survey of problems, experiences, potential solutions, and some lessons learned. 2018.
- [2] Tom Vergoossen. Design, integration and testing of the delfi-pq satellite reaction wheel. *MSc Thesis, Delft University of Technology*, 2017.
- [3] Antonius GL Hoevenaars. Design, integration and verification of the delfi-n3xt reaction wheel system. *Msc Thesis, Delft University of Technology*, 2012.
- [4] Stefan Wismer, René Messing, and Mark Wagner. First real-life results of novel micro vibration measurement facility. *Proc. "ESMATS*, pages 20–22, 2017.
- [5] Kistler ceramic micro-vibration force plate, type 9236a datasheet. <https://www.kistler.com/files/document/003-460e.pdf?callee=frontend>.
- [6] Christopher Masaru Pong, Matthew William Smith, Matthew W Knutson, Sungyung Lim, Sara Seager, Jesus Noel Samonte Villasenor, Shawn D Murphy, and David W Miller. One-arcsecond line-of-sight pointing control on exoplanetsat, a three-unit cubesat. 2011.
- [7] Kistler multichannel laboratory charge amplifier, type 5080a datasheet. <https://www.kistler.com/files/document/000-744e.pdf?callee=frontend>.
- [8] Kistler ceramic micro-vibration force plate, type 9236a instruction manual. <https://www.kistler.com/files/document/002-883e.pdf?callee=frontend>.
- [9] Stefan Wismer, René Messing, and Mark Wagner. First real-life results of novel micro vibration measurement facility. *Proc. "ESMATS*, pages 20–22, 2017.
- [10] M.P. Le. *Micro-disturbances in reaction wheels*. PhD thesis, Department of Applied Physics, 3 2017. Proefontwerp.
- [11] Jian Guo and Congying Han. Where is the limit: The analysis of cubesat adcs performance. 05 2016.
- [12] Ian Howard. A review of rolling element bearing vibration "detection, diagnosis and prognosis". 10 1994.
- [13] Wael A Salah, Dahaman Ishak, and Khaleel J Hammadi. Minimization of torque ripples in bldc motors due to phase commutation-a review. *Przegląd Elektrotechniczny*, 87(1):182–188, 2011.
- [14] D Addari, GS Aglietti, and M Remedia. Experimental and numerical investigation of coupled microvibration dynamics for satellite reaction wheels. *Journal of sound and vibration*, 386:225–241, 2017.
- [15] Zhe Zhang, Guglielmo S Aglietti, and Weijia Ren. Coupled microvibration analysis of a reaction wheel assembly including gyroscopic effects in its accelerance. *Journal of Sound and Vibration*, 332(22):5748–5765, 2013.
- [16] Keiji Komatsu and Hideki Uchida. Microvibration in spacecraft. *Mechanical Engineering Reviews*, 1(2):SE0010–SE0010, 2014.
- [17] Laurent Soula and Gregory Laduree. Modelling micro-vibrations by finite element model approach. In *12th European Conference on Spacecraft Structures, Materials and Environmental Testing*, volume 691, page 40, 2012.
- [18] Zhe Zhang, Guglielmo S Aglietti, and Weiyong Zhou. Microvibrations induced by a cantilevered wheel assembly with a soft-suspension system. *AIAA journal*, 49(5):1067–1079, 2011.
- [19] ECSS-E-HB-32-26A. Spacecraft mechanical loads analysis handbook, 2013.

- [20] Xin Sui, Chunyang Liu, Jishun Li, Yujun Xue, Yongjian Yu, and Yong Cui. Laser-based measurement for micro-unbalance of cylindrical rollers of the high-speed precision rolling bearings. *Cluster Computing*, pages 1–9, 2018.
- [21] Chunlei Jiang, Zihua Zhang, and Chengwei Li. Vibration measurement based on multiple self-mixing interferometry. *Optics Communications*, 367:227–233, 2016.
- [22] Pascal Guay and Ahmed Frikha. Ball bearing stiffness. a new approach offering analytical expressions. In *Proceedings of the 16th European Space Mechanisms and Tribology Symposium (ESMATS 2015)*, 2015.
- [23] J.L. Rijnberg. Theoretical modeling of the stiffness of angular contact ball bearings using a two dof and a five dof approach. *MSc Thesis, Eindhoven University of Technology*, 2007.
- [24] Geert Smet, Guy Richardson, Simon McLaren, and Andrew Haslehurst. Managing reaction wheel microvibration on a high resolution eo small spacecraft. In *15th European Space Mechanisms & Tribology Symposium*, pages 1–8, 2013.
- [25] C. Zwysig, T. Baumgartner, and J. W. Kolar. High-speed magnetically levitated reaction wheel demonstrator. In *2014 International Power Electronics Conference (IPEC-Hiroshima 2014 - ECCE ASIA)*, pages 1707–1714, May 2014.
- [26] ZHOU Weiyong, LI Dongxu, LUO Qing, and LIU Kun. Analysis and testing of microvibrations produced by momentum wheel assemblies. *Chinese Journal of Aeronautics*, 25(4):640–649, 2012.
- [27] Rebecca Ann Masterson. Development and validation of empirical and analytical reaction wheel disturbance models. *MSc Thesis, Massachusetts Institute of Technology*, 1999.
- [28] Rebecca A Masterson, David W Miller, and Robert L Grogan. Development and validation of reaction wheel disturbance models: empirical model. *Journal of Sound and Vibration*, 249(3):575–598, 2002.
- [29] Cornelius J Dennehy. A survey of reaction wheel disturbance modeling approaches for spacecraft line-of-sight jitter performance analysis. In *Munich, Germany: European Space Mechanisms and Tribology Symposium*, 2019.
- [30] Brian Travis Gibson. Custom low-cost force measurement methods in friction stir welding. *MSc Thesis, Vanderbilt University*, 2011.
- [31] Francois Decobert, Mark Wagner, and Stephen Airey. New facility for micro-vibration measurements esa reaction wheel characterisation facility. In *12th European Conference on Spacecraft Structures, Materials and Environmental Testing*, volume 691, page 39, 2012.
- [32] D Addari, GS Aglietti, M Remedia, G Richardson, and B LePage. Inspecting the characterisation of microvibration sources. In *Proceedings of the International Astronautical Congress, IAC*, volume 8, pages 5616–5621. University of Surrey, 2014.
- [33] Accelerometers - vibration sensors for special purpose. <https://www.monitran.com/Products/Accelerometers/Accelerometers-BBI-Test>.
- [34] Scanning laser doppler vibrometer. <https://www.optomet.com/products/scanning-vibrometers/>.
- [35] Kistler multicomponent dynamometer, type 9256c datasheet. <http://web.sensor-ic.com:8000/ZLXIAZAI/KISTLER/000-484e-08.10.pdf>.
- [36] Mordechai Guri. Exfiltrating data from air-gapped computers via vibrations. *Future Generation Computer Systems*, 122:69–81, 2021.
- [37] Valdemir Carrara and Hélio Koiti Kuga. Estimating friction parameters in reaction wheels for attitude control. *Mathematical Problems in Engineering*, 2013.
- [38] Liran Sahar, Eviatar Edlerman, Hovhannes Agalarian, Vladimir Balabanov, and Pini Gurfil. Hard disk drive based reaction wheels for cubesat attitude control. *Journal of Spacecraft and Rockets*, 55(1):236–241, 2018.

- [39] Bryan Siepert. Adafruit_mpu6050 library. https://github.com/adafruit/Adafruit_MPU6050, March 2020.
- [40] InterlinkKnight. Arduino tutorial: Tachometer (rpm counter). <https://www.youtube.com/watch?v=u2uJMJwsfsg>, May 2019.
- [41] Dae-Kwan Kim. Micro-vibration model and parameter estimation method of a reaction wheel assembly. *Journal of Sound and Vibration*, 333(18):4214–4231, 2014.
- [42] Tutorial on measurement of power spectra. https://123.physics.ucdavis.edu/week_2_files/tutorial_on_measurement_of_power_spectra.pdf.
- [43] Daniele Addari. *A semi-empirical approach for the modelling and analysis of microvibration sources on-board spacecraft*. PhD thesis, University of Surrey (United Kingdom), 2016.
- [44] Zhe Zhang. *Development and validation of microvibration models for a satellite reaction wheel assembly*. PhD thesis, University of Southampton, 2013.
- [45] Adrian Rosebrock. Ball tracking with opencv. <https://www.pyimagesearch.com/2015/09/14/ball-tracking-with-opencv/>, 2015. Accessed: 16-11-2021.
- [46] Adrian Rosebrock. Opencv track object movement. <https://www.pyimagesearch.com/2015/09/21/opencv-track-object-movement/>, 2015. Accessed: 16-11-2021.
- [47] Samsung isocell gw1 sensor. <https://www.samsung.com/semiconductor/minisite/isocell/mobile-image-sensors/isocell-bright-gw1/>. Accessed: 15-11-2021.
- [48] Stanley Kon, Kenn Oldham, and Roberto Horowitz. Piezoresistive and piezoelectric mems strain sensors for vibration detection. In *Sensors and Smart Structures Technologies for Civil, Mechanical, and Aerospace Systems 2007*, volume 6529, page 65292V. International Society for Optics and Photonics, 2007.
- [49] Shan-Bo Chen, Ming Xuan, Lei Zhang, Song Gu, Xiao-Xue Gong, and Hong-Yu Sun. Simulating and testing microvibrations on an optical satellite using acceleration sensor-based jitter measurements. *Sensors*, 19(8):1797, 2019.